Università degli Studi di Ferrara

DOTTORATO DI RICERCA IN FISICA

CICLO XXXVI

Coordinatrice prof.ssa Eleonora Luppi

Sub-barrier fusion for ^{24,26}Mg + ^{12}C. New techniques of gamma-particle and heavy ion-particle coincidences for ^{30}Si + ^{12}C

Settore Scientifico Disciplinare: FIS/04

Dottorando:
Del Fabbro Mirco

Tutore:
Prof. Bettoni Diego
Prof.ssa Montagnoli Giovanna

firma

firma

Anni 2020/2023

Contents

List of Figures

List of Tables

Chapter 1

Introduction

Heavy-ion fusion is a quite complex phenomenon whose study has involved several experimental and theoretical efforts after the large Tandem electrostatic accelerators have been put into operation and allowed the production of medium-mass heavy-ion beams with sufficient energy to overcome the Coulomb barrier in collisions with targets of nearly all elements. A specific interest in the study of fusion dynamics evolved in the seventies, following the awareness that fusion reactions between heavy stable nuclei can produce exotic nuclei away from stability on the proton-rich side of the mass valley and they are crucial for the synthesis of very heavy elements.

Measured fusion excitation functions of light-heavy ion systems essentially follow the predictions of the well-known Wong formula based on the quantal penetration of the barrier, but experimental and theoretical studies on near- and sub-barrier heavy-ion fusion received a strong push in the late 70s because two basic kinds of experimental evidence were discovered: on one side, experimenters found the first hints of generalised very large enhancements of cross sections with respect to the simple predictions of the Wong formula. On the other side, shortly after, measurements gave evidence of strong isotopic effects, that is, fusion excitation functions of nearby systems may differ substantially in magnitude and shape. This indicated that a close connection exists between the sub-barrier fusion dynamics and the low-lying collective structure of the two colliding nuclei, and the coupled-channels (CC) model was developed in order to reproduce the experimental evidence. In the following decades, several experiments were performed aiming at clarifying this link in various experimental situations. Subsequently, Neil Rowley suggested [1] that the fusion barrier distributions (BD) originated by channel couplings could be obtained from the second derivative of the energy-weighted excitation functions with respect to the energy, and a second sequence of measurements started in the early 90s, aiming at extracting the shape of the BD for several different systems, as a fingerprint of channel couplings in the various cases. Measurements of this kind are very delicate and are still being pursued. Around ten years later, an experiment performed at Argonne National

Laboratory indicated that the fusion cross sections of ^{60}Ni + ^{89}Y have an unexpected behaviour far below the barrier [2], i.e., they drop much faster than predicted by standard CC calculations. This opened a new area of research, and this phenomenon (named "hindrance") was soon recognised as a general effect, with various aspects whose origin is still a matter of debate and research in the community.

1.1 Physical motivation

Fusion reactions of light systems are basic for understanding the astrophysical reactions responsible for elemental synthesis in stellar environments. Measurements of fusion cross section for light heavy-ions characterised by a positive Q-value are important to establish the presence of hindrance in such systems but challenging experiments are required. Concerning the very relevant case of ^{12}C + ^{12}C (Fig. 1.1 left panel), the behaviour of the fusion cross section at the very low energies is not clear, due also to the many resonances observed [3, 4, 5]. For the case of ^{16}O + ^{16}O (Fig. 1.1 right panel), evidence of hindrance was found in most measurements [6], and the various sets of data were analysed with the hindrance model [7]. The existence and features of hindrance in these systems are not at all established, therefore the study of slightly heavier systems can provide valuable information for placing on solid grounds the extrapolation to the lighter cases important in stellar environments. Recent experiments, performed with the PISOLO set-up [8], on the ^{24}Mg +

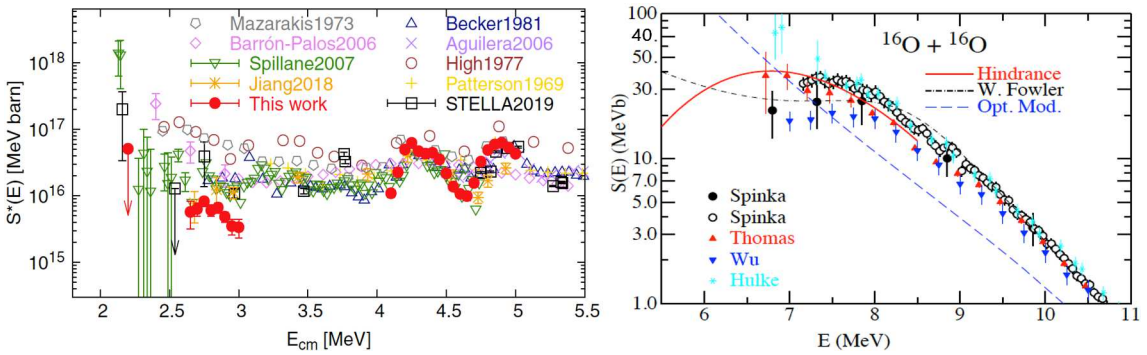

Figure 1.1. Astrophysical S factor for the systems ^{12}C+^{12}C [3] (left) and ^{16}O+^{16}O [6] (right). In the second case, evidence of the hindrance effect is observed.

^{12}C system [9] highlighted a peculiar behaviour of the astrophysical S factor, in fact, as shown in Fig. 1.2, the experimental data seem to be well reproduced by the no-coupling calculation at very low energies. To better understand this phenomenon the experimental data have been fitted with both a hindrance parametrization (red line) and an empirical formula in the spirit of the adiabatic model (blue line) [10]. Both approaches seem to well reproduce the behaviour at low energies of the data so more

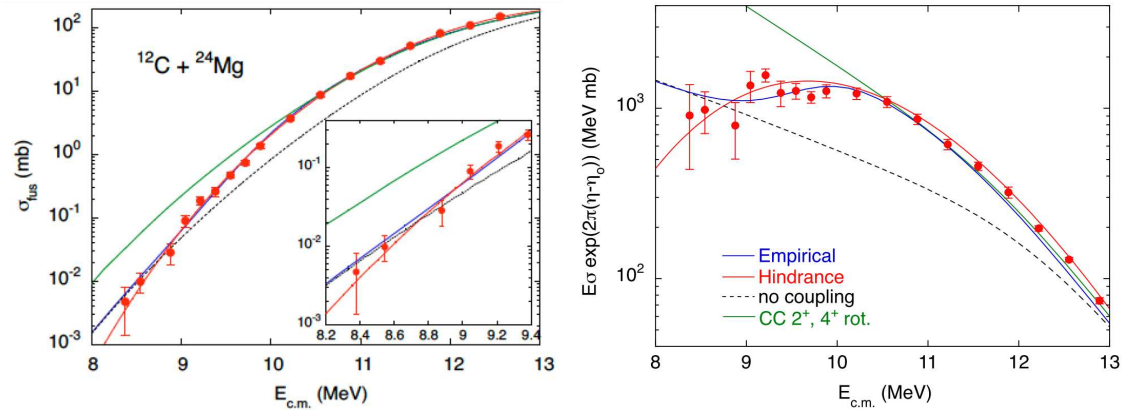

Figure 1.2. Excitation function (left) and astrophysical S factor (right) for the system ^{24}Mg+^{12}C where it can be seen that the no coupling calculation well reproduces the experimental data (figure from [9]).

precise measurements at lower energies are needed. But since the set-up PISOLO, employed to measure the fusion cross section for this system, cannot be used to measure cross sections below about 1 μb, two tests employing different techniques have been performed, to measure cross sections in the range of nanobarns. The analysis and the results of these test experiments are reported in this thesis. The first method consists of an improvement of the PISOLO set-up. Two silicon detectors were placed inside the reaction chamber to detect the charged particles evaporated after the fusion process in coincidence with the evaporation residues. The second method exploits the coincidence between the characteristics γ-rays emitted after the fusion process and the evaporated charged particles, using the gamma spectrometer AGATA [11] and the array of silicon detectors EUCLIDES [12].

Moreover, the ^{24}Mg + ^{12}C system presents a very large cross section at the hindrance threshold compared with similar systems (Fig. 1.3). The reason might be the α-like structure or the large prolate deformation of the ^{24}Mg nucleus. To better understand the behaviour of this system, this work includes also the study of the system ^{26}Mg + ^{12}C, which has a positive fusion Q-value (Q_{fus} = 18.5 MeV) as well. The ^{26}Mg is a prolate deformed nucleus like ^{24}Mg but it does not have the α-like structure. Consequently, a similar behaviour of these two systems might suggest that the large value of the cross section at the hindrance threshold is due to the prolate deformation of the projectile. Instead, a different behaviour might indicate that the underlying reason could be the α-like structure of ^{24}Mg.

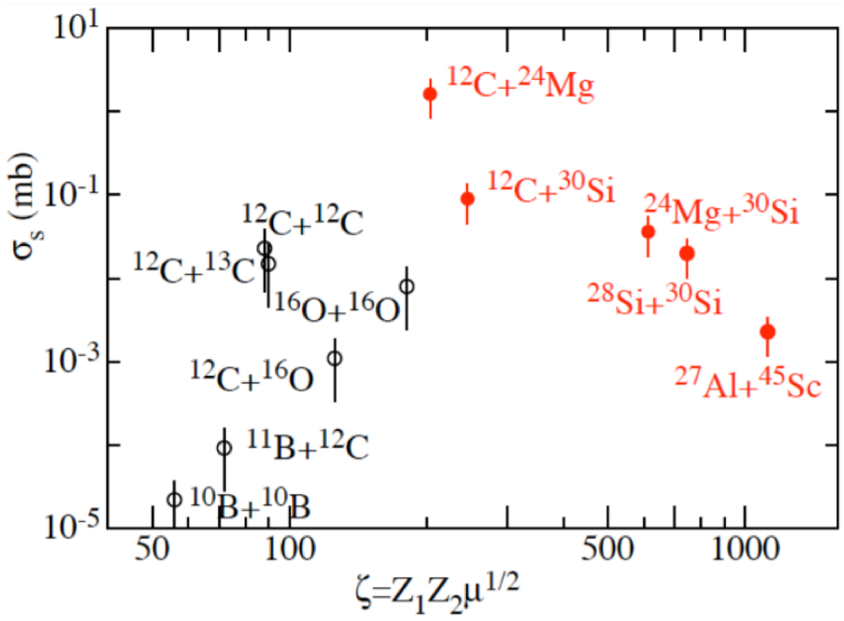

Figure 1.3. Cross section at the hindrance threshold for different medium-light systems. The value is about 10 times larger for ^{24}Mg + ^{12}C compared to the other cases.

Chapter 2

Sub-barrier fusion

Nuclear fusion is a process where two separate nuclei combine together and generate a compound nucleus. Classically this phenomenon can occur only if the energy of the relative motion of the two nuclei overcomes the Coulomb barrier, but due to the quantum tunnelling the fusion process can occur even at sub-barrier energies. The study of the fusion dynamics at energies far below the Coulomb barriers is of great importance not only for nuclear physics but also for astrophysics. This chapter presents the theoretical framework for the sub-barrier fusion process starting from a simple one-dimensional model based on barrier penetration. The coupled channel formalism and the models that try to explain the hindrance effect are then presented.

2.1 One-dimensional ion-ion potential

The first approach to the heavy-ion fusion reactions is within a unidimensional model in which the projectile and target nuclei are treated as structureless. Under this condition, the potential is a function of only the relative distance r between the colliding nuclei and it consists of two components: the nuclear potential $\mathrm{V}_N(\mathrm{r})$ and the Coulomb potential $\mathrm{V}_C(\mathrm{r})$. The Coulomb potential is expressed as the electrostatic potential between two point-like charged particles placed at a distance r:

$$V_C(r) = \frac{e^2 Z_p Z_t}{4\pi\epsilon r} \tag{2.1}$$

where Z_p and Z_t are respectively the projectile and target atomic number. This expression can be only used when the two interacting nuclei do not significantly overlap. A more realistic option consists in considering the projectile and the target as charged spheres with a uniform charge Z_p Z_t, then the Coulomb potential becomes

$$V_C(r) = \frac{e^2 Z_p Z_t}{4\pi\epsilon} \begin{cases} \frac{1}{r} & \text{if } r > R_C \\ \frac{1}{2R_C}\left(3 - \frac{r^2}{R_C^2}\right) & \text{if } r < R_C \end{cases} \tag{2.2}$$

where R_C is the Coulomb radius approximately given by $R_C = 1.2\left(A_p^{1/3} + A_t^{1/3}\right)$. The nuclear potential is particularly important to correctly interpret the experimental data since it defines the height and position of the Coulomb barrier. The nuclear potential can be estimated in several ways. The phenomenological Woods-Saxon potential [13] is widely used:

$$V_N(r) = \frac{-V_0}{1 + e^{(r-R_0)/a_0}} \tag{2.3}$$

where R_0 is the radius, V_0 is the depth and a_0 is the diffuseness of the potential. The three parameters of the Woods-Saxon potential can be estimated by a set of empirical formulae obtained from the analysis of elastic scattering data [13]:

$$\begin{aligned}
&R_p = (1.2A_p^{1/3} - 0.09)fm \qquad R_t = (1.2A_t^{1/3} - 0.09)fm \\
&R_0 = R_p + R_t \\
&\gamma = 0.95\left(1 - 1.8\frac{A_p - 2Z_p}{A_t}\frac{A_t - 2Z_t}{A_p}\right) \\
&V_0 = 16\pi\gamma a_0\frac{R_pR_t}{R_p + R_t} \\
&a_0 = \frac{1}{1.17[1 + 0.53(A_p^{-1/3} + A_t^{-1/3})]}
\end{aligned}$$

This potential is represented in Fig. 2.1 for the system ^{26}Mg + ^{12}C.

However, this Akyüz-Winter potential cannot give a precise description of the fusion dynamics at energy far below the barrier since it is extracted from elastic and inelastic collisions that involve only the nuclear surface while the fusion process requires a larger overlap of the two interacting nuclei. A double-folding potential [14] has been introduced to provide a better description at low energies. Such a potential is given by:

$$V_N(r) = \int d\mathbf{r}_1 \int d\mathbf{r}_2 \rho_p(\mathbf{r}_1)\rho_t(\mathbf{r}_2)v_{NN}(\mathbf{r}_{12}) \tag{2.4}$$

where $\mathbf{r}$ is the relative vector between the interacting nuclei, the $\mathbf{r}_i$'s are referred to the centres of the nuclei respectively and $\mathbf{r}_{12} = \mathbf{r} + \mathbf{r}_2 - \mathbf{r}_1$, v_{NN} is the effective nucleon-nucleon interaction, ρ_p and ρ_t are the density of the projectile and target, respectively. An often-used nucleon-nucleon interaction is the so-called Michigan-3-Yukawa-Reid (M3Y) [15, 14] interaction that produces a double-folding potential in good agreement with the Akyüz-Winter potential at energies above the barrier where the elastic scattering is the main reaction channel. However, it is still unrealistic at sub-barrier energies where the potential constructed in this way is much deeper compared to the ground state of the compound nucleus. The M3Y interaction may be also supplemented with a repulsive core that is suggested to originate from the

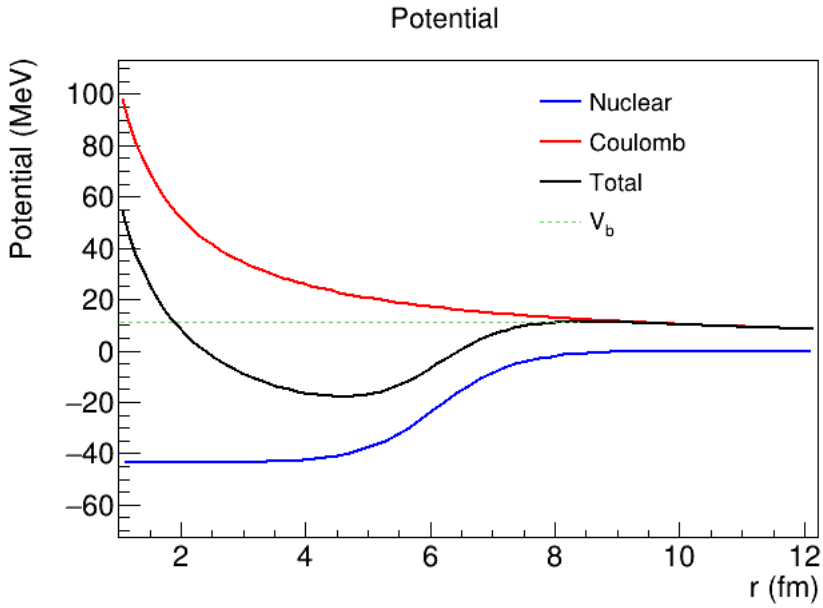

Figure 2.1. Unidimensional potential for the system ^{26}Mg+^{12}C: the red line represents the Coulomb potential, the blue one the nuclear potential and the black one the total one.

incompressibility of the nuclear matter. This repulsive term is given by:

$$v_{NN}^{rep} = v_0 \delta(\mathbf{r}_{12}) \tag{2.5}$$

where the amplitude v_0 is calibrated to reproduce reasonable incompressibility of the overlapping nuclei [16]. The repulsive potential is thus obtained by adding this constant term as an interaction in the double-folding potential formula (Eq. 2.4). The comparison between the Akyüz-Winter and the M3Y potentials with and without repulsion for the system ^{64}Ni+^{64}Ni is shown in Fig. 2.2.

2.2 One-dimensional model

The fusion of two spherical colliding nuclei can be described by the Schrödinger equation, as follows:

$$\left(-\frac{\hbar^2}{2\mu}\nabla^2 + V(r) - E \right) \Psi(r) = 0 \tag{2.6}$$

where μ is the reduced mass of the system and V(r) is the total potential. If the nuclei involved are considered structureless V(r) is still the sum of the Coulomb potential

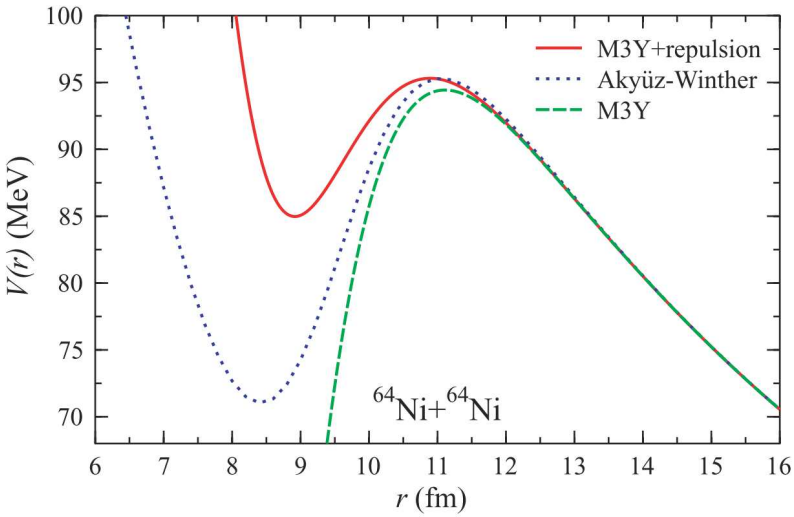

Figure 2.2. Comparison between the Akyüz-Winter and the M3Y and M3Y+repulsion potential for the system ^{64}Ni+^{64}Ni.

and the nuclear potential. The solution of the equation can be expanded in terms of spherical harmonics, where the radial part obeys the following equation:

$$\left(-\frac{\hbar^2}{2\mu}\frac{d^2}{dr^2}+\frac{l(l+1)\hbar^2}{\mu r^2}+V(r)-E\right)u(r)=0 \tag{2.7}$$

In the last equation, the centrifugal repulsive potential appears.

In this model, the cross section is linked to the probability that the nuclei overcome the barrier so that fusion may occur. Neglecting the spin, this probability is expressed by the transmission coefficient $\mathrm{T}_l(\mathrm{E})$ relative to the energy E and the partial wave l. The partial-wave cross section is proportional to the transmission coefficient

$$\sigma_l(E)=\pi\lambda\!\!\!^{-2}(2l+1)T_l(E) \tag{2.8}$$

The total cross section is obtained by the sum over the partial waves, but there is a maximum value of the angular momentum (l_{max}) above which fusion does not occur and the two nuclei separate after a period of contact. The value of l_{max} can be obtained from the angular momentum conservation and results to be:

$$l_{max}=R_{bl}\sqrt{\frac{2\mu}{\hbar^2}(E-V_{bl})} \tag{2.9}$$

where R_{bl} and V_{bl} are the position and the height of the Coulomb barrier respectively and μ is the reduced mass of the system. For $l<l_{max}$ the orbital angular momentum of the system, and consequently also the centrifugal potential, is reduced by dissipative

forces. At this point, the system is captured in the pocket of the nuclear potential and can evolve into a compound nucleus. Instead, if $l > l_{max}$ the capture in the potential pocket does not occur and the two nuclei separate after a period of contact where there is a dissipation of energy and the exchange of nucleons. The fusion cross section is therefore:

$$\sigma(E) = \sum_{0}^{l_{max}} \pi \lambda\!\!\!^{-2}(2l+1)T_l(E) \tag{2.10}$$

The transmission coefficient can be obtained by approximating the Coulomb barrier with a parabola [17].

$$V(r) = V_{bl} - \frac{1}{2}\mu\omega_l^2(r - R_{bl})^2 \tag{2.11}$$

where V_{bl} and R_{bl} are the height and the position of the barrier and ω_l is linked to the curvature of the parabola for the l^{th} wave given by:

$$\hbar\omega_l = \sqrt{-\frac{\hbar^2}{\mu}\left.\frac{\delta^2 V(r)}{\delta r^2}\right|_{r=R_{bl}}} \tag{2.12}$$

Within this approximation, the transmission coefficient results to be:

$$T_l = \frac{1}{1 + e^{\frac{2\pi}{\hbar\omega_l}(V_{bl}-E)}} \tag{2.13}$$

By assuming that the position of the barrier R_{bl} and ω_l are independent of the angular momentum they can be approximated with their value for the s-wave (l = 0) ($R_{bl} = R_{b0}$ and $\omega_l = \omega_0$). The result is that the dependence of the transmission coefficient on the angular momentum can be obtained by shifting the incident energy by a rotational term:

$$T_l = T_0\left(E - \frac{\hbar^2 l(l+1)}{2\mu R_b^2}\right) \tag{2.14}$$

Using this transmission coefficient in the cross section equation and replacing the sum with an integral the fusion cross section results to be given by the Wong formula [18]:

$$\sigma_{fus}(E) = \frac{\hbar\omega_0 R_b}{2E} ln\left[1 + e^{\frac{2\pi}{\hbar\omega_0}(E-V_b)}\right] \tag{2.15}$$

The single barrier penetration model has achieved great success in the description of fusion cross section in light systems. On the contrary, it underestimates the sub-barrier fusion for heavier systems, although it reproduces the experimental data above the Coulomb barrier. In Fig. 2.3 can be seen this situation for the two cases ^{16}O+^{16}O (left) and ^{64}Ni+^{64}Ni [19] (right). This suggested that other degrees of freedom take part in the fusion process besides the relative motion of the two nuclei, and then the coupled-channels [20] model was developed.

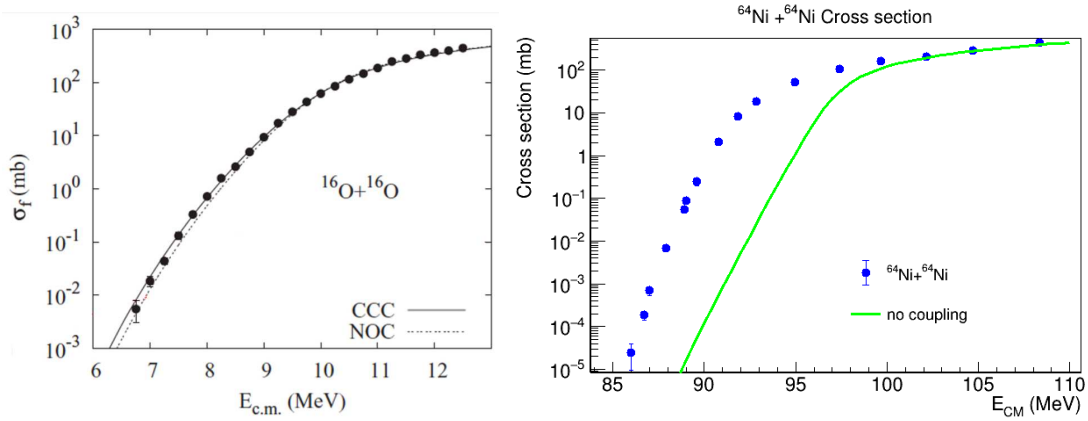

Figure 2.3. The Wong formula (NOC) applied to the light system ^{16}O+^{16}O (left) and to the heavier case ^{64}Ni+^{64}Ni (right). The experimental data of ^{16}O+^{16}O are well reproduced while the excitation function of ^{64}Ni+^{64}Ni is clearly underestimated.

2.3 Coupled Channels model

In the coupled-channels model it is necessary to consider the coupling between the relative motion and the nuclear structure ζ, so that, the Hamiltonian becomes:

$$H(r,\zeta) = H_0(\zeta) + H_k(r) + V_l(r) + V_{int}(r,\zeta) \tag{2.16}$$

where $H_k(r)$ is the kinetic energy, $V_l(r)$ is the ion-ion potential for the wave l, $H_0(\zeta)$ describes the internal structure of the two nuclei and V_{int} is the coupling term. With this Hamiltonian, the stationary Schrödinger equation becomes:

$$\left(-\frac{\hbar^2}{2\mu}\frac{d^2}{dr^2} + \frac{l(l+1)\hbar^2}{\mu r^2} + V(r) - E\right)\Psi(r,\zeta) = -\left(H_0(\zeta) + V_{int}(r,\zeta)\right)\Psi(r,\zeta) \tag{2.17}$$

Denoting $\mid n >$ as the eigenstates and ϵ_n the eigenvalues of the intrinsic Hamiltonian $H_0(\zeta)$, the wavefunction $\Psi(r,\zeta)$ can be expanded in these eigenstates:

$$\Psi(r,\zeta) = \sum_n \chi_n(r) \mid n > \tag{2.18}$$

We have therefore a set of coupled differential equations and taking advantage of the orthonormality of the base of the eigenstates $\mid n >$, it is possible to apply the bra $< m \mid$ to the equations and obtain a new set of coupled equations whose solutions are the wave functions $\chi_n(r)$ of the relative motion of the two nuclei:

$$\left(-\frac{\hbar^2}{2\mu}\frac{d^2}{dr^2} + \frac{l(l+1)\hbar^2}{\mu r^2} + V(r) - E\right)\chi_m(r) = -\sum_n M_{mn}\chi_n(r) \tag{2.19}$$

where the coupling matrix M_{mn} has been defined as:

$$M_{mn} = \epsilon_m \delta_{mn} + < m \mid V_{int}(r, \zeta) \mid n > \tag{2.20}$$

The matrix M_{mn} is symmetric and can be diagonalized using some appropriate approximations [20, 21].

In the optical model, the internuclear potential $V(r)$ is usually supplemented with an imaginary component $-iW(r)$ which simulates the absorption into reaction channels in fusion reactions, then the Schrödinger equation for each partial wave l is written as:

$$\left(-\frac{\hbar^2}{2\mu}\frac{d^2}{dr^2} + \frac{l(l+1)\hbar^2}{\mu r^2} + V(r) - iW(r) - E\right) u(r) = 0 \tag{2.21}$$

To solve this equation typically the following boundary conditions are applied:

$$\begin{cases} u(r) \approx r^{l+1} & r \to 0 \\ u(r) \approx i/2 \left[H_l^+(kr) - S_l H_l^-(kr)\right] & r \to \infty \end{cases} \tag{2.22}$$

where H_l^+ and H_l^- are the outgoing and incoming Coulomb wave functions, S_l is the nuclear S-matrix and $k = \sqrt{2\mu E/\hbar^2}$ is the wave number for the energy E. If the imaginary part of the potential is well confined inside the Coulomb barrier, then the absorption cross section can be regarded as the fusion cross section:

$$\sigma_{fus} \approx \sigma_{abs} \approx \frac{\pi}{k^2} \sum_l (2l+1)(1 - |S_l|^2) \tag{2.23}$$

in heavy-ion fusion reactions, the so-called incoming wave boundary condition (IWBC) is often applied instead of introducing the imaginary part of the potential [22]. The IWBC corresponds to the case where there is strong absorption within the inner region of the barrier so that the incoming flux never returns back. Under this condition the wave function for $r \leq r_{abs}$ assumes the form:

$$u(r) = \sqrt{\frac{k}{k_l(r)}} T_l exp\left[-i \int_r^{r_{abs}} k_l(r')dr'\right] \qquad r \leq r_{abs} \tag{2.24}$$

where T_l is the transmission coefficient for the l^{th} partial wave and r_{abs} is the absorption radius that is assumed to be inside the Coulomb barrier. $k_l(r)$ is the local wave number for the l^{th} wave function at the energy E and is given by:

$$k_l(r) = \sqrt{\frac{\mu}{\hbar^2}(E - V(r)) - \frac{l(l+1)\hbar^2}{2\mu r^2}} \tag{2.25}$$

For heavy-ion reactions, the final result does not depend on the position of r_{abs} that is usually taken at the minimum of the interaction potential. Under this condition, the fusion cross section from Eq. 2.23 becomes:

$$\sigma_{fus} = \frac{\pi}{k^2} \sum_l (2l+1) P_l(E) \tag{2.26}$$

where P_l is the penetrability for the l^{th} scattering wave defined as

$$P_l(E) = 1 - |S_l|^2 = |T_l|^2 \tag{2.27}$$

and T_l is the transmission coefficient. The IWBC is valid only if there is strong absorption inside the Coulomb barrier as it happens for heavy-ion reactions. Other approximations are applied to reduce the dimension of the coupling matrix. In the coupled channel method, an excited state of internal spin I generates $I+1$ channels when it is coupled to the angular momentum l_i of the relative motion, since each orbital angular momentum of the type $l_i' = \mid l_i - I \mid, .., \mid l_i + I \mid$ satisfies the condition $\mathbf{J} = \mathbf{I} + \mathbf{l_i}$. The so-called iso-centrifugal approximation reduces the number of channels by assuming that the orbital angular momentum is the same in all reaction channels, and under this condition, there is only one channel for each excited state (instead of I+1). The so-called sudden approximation [23] assumes that the tunnelling process occurs much faster than the intrinsic motion so that the nuclear structure is not perturbed during the penetration of the Coulomb barrier. In this approximation, the internal energy ϵ can be neglected with respect to the coupling strength, this means that in the coupling matrix M_{mn} (Eq. 2.20) the first term can be neglected to obtain

$$M_{mn} = < m \mid V_{int}(r, \zeta) \mid n > \tag{2.28}$$

This approximation, however, is valid only for strongly deformed nuclei. If the reduced mass of the system and the potential energy are the same for all the channels, it is possible to factorize the coupling potential in two terms which depend separately on the intrinsic and relative motions

$$< m \mid V_{int}(r, \zeta) \mid n >= F(r) < m \mid G(\zeta) \mid n > \tag{2.29}$$

A further approximation is based on supposing $F(r) = F(R_b)$ constant where $F(R_b)$ is the value of F at the barrier (constant coupling approximation). This approximation is not used by CCFULL [24] (the program employed in this thesis for the cross section calculation). Under this condition, the coupling matrix can be diagonalized by a unitary matrix U:

$$Y_m = \sum_n U_{mn} \chi_n \qquad \sum_{ij} U_{ni} M_{ij} U_{jm} = \delta_{mn} \lambda_m \tag{2.30}$$

What is obtained is a set of decoupled equations:

$$\left(-\frac{\hbar^2}{2\mu}\frac{d^2}{dr^2} + V(r) + \lambda_m F - E\right) Y_m(r) = 0 \tag{2.31}$$

where the total potential for each channel becomes $V(r)+\lambda_m F$: in this way, the single Coulomb barrier has been replaced with a set of barriers, each one with a transmission coefficient. The total transmission coefficient can be obtained as the weighted sum of the transmission coefficients of each barrier.

$$T = \sum_m |U_{m1}|^2 \, T[E, V(r) + \lambda_m] \tag{2.32}$$

The factor $W_m = |U_{m1}|^2$ represents the contribution of the m-th barrier to the total fusion cross section that is therefore expressed as the weighted sum of the cross section for each barrier

$$\sigma_f = \sum_m W_m \sigma_{fm} \tag{2.33}$$

2.4 Enhancement

The coupled-channels model predicts an enhancement of the fusion cross section below the barrier. To understand how the model works a simple example with only two channels can be considered. Assuming a constant form factor F and a Q-value Q for the coupled channel, the coupling matrix is $M = \left(\begin{smallmatrix} 0 & F \\ F & -Q \end{smallmatrix}\right)$; then the decoupled equations for the present case are:

$$\begin{aligned} \left(-\frac{\hbar^2}{2\mu}\frac{d^2}{dr^2} + V(r) - E + \lambda_+ F\right) Y_+(r) = 0 \\ \left(-\frac{\hbar^2}{2\mu}\frac{d^2}{dr^2} + V(r) - E + \lambda_- F\right) Y_-(r) = 0 \end{aligned} \tag{2.34}$$

where $\lambda_\pm$ are the eigenvalues and $Y_\pm$(r) are the eigenfunctions of the diagonalized coupling matrix. The eigenvalues of M and their weights turn out to be:

$$\lambda_\pm = \frac{-Q \pm \sqrt{Q^2 + 4F^2}}{2} \qquad P_\pm = \frac{F^2}{F^2 + \lambda_\pm^2} \tag{2.35}$$

In this way, the barrier splits into two barriers, one higher by an amount λ_+ and one lower by λ_- than the original barrier. As shown in Fig. 2.4 the transmission probability is increased for energies lower than and reduced for energies higher than the Coulomb barrier. The effect of the enhancement is that of increasing the fusion cross section below the Coulomb barrier as shown in the example of Fig. 2.5.

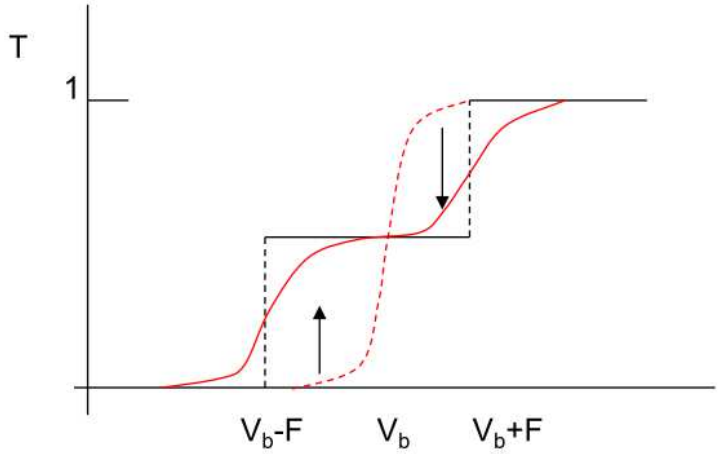

Figure 2.4. Comparison between the transmission coefficient for the unidimensional model (dashed red line) and the coupled-channel model (solid red line), the step function (black line) is obtained in the classical limit.

2.5 Hindrance phenomenon

The experimental data of many systems (like ^{64}Ni+^{64}Ni [19]) showed that, although the coupled-channels approach successfully reproduced the excitation function for heavy ion reactions at energies above and below the barrier, the experimental cross sections at far sub-barrier energies were overestimated. This phenomenon is called hindrance.

In order to describe the hindrance two models have been proposed, the first one by Misicu and Esbensen is the so-called sudden approach [26, 14], which treats the nuclear density as frozen during the collision, assuming in this way that fusion occurs rapidly. They suggest that the incompressibility of nuclear matter becomes effective at small internuclear distances, thus generating a repulsive core in the ion-ion potential, which is then much shallower than standard potentials. This reduces the fusion probability. The second model, proposed by Ichikawa et al., is called the adiabatic model [10] where the fusion process occurs with the formation of a neck between the two interacting nuclei in the overlap region. In this model, the fusion process occurs more slowly and the hindrance phenomenon arises from the tunnelling of the one-body potential due to neck formation, instead of a two-body potential. Fig. 2.6 schematically reports the nuclear ion-ion potential according to these two models. Both of them managed to reproduce several systems despite their origin from quite different hypotheses.

Hindrance shows up in different ways for different systems so that to evidence its presence the logarithmic derivative of $E\sigma$ L(E) and the astrophysical factor S(E)

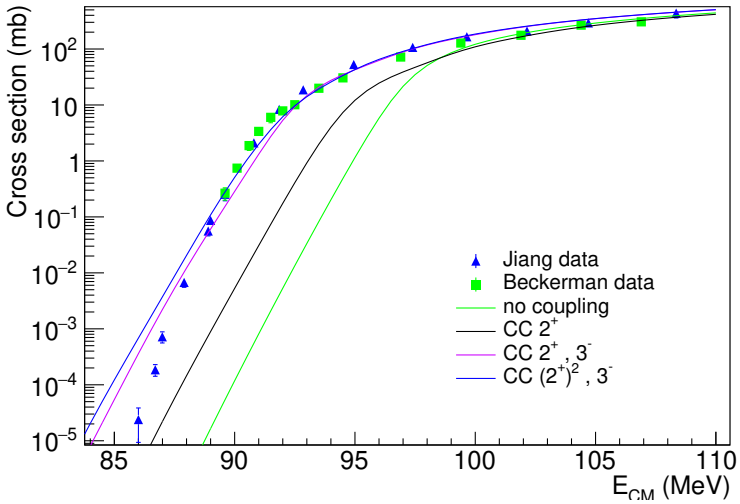

Figure 2.5. Comparison between ^{64}Ni+^{64}Ni experimental cross sections and theoretical prediction (see text).

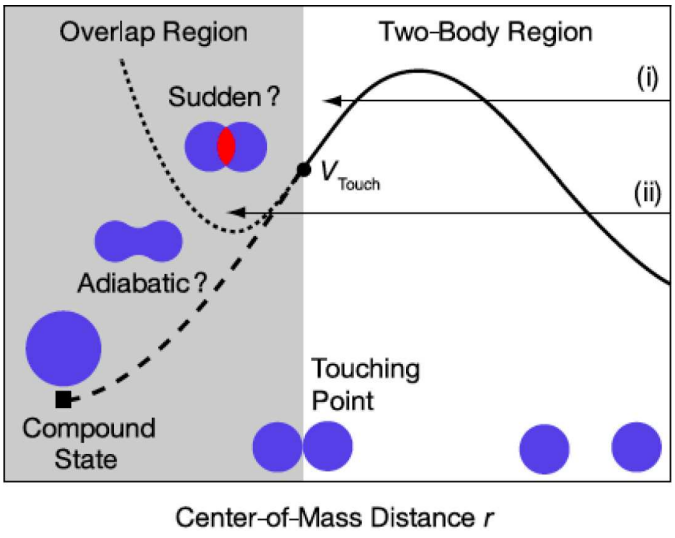

Figure 2.6. Scheme of a heavy ion-ion potential as a function of the centre of mass distance r between colliding nuclei [25]. In the figure, the touching point of the colliding nuclei V_{touch} and its compound state are shown with a circle and square point, respectively. The grey area represents the overlapping region of the colliding nuclei. The dashed and dotted lines indicate the potential energy curves for the adiabatic and the sudden approach, respectively.

are used. L(E) represents the slope of the excitation function

$$L(E) = \frac{dln(E\sigma)}{dE} = \frac{1}{E\sigma}\frac{d(E\sigma)}{dE} \tag{2.36}$$

where E is the energy in the centre of mass of the system. L(E) increases with decreasing energy (Fig. 2.7, left). The astrophysical factor S(E) is defined as:

$$S(E) = E\sigma(E)e^{2\pi\eta} \tag{2.37}$$

where η is the Sommerfeld parameter $\eta = 0.157 Z_p Z_t \sqrt{\frac{\mu}{E}}$ and μ is the reduced mass of the system.

The astrophysical factor is extracted directly from the excitation function (unlike L(E)) so it is a useful way to represent the trend of the excitation function for energies far below the Coulomb barrier (Fig. 2.7, right). The two quantities S(E) and L(E) are related since

$$\frac{dS(E)}{dE} = S(E)(L - \frac{\pi\eta}{E}) \tag{2.38}$$

therefore S(E) develops a maximum at the energy where:

$$L(E) = L_{CS} = \frac{\pi\eta}{E} \tag{2.39}$$

That energy is conventionally taken as the threshold for deep sub-barrier hindrance.

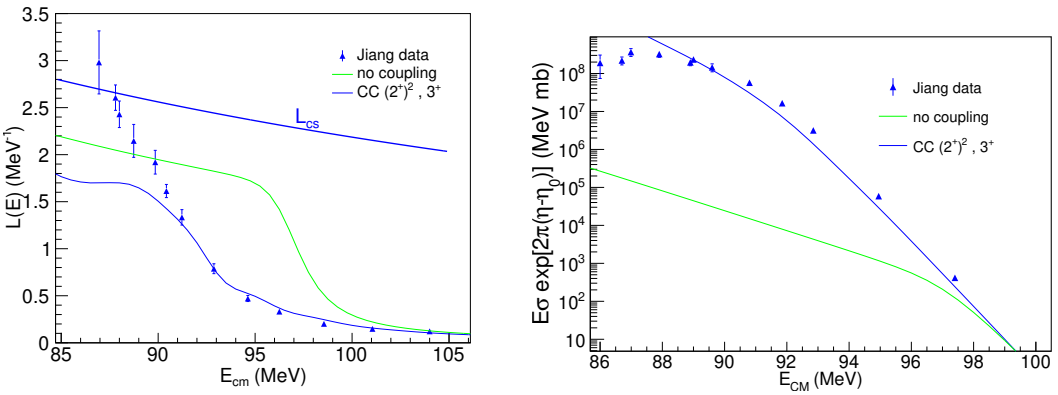

Figure 2.7. Logarithmic derivative (left) and astrophysical factor (right) for the ^{64}Ni+^{64}Ni system confronted with the theoretical prevision. It can be seen that the experimental value of L(E) overcomes the L_{CS} value and S(E) presents a maximum and as a consequence, the excitation function presents hindrance (see Fig. 2.5)

2.6 Effect of transfer channel with positive Q-value

Recent studies have shown the influence of transfer processes with positive Q-value on the fusion reactions at sub-barrier energies, where an enhancement of the cross sections is observed with respect to the coupled-channels calculations including the vibrational and rotational states. The pair transfer between the ground states of the interacting nuclei can be included in the coupled channel calculations through the macroscopic form factor [22]

$$F_{trans}(r) = F_t \frac{dV_N^{(0)}}{dr} \tag{2.40}$$

where F_t is the coupling strength. An example can be found in the two systems ^{58}Ni + ^{64}Ni and ^{40}Ca + ^{96}Zr [27, 28] where, as shown in Fig. 2.8, the theoretical predictions underestimate the experimental data. There is no indication of the fusion hindrance effect. On the contrary, for the similar system ^{64}Ni + ^{64}Ni, which does not present positive Q-value neutron transfer channels, the behaviour at very low energies is quite different with respect to ^{58}Ni + ^{64}Ni, in fact, the CC calculation overestimates the experimental data at low energies showing the presence of hindrance effect as shown in Fig. 2.5.

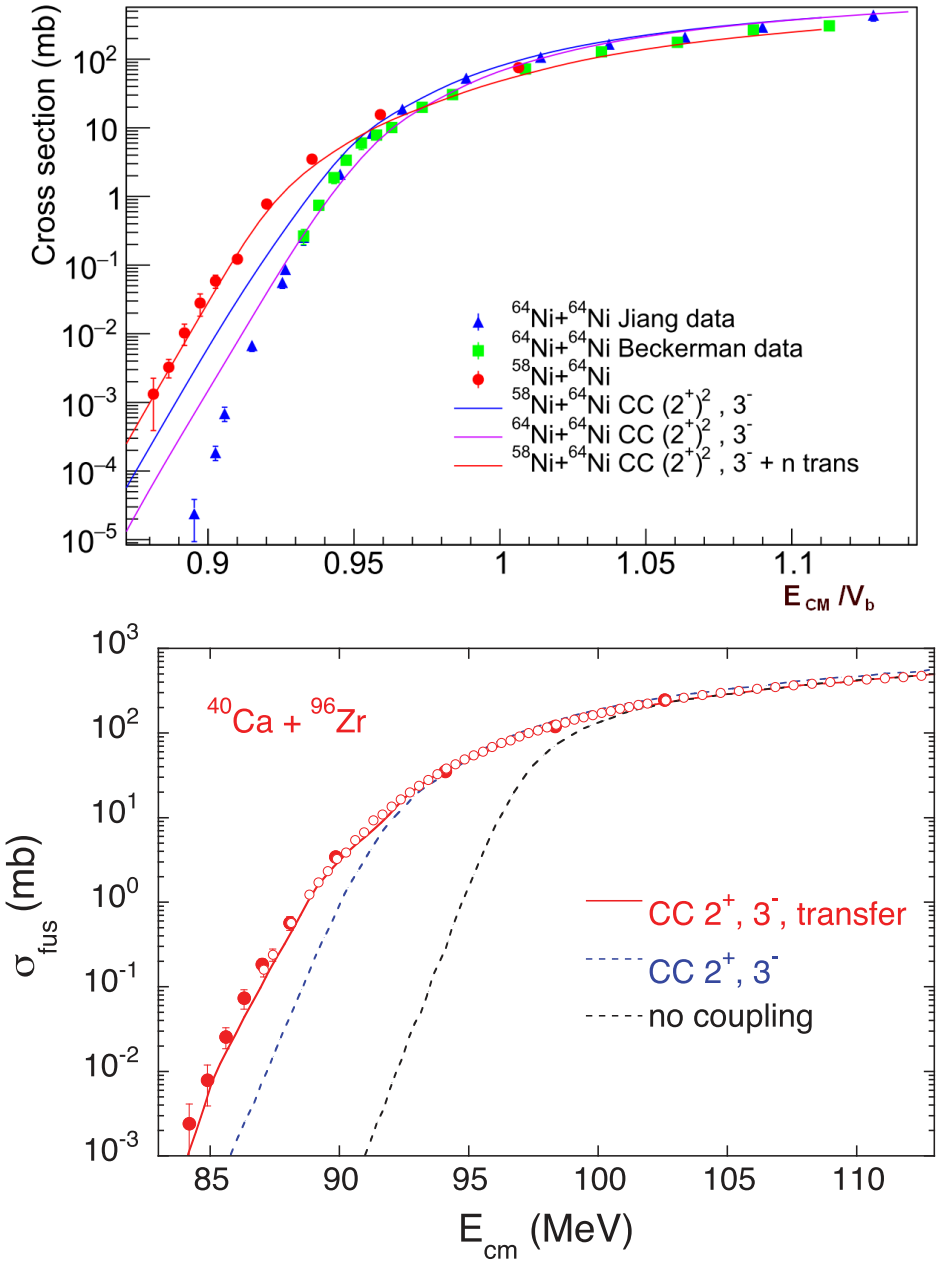

Figure 2.8. Fusion excitation functions for ^{58}Ni+^{64}Ni (top panel) and ^{40}Ca + ^{96}Zr (figure from [28]) (bottom panel).

Chapter 3

PISOLO Set-up

3.1 The electrostatic deflector PISOLO

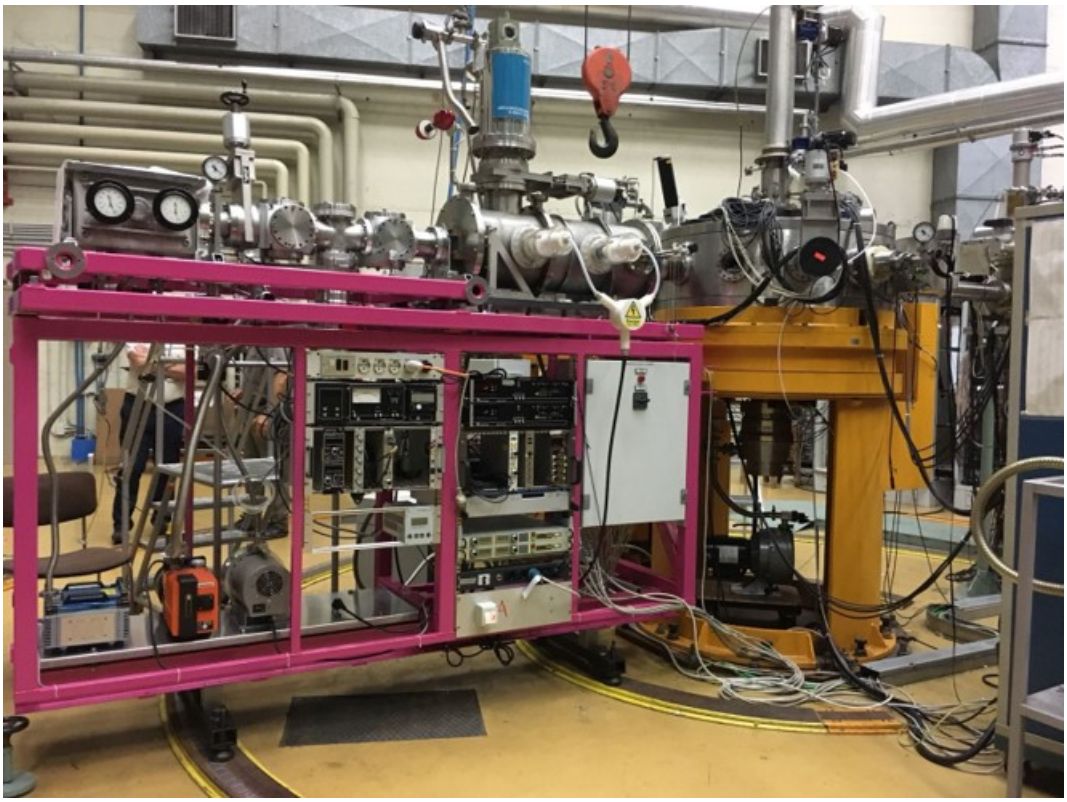

Figure 3.1. Picture of he PISOLO set-up

Fusion cross sections can be experimentally determined by direct detection of evaporation residues (ER). For the measurement of the ^{26}Mg + ^{12}C system the elec-

trostatic deflector PISOLO [8] (Fig. 3.2) has been used. This set-up has been designed to allow a fast and reliable measurement of relative and absolute fusion cross sections. The apparatus consists of a reaction chamber, an electrostatic deflector and an energy (E), energy loss (ΔE) and time of flight telescope based on 2 micro-channel plates, an ionization chamber and a silicon detector at the end of the apparatus.

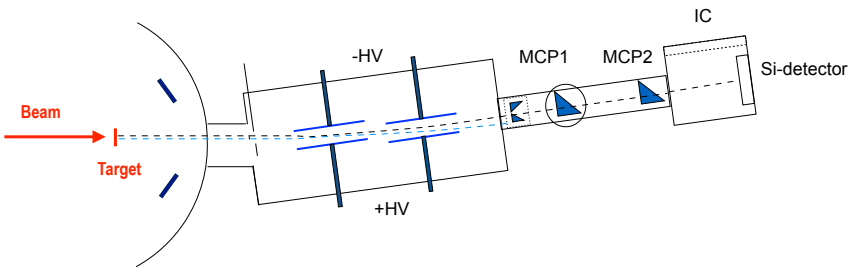

Figure 3.2. Scheme of the PISOLO set-up (figure from [8]).

3.2 Scattering chamber and electrostatic deflector

The reaction chamber is made of stainless steel and has a cylindrical structure with an internal radius of 50 cm. It allows a rotation keeping the vacuum inside (10^{-6} mbar) by means of a sliding seal, to perform angular distribution measurements. Targets are fixed in a six-position holder (Fig. 3.3 left) and consisted of 50 μg/cm^2 ^{12}C. One of the positions is reserved for a quartz plate with a small central hole (1.5 mm in diameter), used to focus the beam. The target support is attached to the cover of the reaction chamber and is moved through an external control system, to be able to focus the beam at each change of energy and to change the target or its angle with respect to the beam direction without breaking the vacuum. Four 50 mm^2 silicon detectors are placed at a distance of 195 mm from the target, they are mounted on a circular support, to a scattering angle of $\theta_{lab} = 16°$ with respect to the beam direction, as shown in Fig. 3.3 (right). These detectors are used to normalize the fusion yields to the Rutherford cross section and to monitor the changes in beam intensity and position on the target, usually associated with the effects of the magnets installed on the beam line upstream of the reaction chamber. The monitor detectors have collimators with a diameter of 1.5 mm to reduce the counting rate and consequently the radiation damage. Taking into account that the surface of the detectors is not perpendicular to the line connecting each of them to the target, their total solid angle is $\Delta\Omega_{mon}$=(166.7$\pm$1.7) μsr for the four monitors.

Figure 3.3. Target holder (left) and set-up of four monitors (right).

The electrostatic deflector allows the separation between the ER and the non-interacting beam. The deflector exploits the difference in electrical rigidity between the ER and the beam particles. This rigidity is defined as $\eta=\frac{E}{q}$, where E is the energy of the particle and q is the ion charge state. The deflector is placed at an angle of 4.7° with respect to the beam direction. The trajectory of charged particles in the electrostatic field region can be approximated to an arc of circumference, with a radius of curvature r given by:

$$\frac{mv^2}{r} \sim q\epsilon \tag{3.1}$$

where v and m are the velocity and mass of the ion respectively, while ϵ is the transverse electric field. Given that for the momentum conservation law, the momentum of ER and beam particles are approximately equal, the ratio between the radii of curvature of the residues (r_{ER}) and of the beam particles (r_b) is proportional to the respective electrical rigidities:

$$\frac{r_{ER}}{r_b} = \frac{(mv^2)_{ER}}{q_{ER}} \cdot \frac{q_b}{(mv^2)_b} \sim \frac{E_{ER}}{q_{ER}} \cdot \frac{q_b}{E_b} \sim \frac{m_b}{m_{ER}} \cdot \frac{q_b}{q_{ER}} \tag{3.2}$$

Since the mass and the charge state of the residues are usually greater than those of the beam ions, r_{ER} is smaller than r_b. The different trajectories allow a clear separation between the two types of particles. The electrostatic deflector is contained in a stainless steel cylinder 30 cm in diameter and 85 cm in length. Inside the cylinder, two pairs of stainless steel rectangular electrodes with smooth surfaces are placed. Each

electrode has dimensions of 25 cm × 12 cm and a thickness of 0.5 cm. The distance between the plates is adjustable externally and separately for each electrode. Two different and independent field regions are generated, which allow a good adjustment for the different experimental conditions by minimizing the scattering of the beam on the plates. Two high-voltage power supplies bring the electrodes up to a maximum voltage of around 40 kV and a collimator placed between the reaction chamber and the electrostatic deflector (entrance collimator) defines the acceptance angle of the device. The applied voltage together with the geometry of the deflector plates bend slightly the primary beam that is stopped on a side of a collimator (exit collimator) placed at the end of the deflector. The ER, having lower electric rigidity, pass through the collimator and reaches the detection system. The applied voltage is chosen for each energy to maximize the transmission of residues. However, not all the beam particles are stopped; in typical fusion experiments the rejection factor, defined as the ratio between the number of incoming and outgoing beam particles from the deflector, is $\sim 10^{7-8}$. Indeed, as a result of the scattering in the target and the multiple collisions with the electrodes or the edges of the collimators, a fraction of the beam particles, degraded in energy, enters the exit collimator. A further separation of the two types of ions is therefore necessary. This is realized by the detector telescope downstream of the exit collimator.

3.3 Detector telescope

The telescope discriminates the particles by exploiting the longer time of flight (TOF) of more massive particles with respect to lighter particles of the same kinetic energy. This allows us to distinguish the ER from the ions of the beam by measuring their TOF and their energy (E). The telescope (Fig. 3.4) consists of two microchannel plate detectors (MCP) [29], an ionization chamber (IC) [30] and a silicon surface barrier detector of 600 mm^2 area. Before reaching the silicon detector, the particles pass through the IC which provides their differential energy loss, while the silicon detector measures the residual energy. The telescope and the deflector are mounted on a platform that can be rotated to perform angular distribution measurements. In order to measure the TOF, the use of MCP allows the detection of ions without significantly changing their energy. They are based on pairs of 43×63 mm^2 glass plates appropriately built to act as very compact electron multipliers with high gain (around 10^3 for each plate). The ions do not interact directly with the plates, they pass through a carbon foil of about 20 μg/cm^2 placed perpendicularly to their direction. As a result of the interaction of the ions with carbon delta-electrons are emitted which are subsequently accelerated and bent onto the plates by an electrostatic mirror placed at 45°. The produced signals are very fast (around 2ns rise time) with a typical amplitude of tenths-hundreds of mV for heavy ions. Each MCP detector has a transparency of 85%, due to the presence of several grids, whereas their measured

intrinsic efficiency is close to 100% for heavy ions. The two MCPs yield the TOF together with the silicon detector, placed at the end of the telescope, that provides the starting signal for the TOF and triggers the data acquisition. The two flight bases are 666 mm and 1047 mm. The time resolution of the MCP detectors is comparable to that of the Silicon detector, and overall they sum up to around 300 ps.

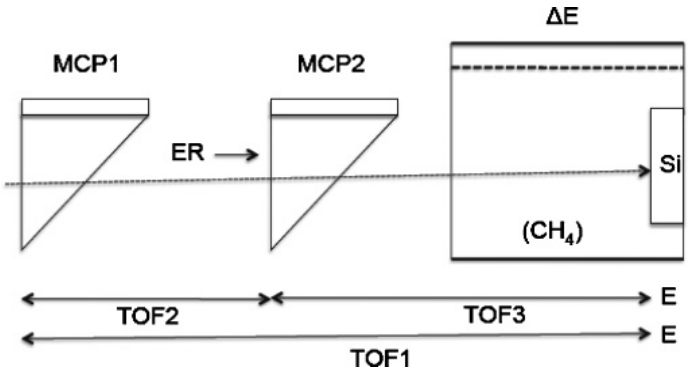

Figure 3.4. Scheme of the detector telescope.

The last detector of the telescope is a conventional ionization chamber using a Frisch grid shown schematically in Fig. 3.5. The two parallel electrodes generate an electric field perpendicular to the particles trajectory. The advantage of this transverse field ionization chamber is a fast separation of the formed electron-ion pairs. In addition, the Frisch grid removes the dependence of the anode pulse amplitude on the transverse position of the interaction. The cathode consists of one single plate of stainless steel, whereas the anode is segmented into three parts of 8 cm, 6 cm and 14 cm. This division of the anode allows the extraction of three differential energy loss signals (ΔE) enabling particle identification, however, in this experiment, the three signals were combined in a single one. The pressure was chosen so that the ER lose about half of its energy in the gas, and for this experiment has been set to 10 mbar. The chosen applied voltage was 200 V to maximize the electron drift velocity. The gas used was methane CH_4, which kept flowing during the measurements in order to assure its purity, despite the interactions with crossing ions and the impurities that may be produced by the walls and various components of the circuit. The gas flow also reduces the recombination and assures a good energy resolution.

3.4 Electronics and acquisition system

The scheme of the electronics used for processing the signals from the monitors, MCP, IC and Si detector is shown in Fig. 3.6. The signals from each monitor are fed to the preamplifier which gives as outputs time and energy signals. The energy

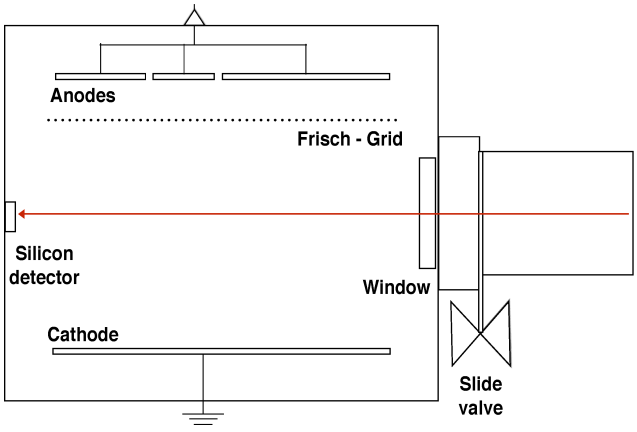

Figure 3.5. Scheme of ionization chamber with Frisch grid.

signals are connected to the inputs of a fast spectroscopy amplifier, then, the signal is sent to a linear gate stretcher and processed by the ADC. The time signals follow a different way, first, they are amplified and subsequently sent to a Constant Fraction Discriminator (CFD). The output signals of the CFD are sent to a gate generator and then to a logical unit, where the four monitor signals are put in OR with the time signal of the silicon detector placed in the IC. Each MCP provides a time signal. This signal is passed through a time pick-off pre-amplifier and fed into the CFD. The output signals of the CFDs are delayed and used as stop and/or start of the TAC module. Three TAC modules are currently in use providing three time of flight signals (TOF). Each TAC is started by the signal of the detector at a lower rate, in order to reduce the number of start signals not followed by a stop. Therefore, the signals of the MCP, conveniently delayed, provide the stop for the two TACs, measuring the time of flight between the first (second) MCP and the silicon detector, referred to as TOF1 (TOF3). Another TAC is employed to measure the time of flight between the two MCP (TOF2). The signal from the silicon detector is fed to the pre-amplifier, and then the energy signal is further amplified, sent to the linear gate stretcher and subsequently to the ADC. The time signal feeds a fast amplifier and subsequently a CFD. Two output signals of CFD are used as the start of TOF1 and TOF3, while a third one is sent to the gate generator. The output of this gate generator is sent in logical OR with monitors and the output of the logic unit provides the trigger which enables the data acquisition. The ionization chamber provides an energy signal which passes through a pre-amplifier followed by a fast spectroscopy amplifier. The output feeds the linear gate stretcher to be finally processed by the ADC.

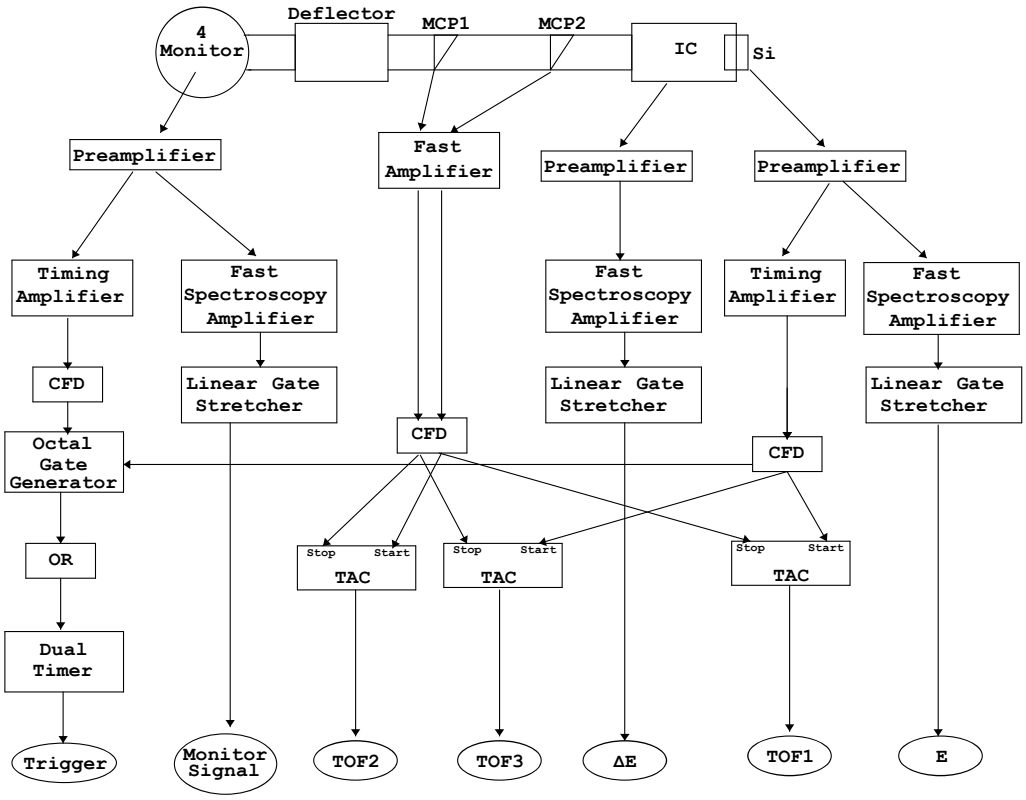

Figure 3.6. Scheme of the electronic chain of the set-up.

Chapter 4

AGATA and EUCLIDES set-up

Fusion cross sections were determined in a test experiment by detecting the prompt γ-rays using the gamma spectrometer AGATA placed at the close-up position (18 cm from the centre of the reaction chamber) in coincidence with the light charged particle evaporated by the compound nucleus, detected by the silicon-array EUCLIDES. For this test a ^{30}Si beam has been used, provided by the XTU Tandem accelerator at the energies of 47 MeV and 40 MeV, on a target 100 μg/cm^2 thick of ^{12}C placed at the centre of EUCLIDES.

4.1 The array of silicon detectors EUCLIDES

EUCLIDES [12] is an array of 40 two-stage ΔE-E silicon telescopes arranged in a 42-face polyhedron composed of 30 irregular hexagons and 12 regular pentagons (Fig. 4.1). The forward hexagonal detectors are placed at 30° with respect to the beam direction and are electrically segmented into 4 sectors with equal geometrical area. ΔE and E silicon detectors (Fig. 4.2) have $\sim$130 μm and $\sim$1000 μm thickness leading to capacitance values of 850 pF and 130 pF respectively. Both detectors cover the same area of $\sim$10.2 cm^2 and are separated by a 100 μm kapton spacer. A hexagonal or pentagonal frame of fibreglass, about 15 mm high is mounted behind each E detector. The full EUCLIDES structure is built by locking the neighbouring telescopes together by their frames through small Al bridges so that the distance between neighbouring telescopes is 0.2 mm. In this configuration, the distance from the target to the ΔE layer of the detectors is 62 mm and the whole EUCLIDES covers 81% and 80% of the solid angle for the ΔE and E respectively. The Si telescopes and the holding structure do not cause large γ-ray absorption or scattering.

The light charged particles are identified using the E-ΔE method, and the energy detected in the ΔE layer is combined with the total energy loss (E+ΔE), since the energy loss, as described by the Bethe-Bloch equation, is a function of the atomic number and the mass of the particle. Using E-ΔE spectra allows to distinguish

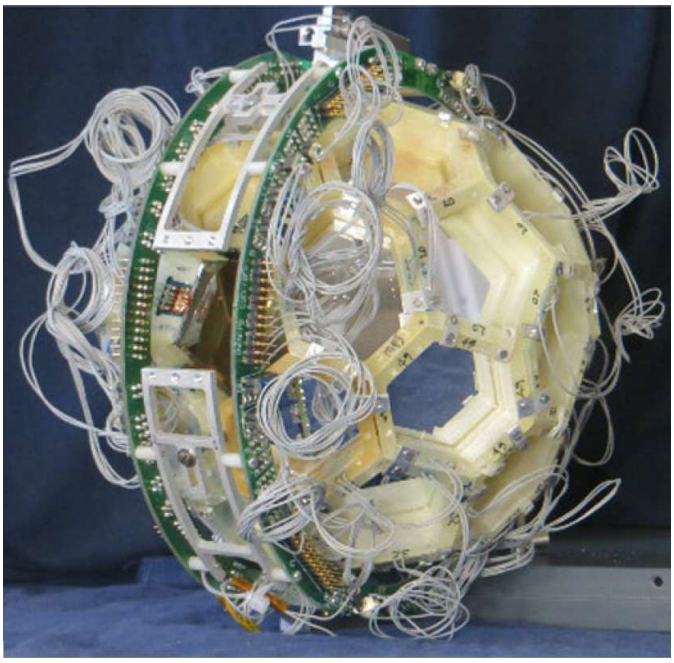

Figure 4.1. The EUCLIDES silicon array.

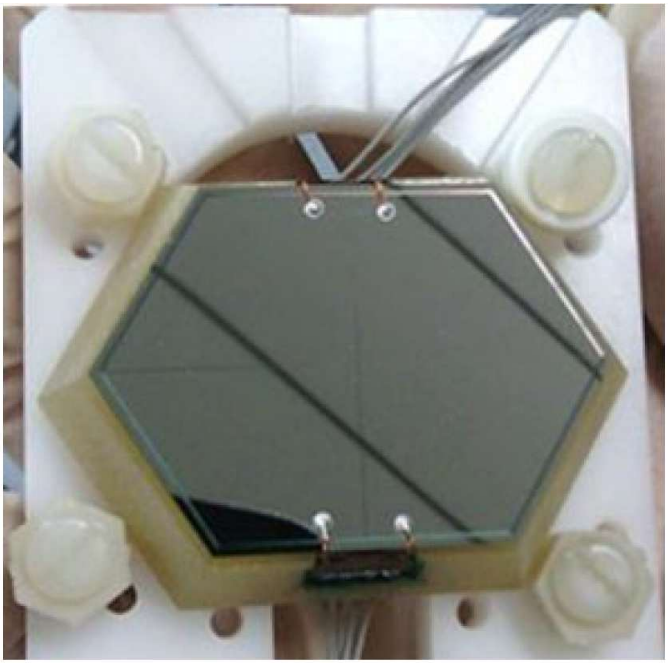

Figure 4.2. Picture of a two-stage ΔE-E telescope from the EUCLIDES silicon array.

between protons, deuterons and alpha-particles, as shown in Fig. 4.3. It should be noted that the deuterons observed in the spectra come from the contamination of the ^{12}C target, not from the evaporation process. Some of the low energy particles are stopped in the ΔE layer and are represented by the events in the diagonal because the particle never reaches the E layer. So, the total energy loss is equal to the energy loss in the ΔE layer. The most energetic particles can go through the E layer and not be stopped in the detector, however, even if that happens, such events can still be identified using the energy released in the telescope. As Si detectors are sensitive to

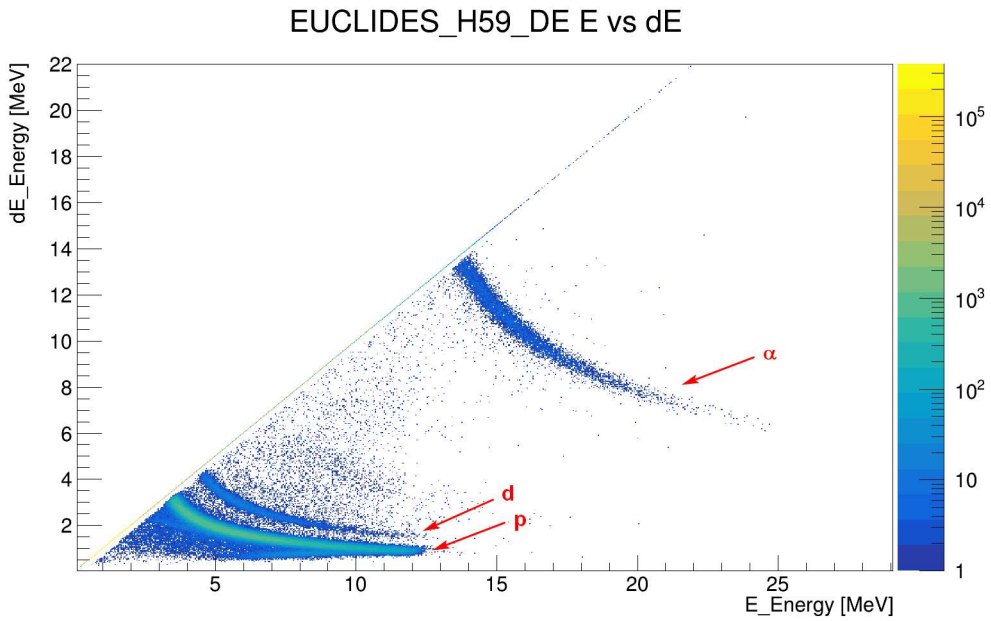

Figure 4.3. Energy loss vs total energy spectra from the detector H59 of EUCLIDES placed at 60° with respect to the beam direction.

radiation damage a 15 cm long aluminum cylindrical absorber has been placed inside EUCLIDES through the beam exit area to protect the detectors from the elastically scattered particles. In this experiment, only half of the absorber was used due to the inverse kinematics of the reaction where no elastic scattering occurs at backward angles. The thickness of the absorber has been chosen using LISE++ [31] and set to 12 μm. Also, a 7 μm Upilex-75S foil is permanently put in front of each telescope to guarantee the mechanical protection of the surface and its electrical insulation. For this experiment, the signals from the detectors of EUCLIDES were sent to 5 digitizers with 16 channels each and to another digitizer with only 8 channels for a total of 88 channels available. Since each regular EUCLIDES detector requires 2 channels (one for the E signal and one for the ΔE signal) and the segmented detectors require 8 channels it was possible to put in work only 4 segmented detectors and 28 regular detectors out of the 40 positions available for EUCLIDES. The removed detectors were

the five placed at 150° and two at 120° because these detectors have a lower counting rate, and one detector placed at 30° in order to have space for a monitor installed at that angle in the reaction chamber used to detect the elastically scattered particles to renormalize the fusion yield to the Rutherford cross section and monitor the beam current. A hole has been opened in the absorber in order to allow the monitor to correctly detect the elastic scattering. The granularity of EUCLIDES, when combined with a γ-spectrometer, also permits a good Doppler correction by reconstructing the full kinematic of the reaction; this leads to a significant improvement in the quality of the γ-ray spectra. The Doppler correction algorithm applied uses both the angular and energy information deduced from the EUCLIDES detectors. This algorithm is based on relativistic kinematics and uses momentum conservation to deduce the velocity vector of evaporation residues, assuming that the compound nucleus moves along the beam axis.

4.2 The γ-spectrometer AGATA

AGATA (Advanced GAmma Tracking Array) [11] is a γ-ray tracking array composed of High Purity Germanium (HPGe) crystals. The main characteristic of AGATA is

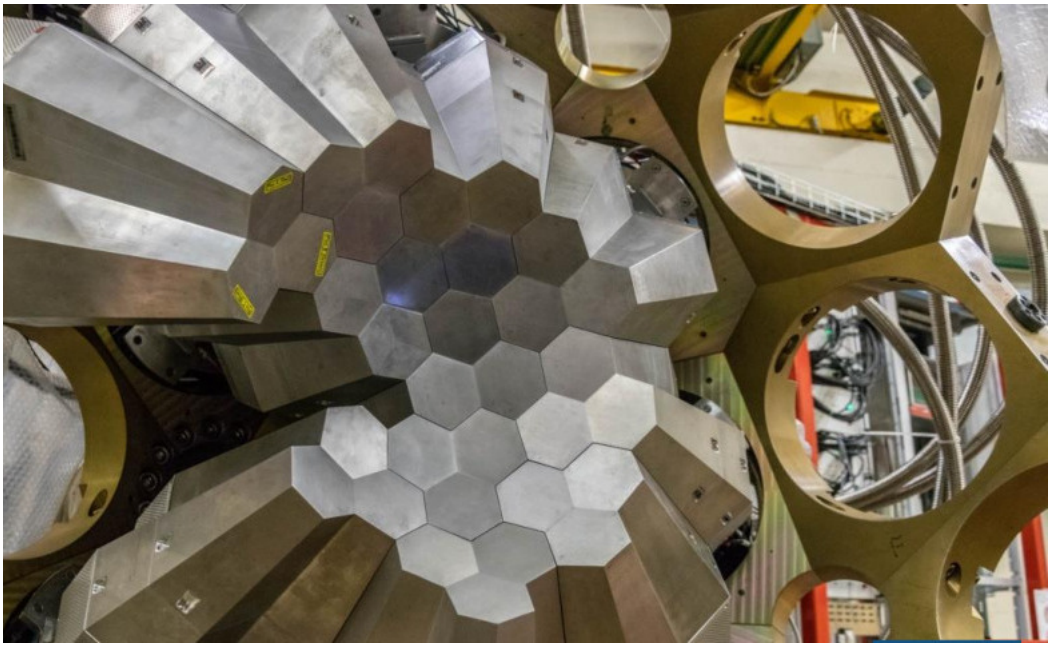

Figure 4.4. Picture of AGATA HPGe detector array at LNL.

the very precise estimation of the position of interaction of the photons (within 4 mm) by relying on the pulse shape from the segmented anodes [32]. This allows the implementation of γ-rays tracking algorithms to reconstruct the events from γ-rays

Compton scattering so that it is possible to reduce the background. This tracking technology, unlike the previous generation of γ detectors, does not require scintillators surrounding the germanium detector to suppress the Compton events. For this reason, the possibility of AGATA reconstructing events with multiple interactions also improves the overall efficiency of the set-up since the Compton suppressor scintillators are replaced with sensitive HPGe material. The high resolution of the interaction position also consents to achieve an improved Doppler correction.
Fig. 4.4 shows the AGATA detector at LNL. Each crystal that composes AGATA has been electrically segmented longitudinally and radially in 6 sections, for a total of 36 sections each (Fig. 4.5). The high degree of segmentation also allows us to sustain a higher counting rate compared to other detectors of the same size. All sections are different in shape because of the geometry of the detector, and in the centre of the germanium crystal, there is a common central contact. All crystals are arranged in clusters of three, called AGATA triple clusters (ATC) that share the same flange and the same dewar of liquid nitrogen. Each triple cluster is mounted on the AGATA honeycomb support with a 0.5 mm distance between two neighbouring detectors. For the AGATA detectors to work properly the germanium crystal has to be cooled to a temperature of about 80 K, which is reached using a cryostat for each triplet cluster with a system of periodic filling with liquid nitrogen.

The position of interaction of the γ-rays is determined by a pulse-shape analysis

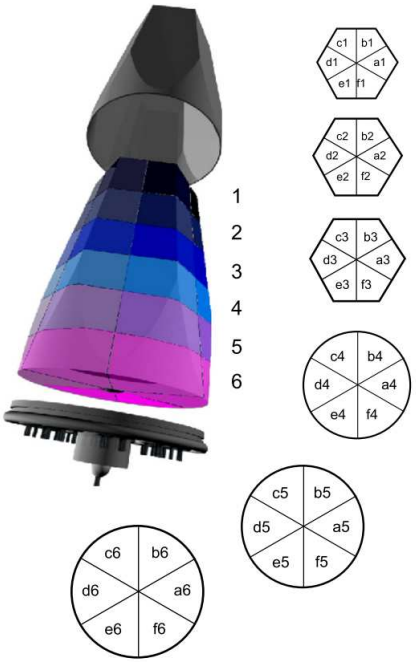

Figure 4.5. Representation of a crystal of HPGe of AGATA detector showing also a scheme of the 36 different sectors of each crystal (figure from [11]).

(PSA) [33]. This procedure consists in the comparison of the detected pulse shapes with a calculated reference basis for each sector, in real-time, minimizing the difference between the detected and reference signals. The working principle is based on the different mobility of the electrons and holes produced in the germanium crystal from the γ-rays interaction, so the shape of the signal obtained from the detector is dependent on the distance of the interaction point from the electrodes. In fact for a small distance from the core electrode, the faster electrons are collected immediately while the slower holes still have to drift to the segment electrode, resulting in a signal with a first part with a very low rise time (electron collection) and a second part with a higher rise time (hole collection). The shortest rise time occurs at an intermediate position, where the collection process for both signals is equal. Then for a larger distance from the core electrode, the time for the electrons to be collected is longer than for the holes, as they have to drift to the core electrode. The drifting charge in the hit segment also induces a signal in the neighbouring segment electrodes for every interaction, and the shape of the induced signal in a segment next to the hit segment is important because it gives us information on the angular and z positions. Depending on the distance of the interaction point to the non-hit electrode, the amplitude of the transient signal changes. An example of a simulated signal in AGATA is shown in Fig. 4.6 where the different shapes of the signal from the hit segment and the induced signal in the non-hit segment can be clearly seen. For this experiment,

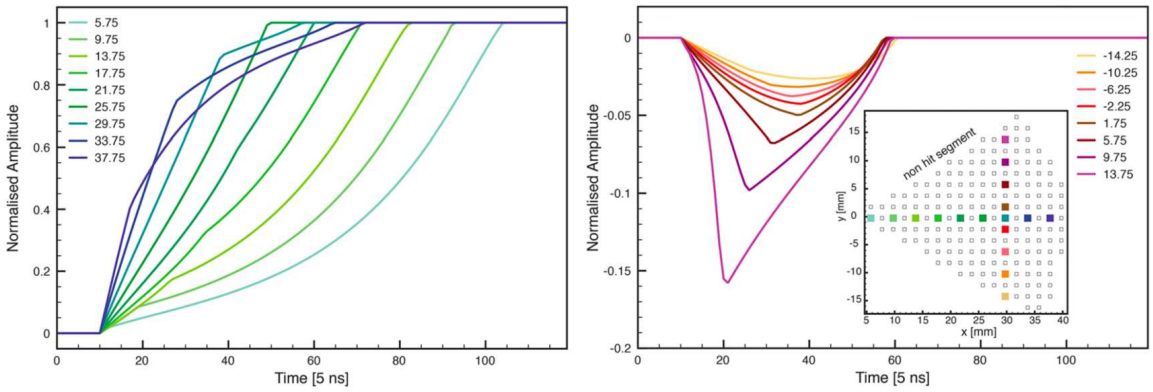

Figure 4.6. Simulated core signal for different distances from the core electrode (left), induced signal in the non-hit segment for different distances from the neighbouring segment (right), for a slice at 40.25 mm from the front of the detector (figure from [33]).

there were 11 AGATA triple clusters (ATC) mounted with a total of 32 HPGe crystals fully operative.

4.3 AGATA and EUCLIDES set-up

EUCLIDES has been placed inside the reaction chamber of AGATA, which is fixed to the PRISMA set-up (not used in this experiment). The chamber is a section of a sphere of radius of $\sim$ 170 mm with a thickness of 2 mm of aluminium. On the posterior part of the chamber, there is a movable beam dump that can rotate from 45° to 95°, Fig. 4.7 shows the whole set-up. In the experiment, the fusion cross section has been measured at two energies (47 MeV and 40 MeV), one above and one below the Coulomb barrier. Since the counting rate of the set-up was not high, the AGATA

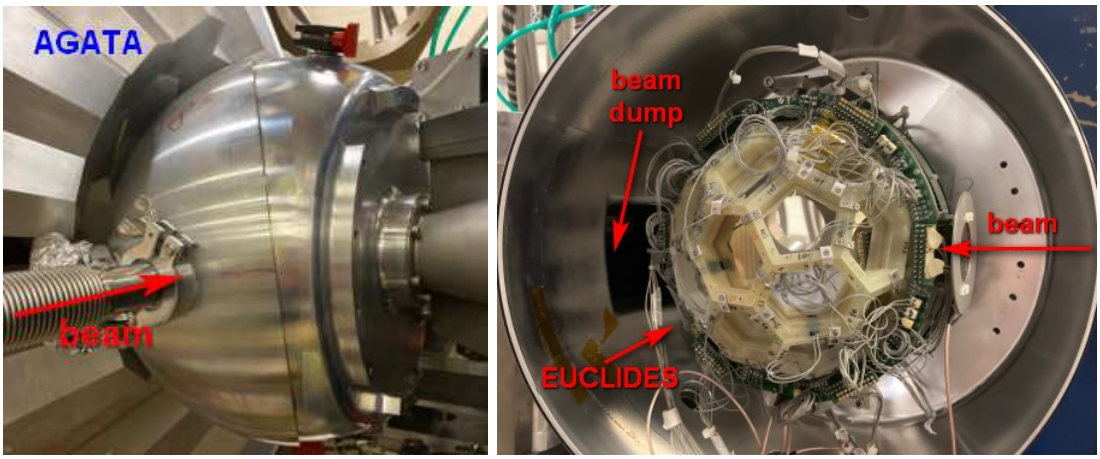

Figure 4.7. On the left there is the closed chamber with the AGATA detector placed at 18 cm from the target (close-up position), on the right there is the open chamber with EUCLIDES mounted inside.

array operated in standalone mode, measuring any γ-ray without any trigger request from the EUCLIDES detectors. The data were combined based on the timestamp (1 timestamp corresponds to 10 ns). During the data analysis, the events of AGATA in coincidence with EUCLIDES were selected with a time window on the timestamp difference as shown in Fig. 4.8. The chosen window (200 ns) was set from -10 to 10 timestamps corresponding to 20 timestamps.

4.4 PISOLO and silicon detectors

PISOLO can be used to measure fusion cross sections down to $\sim$1 μb. Below this limit, the fusion events are so rare that they cannot be distinguished from the beam-like particles. So to reduce the background and measure lower cross sections two silicon detectors have been placed inside the reaction chamber of PISOLO to detect the charged particles (protons, alphas) evaporated after the fusion process, in coincidence with the ER detected by PISOLO. The silicon detectors employed in the test are two

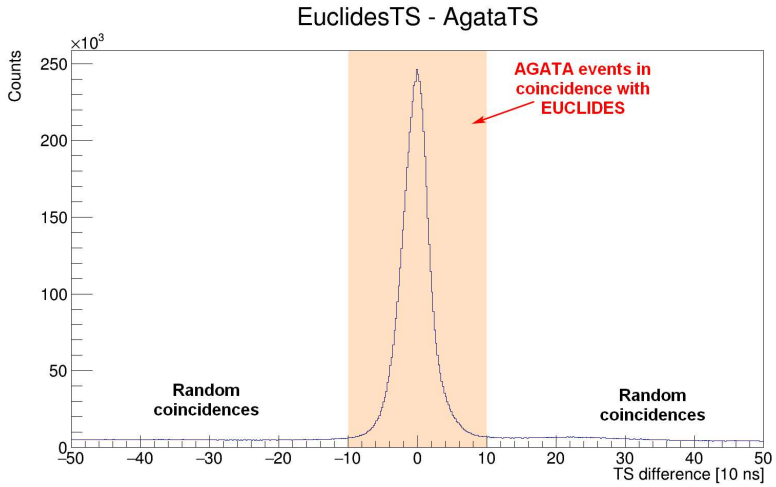

Figure 4.8. Timestamp difference between AGATA and EUCLIDES where the time window of 200 ns around the coincidence peak can be seen.

hexagonal detectors from the EUCLIDES set-up; these detectors are two-stage ΔE-E telescopes (Fig. 4.2) described in Sect. 4.1. The experiment has been performed using a beam of ^{30}Si from the XTU TANDEM accelerator on a target of ^{12}C of thickness 50 μg/cm^2 enriched to 99.8% in mass 12, at the energies of 47,40 and 37 MeV during three days of beam-time. The two EUCLIDES detectors have been placed at angles of 90° and 120° with respect to the beam direction on the reaction plane facing the target at a distance of 7 cm from it, while PISOLO has been rotated at -3° with respect to the beam direction. The adopted configuration is shown in Fig. 4.9. The purpose was to reduce the background in the PISOLO spectra, even at the cost of lower efficiency.
The electronic chain used to process the signals from PISOLO is the same as described in Sect. 3.4 with the addition of the electronic used for the two silicon detectors. The four signals coming from the two EUCLIDES detectors are fed to an 8-channel preamplifier shaper and timing filter that provides both an Energy signal that is directly sent to the acquisition system and a time signal used, in OR with the time signals from the four monitors and the silicon detector at the end of PISOLO, as the trigger of the acquisition. The time signal from the detector placed at 120° has been also used as the start for a TAC module, while the stop signal came from the PISOLO silicon detector.

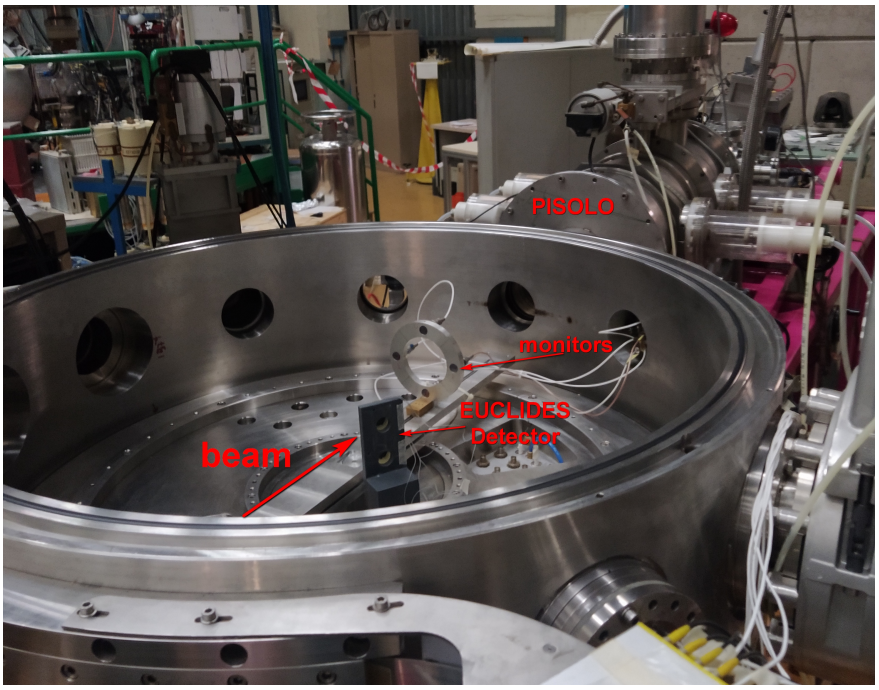

Figure 4.9. The reaction chamber of PISOLO with one of the two EUCLIDES detectors mounted inside the chamber.

Chapter 5

Data analysis of the ^{26}Mg + ^{12}C system

5.1 Experimental procedure

The first experiment with PISOLO was designed to perform a detailed measurement of the fusion excitation function for the ^{26}Mg + ^{12}C system and was run for eight days. This same system was measured in direct kinematics above the energy range investigated in the present work by Daneshvar et al. [34]. The XTU-Tandem accelerator provided the ^{26}Mg beam. The target consisted of 50 μg/cm^2 ^{12}C which introduced an average beam energy loss of around 0.33 – 0.4 MeV, which was taken into account in the analysis. The energies studied were in the range E_{lab} = 50 - 25.5 MeV. The ^{12}C target was mounted on the six-position target holder. The energy was gradually changed starting from the highest value, in order to minimize hysteresis phenomena in the analyzing magnet placed at the exit of the accelerator. At every energy change the beam was refocused on the target using a quartz. Fusion cross sections have been determined by direct detection of the fusion evaporation residues (ER) by separating them from the beam particles using the electrostatic deflector. The voltage applied to the electrodes was tuned during the experiment to maximize the number of ER detected after the deflector stage (yield of ER). The yield measurement was performed at the highest energy (50 MeV), in the range V = 31 - 25 kV, and the maximum transmission was reached at the voltage of ±27.0 kV on each deflector electrode. For the other beam energies, the applied voltage was scaled for the estimated electrical rigidity of the ER. The whole set-up was at first placed at an angle of +2° with respect to the beam direction and then moved to angles of +3° and +4° for the lower energies, in order to reduce the background of beam-like particles compared to the number of ER. Four silicon detectors were placed in the reaction chamber symmetrically around the beam direction at the same scattering angle (16°) and have been used to monitor the beam and to normalize the fusion yields to the Rutherford scattering cross

section.

5.2 Total fusion cross section and excitation function

An example of TOF_1-E and TOF_1-ΔE matrices for different energies can be seen in Fig. 5.1. When the energy is far below the barrier, the number of ER compared to

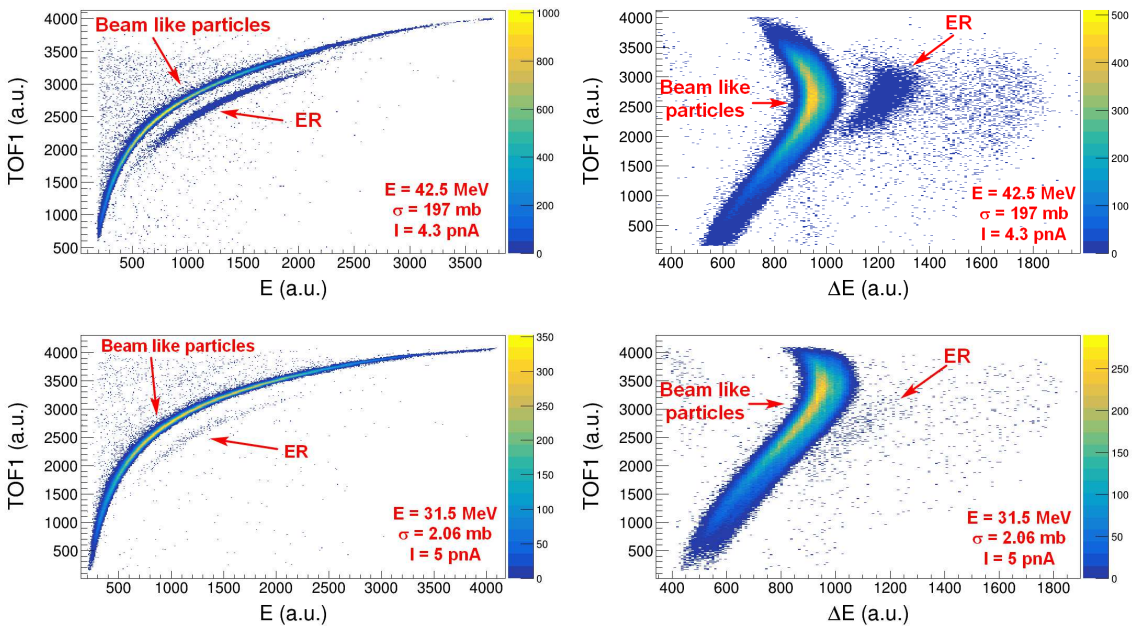

Figure 5.1. Example of TOF_1-E (left panels) and TOF_1-ΔE (right panels) spectra for energies of 42.5 MeV, above the Coulomb barrier (top), and of 31.5 MeV below the barrier (bottom).

background events decreases rapidly. The identification of ER becomes, therefore, more difficult making it necessary to apply software conditions in order to remove the background. The ER are identified by using the various independent parameters (two TOF, ΔE and E) that are measured. An example of a spectrum with software condition is shown in Fig. 5.2 where the spectra TOF_1-ΔE without and with a condition on the TOF_1-E spectra are shown. The ER events are clearly visible once the software condition has been applied while they were almost indistinguishable from the background before. Examples of the spectra provided by the four monitors at the energy of 30 MeV are shown in Fig. 5.3. These spectra allow us to measure the number of elastic scattering events, which is used to normalize the fusion cross section to the Rutherford cross section. The monitors allow also to correct for the variations

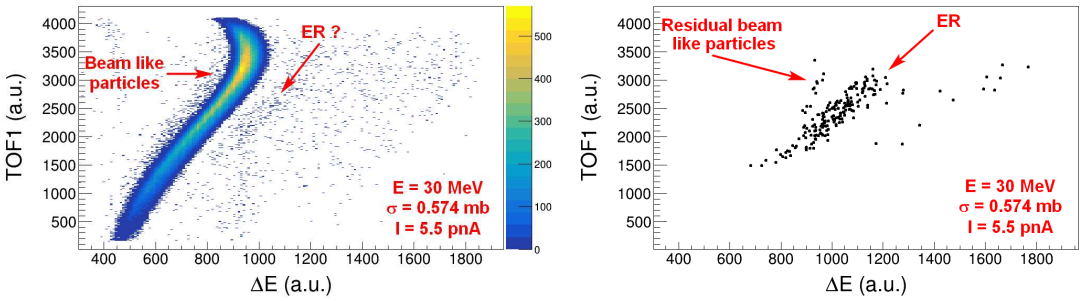

Figure 5.2. Example of TOF_1-ΔE without (left panel) and with (right panel) a condition on the TOF_1-E spectra at the energy of 30 MeV, below the Coulomb barrier.

of beam conditions that may change during long data acquisitions.

The ER angular distribution was also measured at two energies of E_{lab} = 43.5 MeV

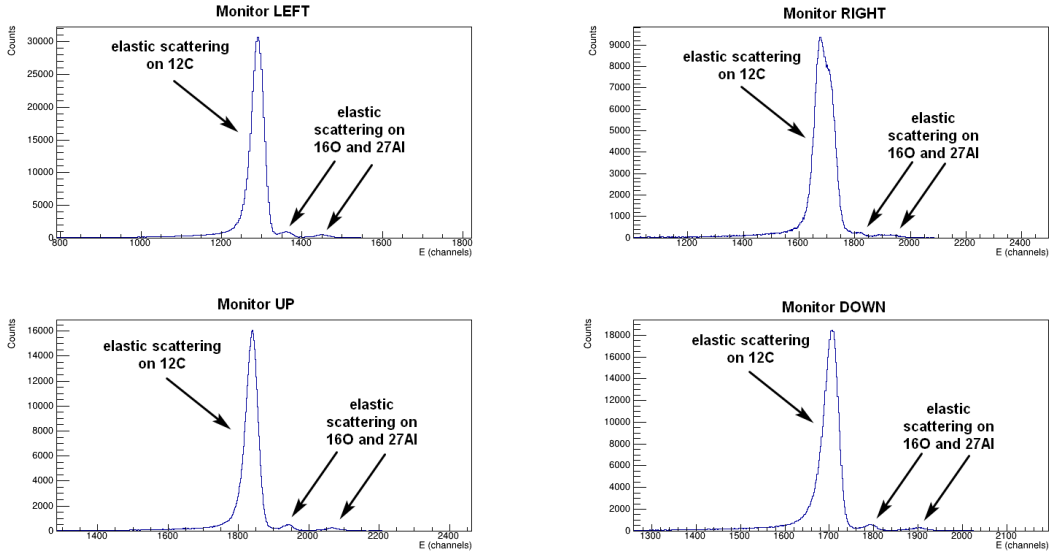

Figure 5.3. Examples of the spectra provided by the four monitors for the energy of 30.0 MeV

and E_{lab} = 36.5 in order to obtain the total fusion cross section. The differential fusion cross section can be obtained from the ER and monitors counts by the formula:

$$\frac{d\sigma_f}{d\Omega}(E,\theta) = \frac{d\sigma_{Ruth}}{d\Omega}(E,\theta_{lab})\frac{N_{ER}}{N_{mon}}\frac{\Delta\Omega_{mon}}{\Delta\Omega_{ER}}\frac{1}{\epsilon} \tag{5.1}$$

where N_{mon} is the number of elastic scattering events detected by the monitors, $\Delta\Omega_{mon}$ is the total solid angle subtended by them and θ_{lab} is the monitor angle (16°). N_{ER}

is the number of ER obtained from the PISOLO spectra and $\Delta\Omega_{ER}$ is the solid angle covered by the silicon detector at the end of the telescope. The quantity ϵ can be explicitly expressed as the product of the deflector transmission T = 0.82±0.03 and the telescope transparency. The telescope transparency depends on the grids of the two MCP (0.85±0.03 each) and the mesh that supports the window of the IC (0.80±0.01). The value of T was estimated by interpolating the values previously obtained for several different systems. T does not essentially depend on the energy, however, it is a function of the mass asymmetry of the system under study. The total fusion cross section for each energy can be obtained by integrating the differential cross section on the whole solid angle. This can be done by fitting the angular distribution measured with PISOLO and then integrating the fitting function. Since the ER angular distribution depends on the evaporated particle, the experimental data have been fitted using two Gaussians, one reproducing the evaporation of light particles (neutron or proton) and one reproducing the evaporation of alpha particles. The angular distribution obtained for the energy of 43.5 MeV is shown in Fig. 5.4. At small angles, the spectra from PISOLO become very noisy making it not possible to correctly separate the ER from the beam-like particle. Therefore, the differential fusion cross section was not reliably estimated at angles lower than 2°. The angular

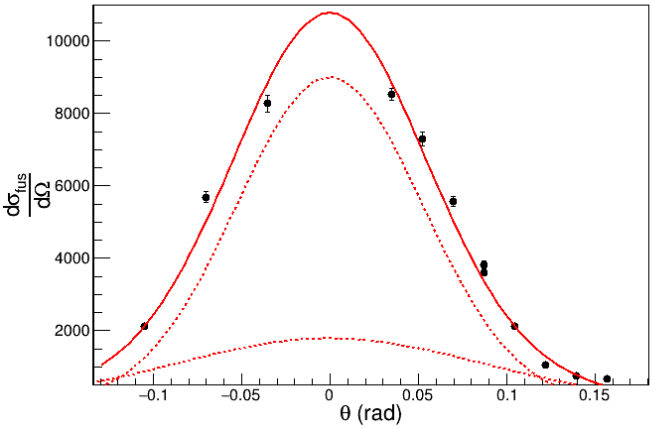

Figure 5.4. Angular distribution for the system ^{26}Mg + ^{12}C at the energy of 43.5 MeV. The solid line is the function corresponding to the sum of the two Gaussian used to fit the data (dashed lines)

distributions are fitted and then integrated on the whole solid angle by the formula:

$$\sigma_f = \int \frac{d\sigma_f}{d\Omega}(E,\theta)d\Omega = 2\pi \int_0^{\pi} \frac{d\sigma_f}{d\Omega}(E,\theta)sin(\theta)d\theta \tag{5.2}$$

The angular distribution has not been measured at very low energies, since it would take too much time to obtain the differential cross section at large angles.

Nevertheless one can notice that the value of the ratio between the total cross section and the differential cross section $K(E,\theta)$ is a quantity weakly dependent on the energy and can be considered constant for a fixed angle of PISOLO. It follows that the value of $K(\theta)$ can be extracted for the energies where the angular distribution has been measured and used to obtain the total cross section for the lower energies by the formula:

$$\sigma_f = K(\theta)\frac{d\sigma_f}{d\Omega}(E,\theta) \tag{5.3}$$

The resulting cross sections are reported in Table 5.1 and shown in Fig. 5.5

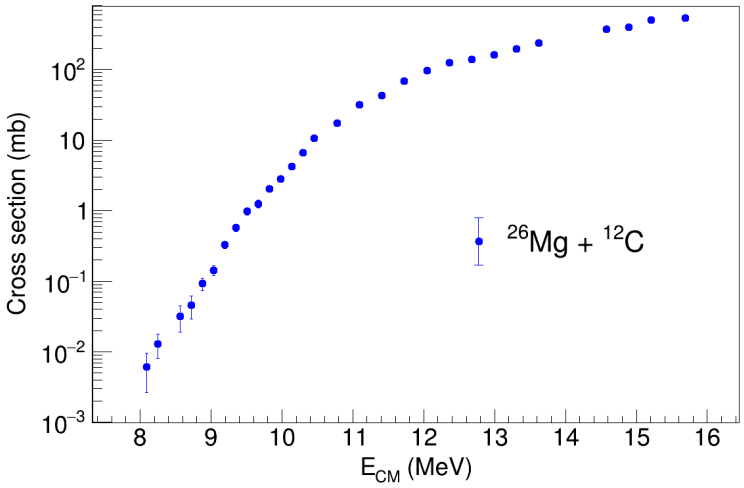

Figure 5.5. Total fusion cross section for the ^{26}Mg + ^{12}C system.

The relative uncertainties depend only on statistics. Since the distribution of the particle counts N is Poissonian the associated uncertainty is $\sqrt{N}$. The cross sections vary by five orders of magnitude in the energy range of the measurements.

5.3 Astrophysical S-factor and logarithmic slope

A first approach to verify the behaviour of this system at low energies is extracting the Logarithmic derivative L(E) and the Astrophysical S factor S(E). The logarithmic derivative (slope) is defined as

$$L(E) = \frac{dln(E\sigma)}{dE} \tag{5.4}$$

that can be obtained from a pair of experimental data using the incremental ratio:

Table 5.1. Cross sections measured in this experiment for the ^{26}Mg + ^{12}C system, the quoted errors are statistical uncertainties (see text).

E_{CM}	σ_f
15.69	533 ± 23
15.21	505 ± 23
14.89	400 ± 26
14.58	375 ± 33
13.63	240.1 ± 9.2
13.31	197 ± 12
12.99	160 ± 10
12.68	140.6 ± 9.1
12.36	124.7 ± 6.2
12.04	96.7 ± 6.1
11.73	69.1 ± 4.4
11.41	43.2 ± 3.2
11.09	32.0 ± 2.3
10.78	17.5 ± 1.4
10.46	10.68 ± 0.79
10.30	6.69 ± 0.56
10.14	4.24 ± 0.33
9.99	2.85 ± 0.19
9.83	2.06 ± 0.22
9.67	1.26 ± 0.16
9.51	0.99 ± 0.12
9.35	0.574 ± 0.071
9.19	0.332 ± 0.039
9.03	0.144 ± 0.023
8.88	0.093 ± 0.019
8.72	0.069 ± 0.014
8.56	0.032 ± 0.013
8.24	0.0130 ± 0.0049
8.09	0.0062 ± 0.0035

$$L(E) = \frac{ln(E_2\sigma_2) - ln(E_1\sigma_1)}{E_2 - E_1} \tag{5.5}$$

The statistical uncertainty associated with the logarithmic derivative is estimated by propagating the statistical uncertainty of the cross section. The results are shown in Fig. 5.6 where the value of $L_{CS} = \frac{\pi\eta}{E}$ is also plotted and reported in Table 11.1. From

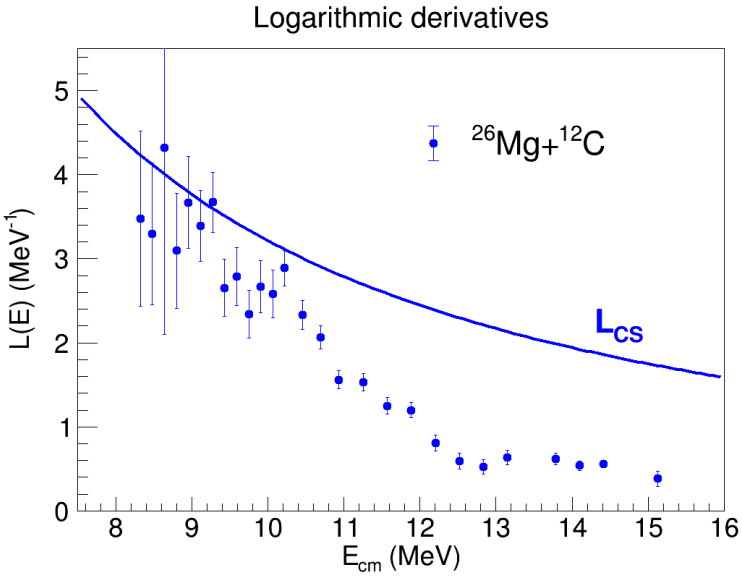

Figure 5.6. Logarithmic derivative for the ^{26}Mg + ^{12}C system.

this plot, it can be seen that the experimental value of L(E) reaches the L_{CS} value (blue line) but then the slope seems to decrease again. Due to the large errors in the logarithmic slope, there is no clear evidence of the hindrance effect for this system. The trend at very low energies also presents some slope oscillations.
The astrophysical S factor has been calculated from the cross section values as:

$$S(E) = E\sigma(E)e^{2\pi(\eta-\eta_0)} \tag{5.6}$$

The parameter η_0 has been used as a normalization factor to obtain S(E) in a reasonable range of values. In this case, $\eta_0 = 9.55$ has been used. As for the logarithmic derivative, the statistical uncertainty for S(E) is estimated by propagating the statistical errors on the cross sections. The results are shown in Fig. 5.7 and reported in Table 11.2. It can be seen that there is no clear maximum for S(E), in accordance with the trend of L(E), but the S-factor also presents some oscillations at low energies. So this system does not present a large cross section at the hindrance threshold as observed in ^{24}Mg + ^{12}C. To correctly understand the experimental results, a theoretical interpretation is necessary. In this thesis, a coupled-channels analysis has been performed using the CCFULL code [24].

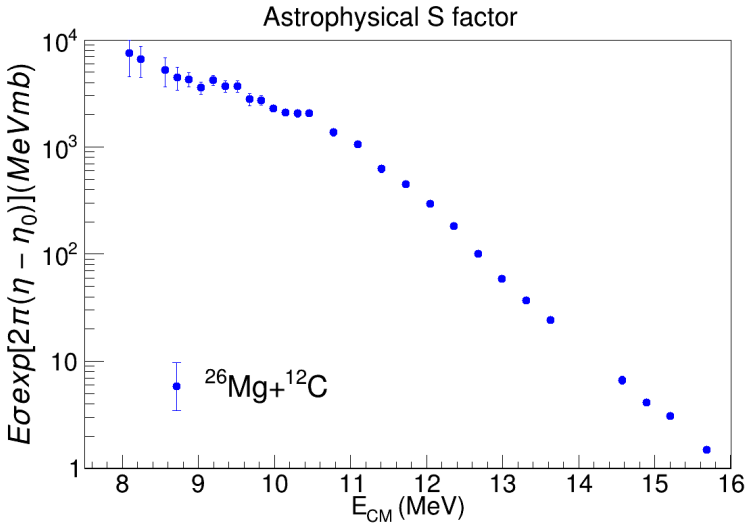

Figure 5.7. Astrophysical S factor for the system ^{26}Mg + ^{12}C

Chapter 6

Comparison with CC calculations

The experimental data on ^{26}Mg + ^{12}C have been compared to the calculations based on the coupled channels model. The comparison is of great importance to verify the effect of the excited states involved in the fusion dynamics. The CC calculations were performed by means of the CCFULL code, which solves the coupled equations by employing the isocentrifugal approximation and the incoming wave boundary condition. The energies of the excited states of ^{26}Mg, as well as the associated deformation parameters, are given in Table 6.1 [35, 36], while ^{12}C has been considered inert since its contribution is already taken into account by the renormalization of the nuclear potential needed to best fit the data near the Coulomb barrier. The parameters of the Akyüz-Winther potential are reported in Table 6.2 (first line).

Table 6.1. Nuclear structure parameters for CCFULL calculations.

Nucleus	E(MeV)	λ^{π}	β_{λ}
^{26}Mg	1.809	2^+	0.482
	6.876	4^+	0.214

Table 6.2. Well depth V_0, radius parameter r_0, diffusivity a_0 of the Akyüz-Winther potential and resulting height V_b and position R_b of the Coulomb barrier for the system ^{26}Mg+^{12}C. The second line shows the parameters of the modified potential (see text)

V_0 (MeV)	r_0 (fm)	a_0 (fm)	V_b (Mev)	R_b (fm)
43.52	1.17	0.61	11.3	8.45
41.65	1.10	0.61	11.9	9.51

6.1 Results of calculation

The resulting fusion cross section overestimates the experimental data above the Coulomb barrier. This effect may be caused by an underestimation of the Coulomb barrier by the Akyüz-Winther potential. In order to correct for this effect the barrier height has been modified to $V_b = 11.9$ MeV, and following this modification, the well depth of the nuclear potential has to be $V_0 = 41.65$ MeV and the radius $r_0 = 1.10$ fm, with the same $a_0 = 0.61$ fm (see the second line of Table 6.2).

The coupled channel calculations are shown in Fig. 6.1: the couplings lead to an enhancement of the fusion below the barrier with respect to the no coupling limit, and the results seem to overestimate the cross sections at low energies even if there is no clear evidence of hindrance for this system as discussed above. The results of the coupled channel calculation are in good agreement with the experimental data at energies above and slightly below the Coulomb barrier. At very low energies the behaviour of the theoretical predictions is just slightly different from that of the experimental data, so that, there is not a clear maximum for the S-factor.

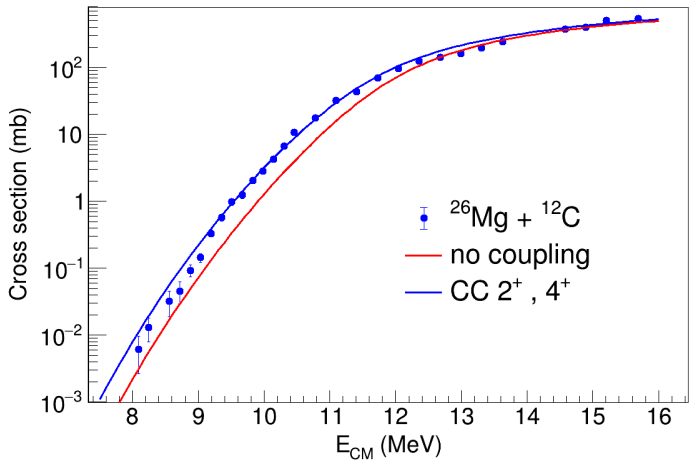

Figure 6.1. CC calculations of the excitation function with the modified potential for the system ^{26}Mg + ^{12}C.

The logarithmic derivative (Fig. 6.2) and the astrophysical S factor (Fig. 6.3) have been calculated and compared with the experimental data. As expected the experimental values of the logarithmic derivative follow the theoretical predictions at high energies. Still, even if, at lower energies, the measured slope reaches the L_{CS} value it decreases again following the theoretical prediction (red line), so there is no clear evidence of the presence of the hindrance effect due to the oscillation of L(E) and the small difference between the L_{CS} value and the CC calculation. Consequently, there is no clear maximum for the astrophysical S-factor that seems to follow the

theoretical prediction.

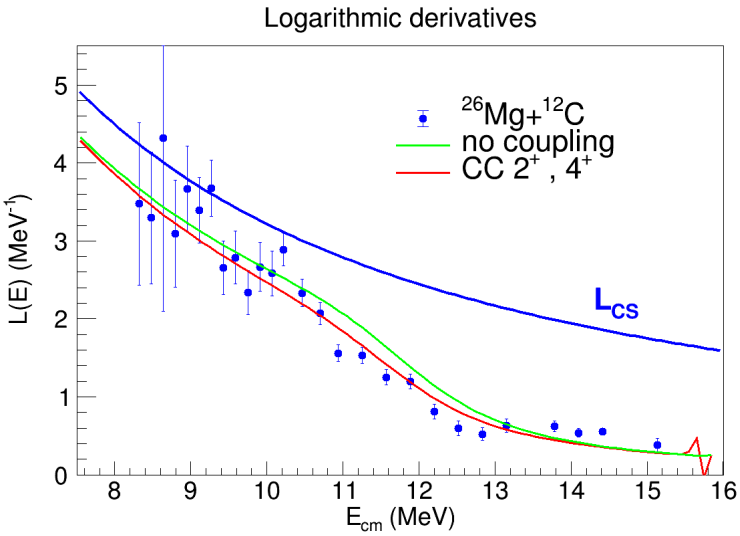

Figure 6.2. CC calculations of the logarithmic derivative for the system ^{26}Mg + ^{12}C.

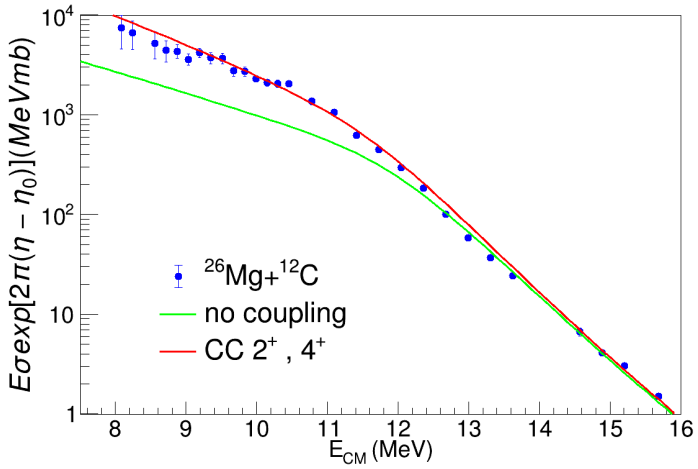

Figure 6.3. CC calculations of the astrophysical S factor for the system ^{26}Mg + ^{12}C.

The experimental data are not well reproduced at very low energies by the no coupling calculations at variance with ^{24}Mg + ^{12}C. To understand more clearly the behaviour of ^{26}Mg + ^{12}C precise measurements at even lower energies are needed.

6.2 Comparison of ^{26}Mg+^{12}C and ^{24}Mg+^{12}C

^{24}Mg+^{12}C is a nearby system with a positive Q-value (+16.3 MeV). The nucleus ^{24}Mg has a large prolate deformation ($\beta_2 = 0.60$), similar to the ^{26}Mg ($\beta_2 = 0.48$), but presents also an alpha-like structure (unlike ^{26}Mg where two additional neutrons are found). The lowest 2^+ states are found at $E_x = 1.369$ MeV in ^{24}Mg and at $E_x = 1.809$ MeV in ^{26}Mg, in both cases the octupole excitation is weak and very high. The analysis of ^{24}Mg+^{12}C fusion shows two peculiar features that are not observed in similar systems. The fusion cross section at the hindrance threshold is very high ($\sigma = 0.75\ mb$) and the experimental data seem to be well reproduced at very low energies by the no coupling calculation (as shown in Fig. 1.2 of Chapter 1). The excitation function has been reproduced with two methods, the first one using an empirical formula (Eq. 6.1) in the spirit of the adiabatic model [10] assuming that at energies far below the barrier, the coupling strength is completely damped:

$$ln(\sigma_{exp}) = \beta(E) ln(\sigma_{CC}) + (1 - \beta(E)) ln(\sigma_{NC}) \tag{6.1}$$

where σ_{CC} is the cross section predicted by the coupled-channels calculation, σ_{NC} is the excitation function for the no coupling limit and $\beta(E)$ is an empirical function that should be close to 1 near the barrier and close to 0 at low energies. $\beta(E)$ can be obtained at each measured energy and its energy dependence can be fitted with a Fermi function:

$$\beta(E) = \frac{1}{1 + e^{\alpha_0 (E - E_0)}} \tag{6.2}$$

The result of the fit is shown in Fig. 6.4 and the obtained parameters are α_0 = -2.728 MeV^{-1} and $E_0 = 9.594$ MeV. The fitted β(E) function used in Eq. 6.1 allows to reproduce the excitation function of the system and the S factor (blue line in Fig. 1.2 of Chapter 1). The maximum for the S factor is well reproduced and at the lowest energies, S increases again following the no-coupling calculation.

The second method to reproduce the data is based on a parameterization of the logarithmic slope that reproduces the data of several systems with positive fusion Q-value, in which the hindrance effect has been observed [7]:

$$L(E) = A_0 + \frac{B_0}{E^{3/2}} \tag{6.3}$$

As a consequence, the low energy excitation function can be written as:

$$\sigma(E) = \frac{\sigma_s E_s}{E} exp\left(A_0 (E - E_s) - \frac{2B_0}{\sqrt{E_s}} \left(\sqrt{\frac{E_s}{E}} - 1 \right) \right) \tag{6.4}$$

where E_s is the hindrance threshold and σ_s is the cross section at $E = E_s$. The low energy cross sections for ^{24}Mg+^{12}C have been fitted using Eq. 6.4 obtaining A_0 = -4.62 MeV^{-1}, $B_0 = 239.6$ MeV$^{1/2}$, $E_s = 9.67$ MeV and $\sigma_s = 0.75$ mb. The result is

the red line shown in Fig. 1.2 of Chapter 1, which reproduces very well the data and the maximum of the S factor.

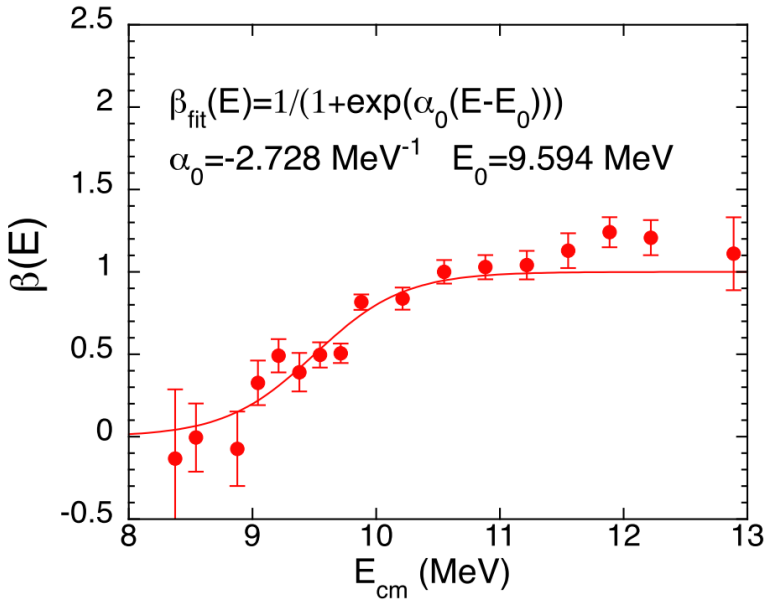

Figure 6.4. $\beta(E)$ obtained from the experimental data and fitted with a Fermi function.

Both methods reproduce the data in the studied energy range in the experiment but their behaviour at lower energies is very different; this can be seen clearly by observing the S factor. Indeed the empirical formula predicts an increase of the S factor at very low energies following the no coupling limit, while according to the hindrance, the S factor should keep decreasing at lower energies.

The results obtained with the system ^{26}Mg +^{12}C could give important information to better understand the behaviour of the ^{24}Mg + ^{12}C system, indeed, as already shown in Sect. 5.2, ^{26}Mg + ^{12}C does not present a large value of the excitation function at the hindrance threshold and the cross section at very low energies is about four times larger compared with the ^{24}Mg + ^{12}C. The reason behind the different value of the cross section at the hindrance threshold may be attributed to the alpha-like structure of the ^{24}Mg not presented by the ^{26}Mg. In any case, an unambiguous theoretical interpretation is still missing. As a consequence of the higher hindrance threshold, the excitation function of the ^{24}Mg + ^{12}C decreases more rapidly compared with the ^{26}Mg + ^{12}C, this becomes even more evident when looking at the different behaviour of the S factor at very low energies for the two systems, as shown in Fig. 6.5. Also, the experimental points of ^{26}Mg+^{12}C are not well reproduced by the no coupling limit even at very low energies. The reason may be again the different hindrance threshold. Anyway, both systems present some oscillation at low energy, as can be indeed seen

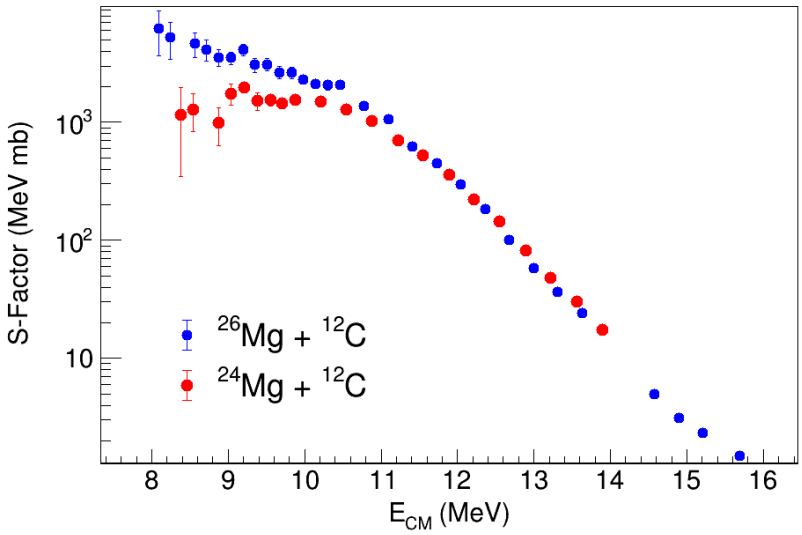

Figure 6.5. Astrophysical S-factor for the two systems ^{24}Mg + ^{12}C (red) and ^{26}Mg + ^{12}C (blue).

looking at the logarithmic slope L(E) where two peaks are clearly present for both systems. This phenomenon is more accentuated for ^{24}Mg + ^{12}C and does not have yet a theoretical explanation. Still, it could be related to the oscillation in the fusion cross section observed in the ^{12}C + ^{12}C [3] and ^{16}O + ^{12}C [37] systems. For ^{16}O + ^{12}C this behaviour has been associated with the α elastic transfer and recently also with quasi-molecular resonances [37], while for the system ^{12}C + ^{12}C the oscillations have been associated with quasimolecular resonances [38, 39] and recently also with the low level density of the compound nucleus ^{24}Mg [40]. In fact, these oscillations in the excitation function can be observed for ^{12}C + ^{12}C but not for the system ^{12}C + ^{13}C (as shown in Fig. 6.6 right panel), suggesting that they originate from the low level density of the compound nucleus ^{24}Mg [40] for ^{12}C + ^{12}C. The level density as a function of the excitation energy for the two CN ^{24,25}Mg is shown in Fig. 6.7. For ^{12}C + ^{12}C, the oscillations show up in the S-factor while in the ^{26}Mg +^{12}C case, this behaviour is clearly visible only in the logarithmic derivative (Fig. 6.6 left panel).

At this point it is clear that to better understand the behaviour of both the ^{24,26}Mg + ^{12}C systems one needs to perform measurements of fusion cross section at even lower energies. Therefore, the possibility of employing coincidences between the light evaporated charged particles and prompt γ-rays using AGATA and EUCLIDES, has been tested. The further possibility of using the coincidence between the light charged particles and the ER has been tested by installing in the PISOLO reaction chamber two silicon detectors from the EUCLIDES array, in order to remove most of the background from the PISOLO spectra and extend the measurable cross section down to the range of hundreds of nanobars.

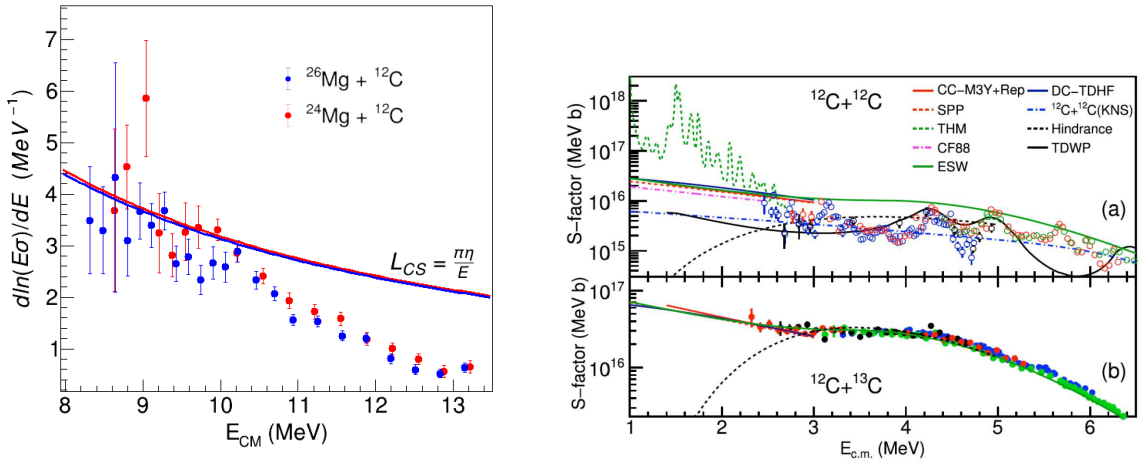

Figure 6.6. Logarithmic slope for the systems ^{24}Mg+^{12}C (red) and ^{26}Mg+^{12}C (blue) (left panel). Astrophysical S-factor for the two systems ^{12}C+^{12}C (above) and ^{12}C + ^{13}C (right panel). No oscillations (and no hindrance) are observed for the ^{12}C + ^{13}C (figure from [41]).

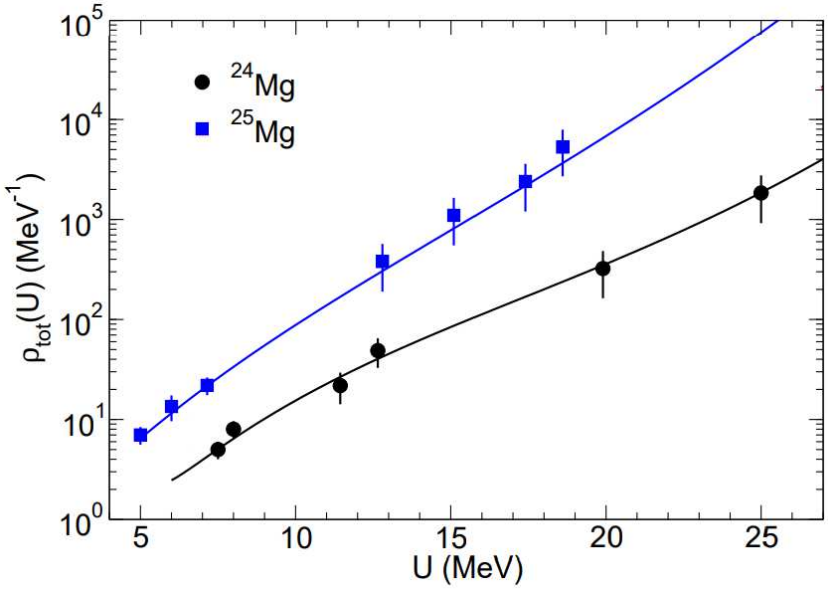

Figure 6.7. Level density for ^{24}Mg and ^{25}Mg as a function of the excitation energy U (figure from [40]).

Chapter 7

PISOLO and Silicon detectors Test

The PISOLO set-up can measure fusion cross sections down to 1-0.5 μb, so in order to approach the energy range of interest for astrophysics it is necessary to improve its sensitivity. To this end, two detectors of the EUCLIDES have been placed inside the reaction chamber of PISOLO as described in Sect. 4.4 to detect the light charged particles evaporated from the compound nucleus in coincidence with the ER detected by PISOLO. The system ^{30}Si + ^{12}C, which is another system with a positive fusion Q-value (Q = 14.1 MeV), has been used. The beam, provided by the XTU Tandem accelerator, was ^{30}Si at the energies of 47, 40 and 37 MeV on a target of enriched ^{12}C 50 μg/cm^2 thick placed on the target holder in the PISOLO reaction chamber. The target introduced an average beam energy loss of around 0.45 MeV, which was taken into account in the analysis. The experimental procedure is similar to what is described in chapter 5 for the ^{26}Mg+^{12}C system. Also in this test, the voltage applied to the electrodes was tuned to maximize the number of ER (yield) detected after the deflector stage. The yield measurement was performed at the highest energy (47 MeV), in the range V = 28 - 20 kV, and the maximum transmission was reached at the voltage of $\pm$ 23.0 kV on each deflector electrode. For the other beam energies, the applied voltage was scaled for the estimated electrical rigidity of the ER.

An example of a spectrum from the EUCLIDES detector placed at 120° from the beam direction can be seen in Fig. 7.1. The protons can be clearly identified while the α-particles are not energetic enough to go through the ΔE layer. Anyway, since the purpose of the experiment was the measurement of the total fusion cross section the proton-α discrimination is not crucial.

7.1 Experimental procedure

Examples of spectra obtained from PISOLO in this experiment can be seen in Fig. 7.2. From the spectrum TOF$_1$-ΔE the different evaporation channels can be distinguished because of the different atomic numbers Z of the ER that cause a different energy

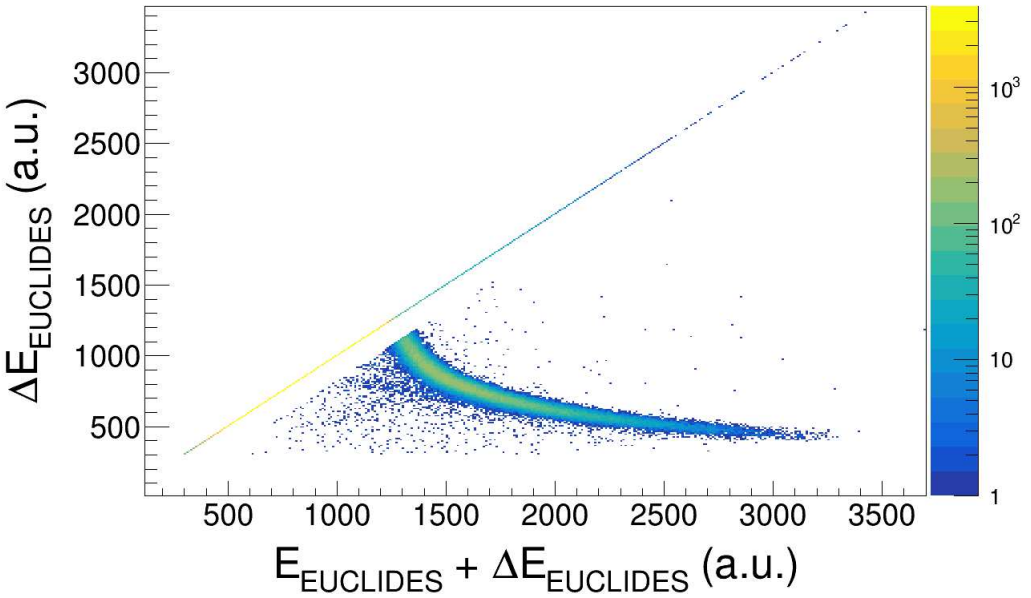

Figure 7.1. Spectrum of ΔE-E_{tot} from the detector placed at 120° from the beam direction.

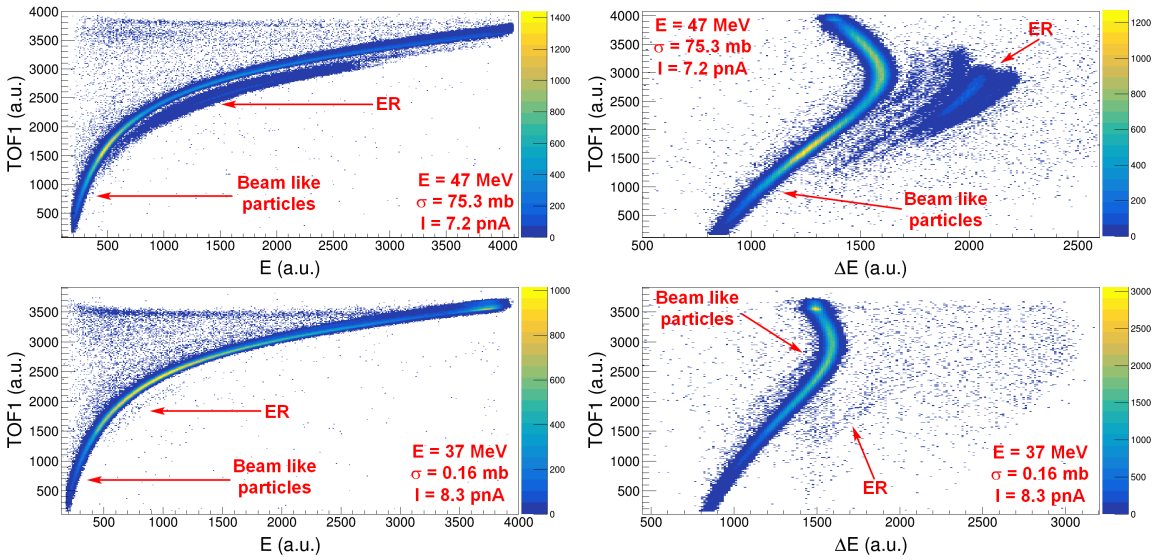

Figure 7.2. Example of TOF_1-E (left panels) and $TOF_1 - \Delta E$ (right panels) spectra for the energies of 47 MeV (top) and 37 MeV(bottom).

loss in the ionization chamber. Fig. 7.3 (left) shows the spectrum TOF_1-ΔE, with a condition on the spectrum TOF_1-E to remove most of the background, at 47 MeV. The evaporation channels with different atomic numbers are clearly separated. This

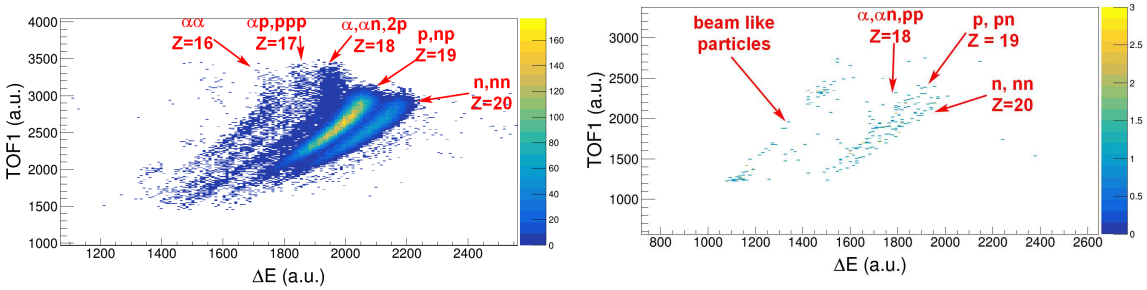

Figure 7.3. Example of $TOF_1 - \Delta E$ spectrum with a condition on the spectrum TOF_1-E at the energy of 47 MeV (left) and 37 MeV (right) where the evaporation channels with different Z can be distinguished.

can be observed because $^{30}Si + ^{12}C$ is a light system and because of the improvement of the energy resolution of the ionization chamber compared with the experiment on $^{26}Mg + ^{12}C$. The identification of evaporation channels is useful to compare these results with those obtained in the test with AGATA and EUCLIDES (chapter 8) since both tests have been performed for the same system. In table 7.1 the numbers of events for the different atomic numbers are presented for the energy of 47 MeV and PISOLO placed at 3°, where it can be observed that the main evaporation channels are 1p and 1p1n and that the lowest observed atomic number is Z = 16 corresponding to the evaporation channel of 2 α. At 40 and 37 MeV the evaporation channels of two

Table 7.1. Different evaporation channels recognized in the ionization chamber at the energy of 47 MeV.

Z	evaporation channels	number of events	percentage
20	n,nn	23349	25.77%
19	p,pn	61121	67.45%
18	α,pp,αn	3983	4.40%
17	αp,ppp	1129	1.25%
16	$\alpha\alpha$	1030	1.14%

or three charged particles are strongly reduced and in the TOF_1-ΔE Z = 20, Z = 19 and Z = 18 events are observed as can be seen in Fig. 7.3 (right).

7.2 Cross section and coincidences PISOLO-silicon detectors

7.2.1 Cross section calculation

Obtaining the fusion cross section at the three energies measured follows the same procedure utilized for the ^{26}Mg + ^{12}C system described in chapter 5, so it will be only briefly repeated here in order to focus on the coincidences spectra between PISOLO and the silicon detectors. The ER have been identified using the TOF$_1$-ΔE spectrum with a condition on the TOF$_1$-E spectrum, and the spectra from the four monitors have been integrated. The differential fusion cross section has been obtained by the following formula:

$$\frac{d\sigma_f}{d\Omega}(E,\theta) = \frac{d\sigma_{Ruth}}{d\Omega}(E,\theta_{lab})\frac{N_{ER}}{N_{mon}}\frac{\Delta\Omega_{mon}}{\Delta\Omega_{ER}}\frac{1}{\epsilon} \tag{7.1}$$

where N$_{mon}$ is the number of elastic scattering events detected by the monitors, $\Delta\Omega_{mon}$ is the total solid angle subtended by them and θ_{lab} is the monitor angle (16°). N$_{ER}$ is the number of ER obtained from the PISOLO spectra, $\Delta\Omega_{ER}$ is the solid angle covered by the silicon detector at the end of the telescope and ϵ is the efficiency of the set-up. For this test, the ER angular distribution calculated by the Monte Carlo code PACE4 [42] has been used, and the result is shown in Fig. 7.4. The angular

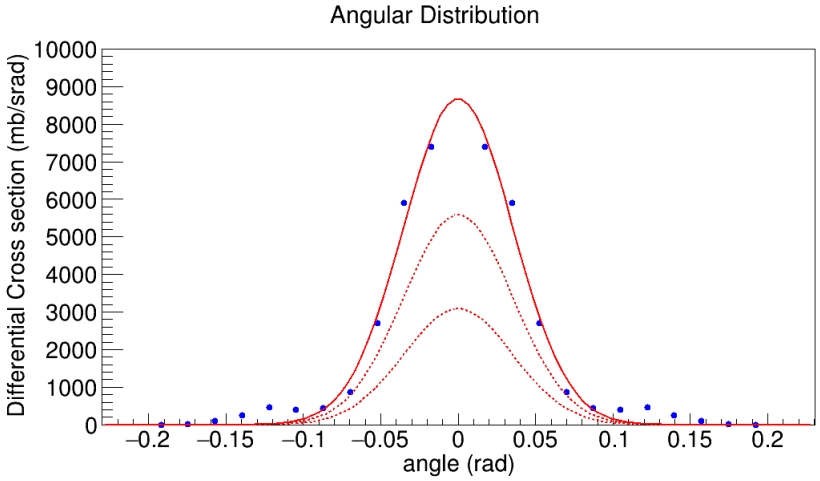

Figure 7.4. Angular distribution obtained with the PACE4 code for the system ^{30}Si + ^{12}C fitted with two Gaussian curves.

distribution obtained by PACE4 has been renormalized to the experimental points and integrated on the whole solid angle in order to extract the total fusion cross section. The results are reported in Table 7.2 and shown in Fig. 7.5 together with the

values obtained from a previous experiment with PISOLO for the same system [43].

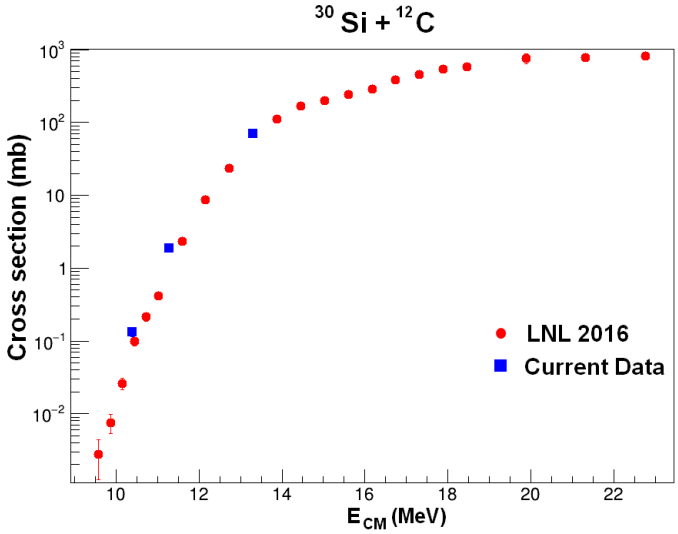

Figure 7.5. Fusion cross sections obtained in a previous experiment with only PISOLO [43] (red dots) and results from the current test (blue dots) for the system ^{30}Si + ^{12}C.

Table 7.2. Cross sections measured in this experiment with only PISOLO compared with the results of a previous experiment for ^{30}Si + ^{12}C. The quoted errors are statistical uncertainties.

$E_{CM}(MeV)$	σ_f (mb) present data	σ_f (mb) LNL 2016
13.3	75.3 ± 7.4	70.0 ± 7.2
11.3	1.91 ± 0.21	1.00 ± 0.16
10.4	0.147 ± 0.020	0.099 ± 0.014

The results are compatible with the previous data considering the ∼8% of systematic error of PISOLO and also that the angular distribution has been simulated with PACE4 and not measured.

7.2.2 PISOLO-EUCLIDES coincidences

The light charged particles detected by the two double-stage silicon detectors placed inside the reaction chamber have been put in coincidence with the ER detected by PISOLO. In this way, one can remove a large part of the background that makes it difficult to evaluate the number of ER only from the spectra of PISOLO, at the cost of a lower efficiency of the set-up. First, a gate on the E-ΔE spectra has been used to

select the events recognized as protons or α-particles detected by the two EUCLIDES detectors and then the spectra of PISOLO in coincidence with the selected events have been analyzed. Examples of the resulting spectra are shown in Fig. 7.6, and comparing these new spectra with those obtained only with PISOLO the background reduction is evident, especially for the lower energy. Another approach consists of

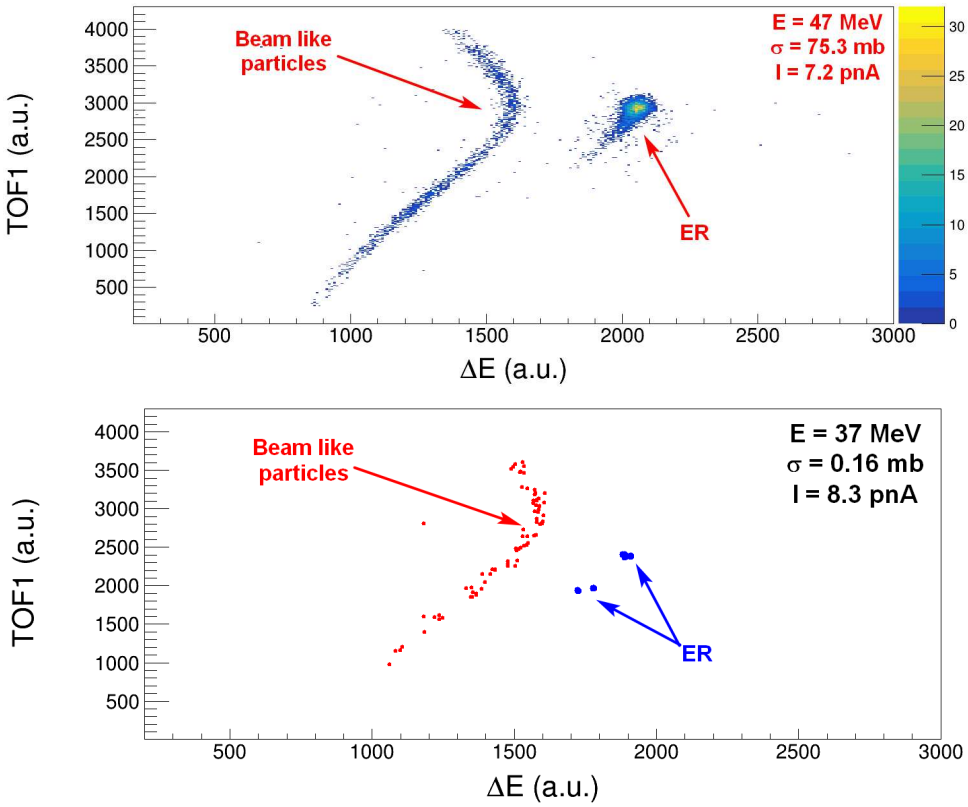

Figure 7.6. Example of $TOF_1 - \Delta E$ spectrum in coincidence with the charged particles identified in the E-ΔE spectrum of the EUCLIDES detectors, at the energy of 47 MeV (top panel) and 37 MeV (bottom panel) where the background reduction can be clearly observed.

using the time signal from the EUCLIDES detector placed at 120° as the start signal for a TAC module while the stop signal has been provided by the silicon at the end of the PISOLO telescope. In this way selecting the events of PISOLO in time coincidence with the EUCLIDES detector has been possible by a gate on the TAC spectrum as shown in Fig. 7.7. This method allows the use of a shorter time gate to exclude more efficiently the events far away from the coincidences peak providing an even better background suppression. In the test, only the detector placed at 120° has been used for this method, because it counted a much larger number of light particles. As shown in Fig. 7.8 with this time condition the number of beam-like

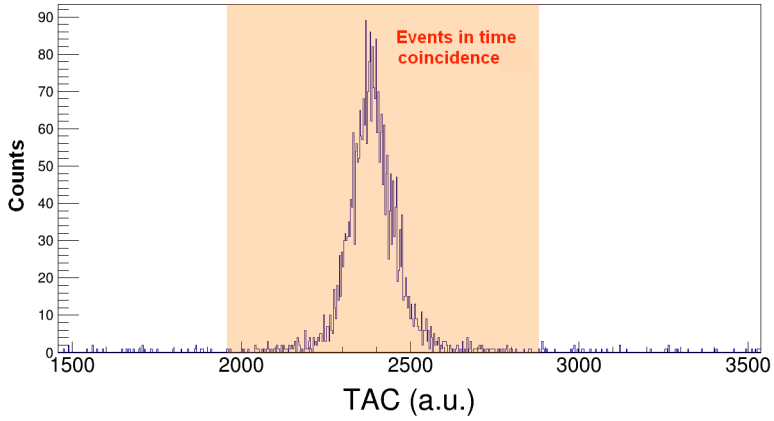

Figure 7.7. TAC spectrum at the energy of 47 MeV where the chosen time chosen is highlighted.

events is strongly reduced, while, the number of ER remains almost the same. From the coincidence spectrum at 47 MeV one can notice that the ER are for the most part in the region corresponding to Z = 19. The reason is that if the compound nucleus evaporates only one proton and PISOLO, which is placed at 3° with respect to the beam direction, detects the corresponding ER, then the proton is evaporated in the reaction plane defined by the beam and the ER direction. This is valid only for a two-body reaction, while if the compound nucleus evaporates more than one particle the angles are no longer fixed by the two-body kinematic. The efficiency for detecting these evaporation channels is lower since the particles can be evaporated out of the reaction plane. For this reason, the two silicon detectors have been placed in the reaction plane. The number of ER detected with this method with respect to the overall number of ER detected with PISOLO is reported in table 7.3, resulting in an efficiency of about 3.5-4% for the events taken in coincidence. This has been obtained with only two silicon detectors; in a future experiment, more silicon detectors will be installed in the reaction chamber increasing the overall efficiency of the set-up. The

Table 7.3. Number of ER detected in coincidence and with only PISOLO.

E_{CM} (MeV)	$N_{ER,PISOLO}$	$N_{ER,coinc}$	$\frac{N_{ER,coinc}}{N_{ER,PISOLO}}$(%)
13.3	360043	12796	3.55% ± 0.03%
11.3	1551	68	4.38% ± 0.54%
10.4	402	13	3.23% ± 0.91%

percentage of ER detected in coincidence slightly changes with the energy, probably because at lower energies the one-particle evaporation channels should be dominant.

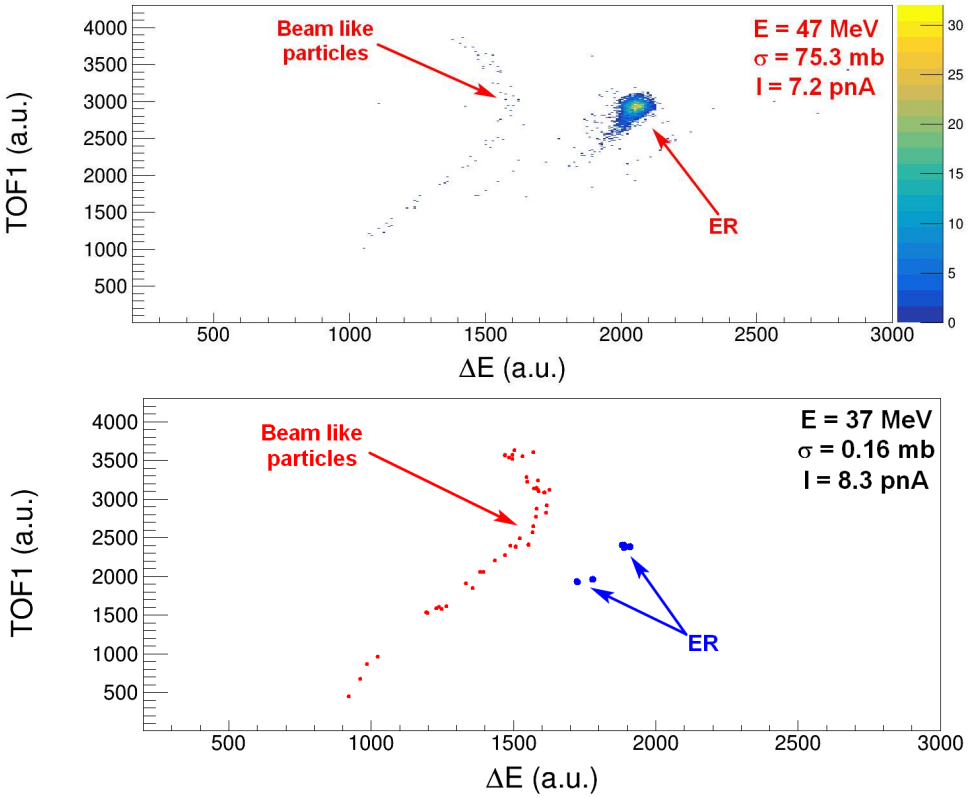

Figure 7.8. TOF_1-ΔE spectra at the energy of 47 MeV (top) and 37 MeV (bottom) in coincidence with EUCLIDES using the time gate on the TAC spectrum.

At the lowest measured energy (about 2.6 MeV below the Coulomb barrier), 13 events in coincidence have been detected in 11 hours of beam time.

7.3 Improvements for the PISOLO and silicon detectors set-up

The principal limitation of this method is the low efficiency of the set-up. This can be improved by utilizing more detectors on the reaction plane to detect most of the particles from channels where only one particle is evaporated (in general, these are the dominant evaporation channels at very low energies). In order to be able to mount silicon detectors also at forward angles, to increase the efficiency of the set-up, one should protect these detectors from elastic scattering with an aluminium foil placed in front of them. The background reduction obtained from the coincidences with the silicon detectors is particularly good so that it will be possible to place PISOLO at smaller angles where for PISOLO the background would be too high to consent a good discrimination between the ER and beam-like particles. Placing PISOLO at 2°, 1° or even at 0° will result in higher efficiency of the set-up while the background would be almost completely removed by the coincidences with the silicon detectors. A complete experiment employing the coincidence between the ER and evaporated particles will be proposed. The purpose of the experiment will be to measure the excitation function of ^{24}Mg + ^{13}C down to 100-200 *nb*. The study of this system will be also useful to understand better the reasons behind the oscillations in the logarithmic slope observed for the two systems ^{24}Mg + ^{12}C and ^{26}Mg + ^{12}C. Those oscillations do not have a theoretical explanation yet, but the behaviour of ^{24}Mg + ^{13}C would suggest that the smaller level densities of the CN (Fig. 7.9) could be the origin of the oscillation similarly to what happens in the two systems ^{12}C + ^{12}C and ^{12}C + ^{13}C [41] as described in Sect. 6.2. Fig. 7.9 shows the level density of the three compound nuclei ^{36,37,38}Ar in the relevant energy range, obtained using the parametrization of Refs. [44, 45] where the resulting curves are shown to be in agreement with available experimental data. We observe from the figure that the level density of the compound nucleus ^{37}Ar produced by ^{13}C + ^{24}Mg, is much larger with respect to the other two even-even systems. From this, we might expect no oscillations, in analogy to the case of ^{12}C + ^{13}C. In the case that oscillations in ^{13}C + ^{24}Mg will be observed, a different interpretation should be looked for.

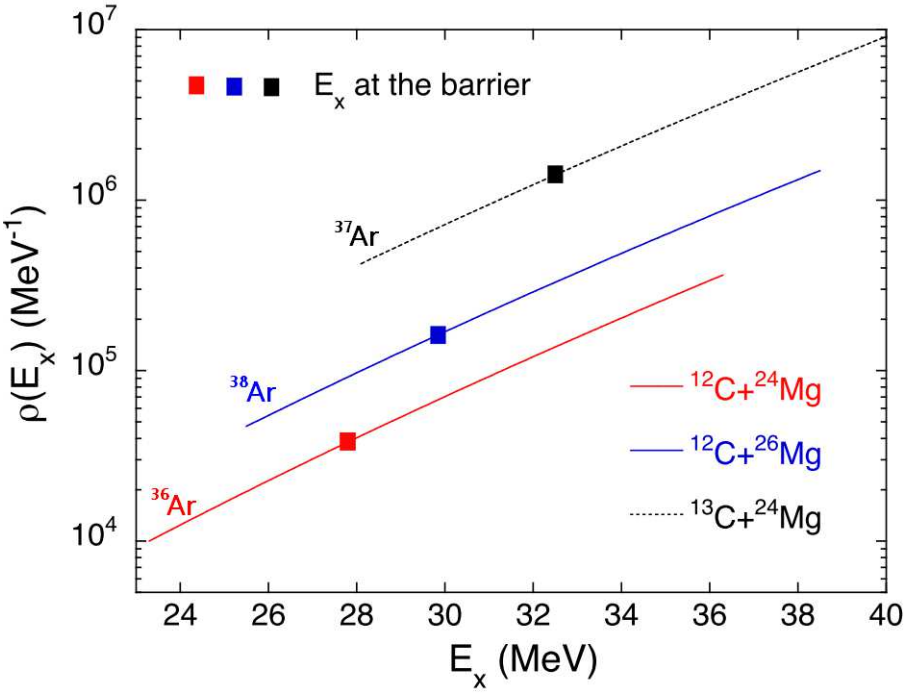

Figure 7.9. Level density for the three nuclei ^{36}Ar (red), ^{37}Ar (black) and ^{38}Ar (blue) as a function of the excitation energy of the compound nucleus.

Chapter 8

AGATA-EUCLIDES experiment

This test experiment has employed the coincidences between light charged particles evaporated by the compound nucleus and the prompt γ-rays emitted after the evaporation process.

EUCLIDES has been placed inside the reaction chamber of AGATA as shown in Chapter 4. The beam of ^{30}Si was provided by the XTU Tandem accelerator at the energies of 47 MeV and 40 MeV on a target of natural ^{12}C of thickness 100 μg/cm^2 placed in the centre of EUCLIDES. The target introduced an average beam energy loss of around 0.88 MeV and 0.91 MeV for the two energies measured, which was taken into account in the analysis. AGATA was placed at the close-up position (18 cm from the centre of the reaction chamber). The EUCLIDES detectors provide the energy loss ΔE of the particles in the first thin layer and the residual energy E in the second thicker layer stopping the particle. Combining the information from the two layers it is possible to distinguish between the various particles, as shown in Fig. 8.1. The protons and the α-particles with energy respectively below $\sim$3.4 MeV and $\sim$13.6 MeV are stopped in the first layer of the EUCLIDES detectors and do not reach the second one and, as a consequence, the energy lost in the second layer is zero. In the spectra, the events corresponding to these low-energy particles can be seen in the diagonal ΔE-E=ΔE. For the detectors at forward angles it can also be noticed that the protons with energy above $\sim$11.3 MeV are not stopped inside the E layer (punch trough). These events can be distinguished anyway from alpha and deuterium and have been taken into account during the analysis. The spectra from detectors at different angles from the beam direction show that the α particles evaporated beyond 90° are stopped in the ΔE layer so during the analysis also the particles stopped in the first layer of the detectors have been taken into account even if it is not possible to completely distinguish between protons and α-particles at energies lower than $\sim$3.5 MeV. The spectra of EUCLIDES have been calibrated using the energy necessary for protons, α-particles and deuterium to go through the ΔE layer and the E layer using the LISE++ physical calculator [31] associating then

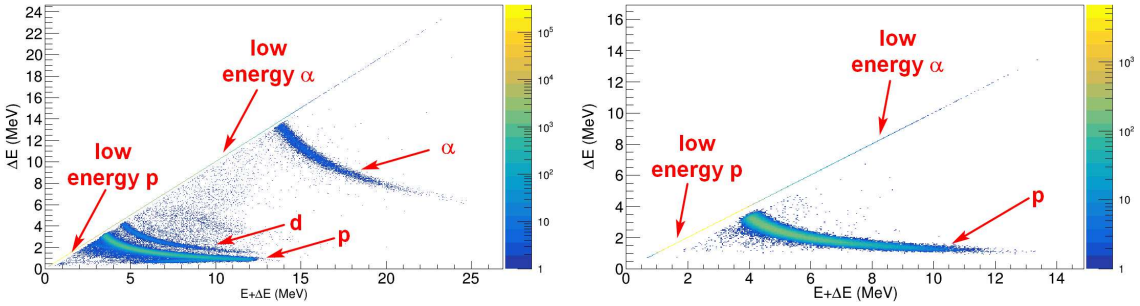

Figure 8.1. Spectrum ΔE vs (E+ΔE) of the detector H59 (left) placed at 60° and the detector P500 (right) placed at 120° from the beam direction.

these values to the corresponding points in the E-ΔE spectra. A gate has been placed on the E-ΔE spectra for every detector of EUCLIDES selecting the different particles. Only the events inside the gates have been put in coincidence with AGATA, in order to separate the various evaporation channels and reduce the background. The data of AGATA and EUCLIDES are then put together based on their timestamp difference and only the events within a certain time window are considered in coincidence. Since the signals from EUCLIDES come from 6 different boards with, in total, 88 channels, different detectors of EUCLIDES have different timestamps. As a consequence, the time gate for the coincidences is very large (1000 ns) including a lot of background. Therefore, the timestamp difference can be realigned to 0 adding a proper time offset to each detector. As a result of the realignment of the coincidence peak, as shown in Fig. 8.2, the width of the time gate can be decreased to 200 ns (from -10 to 10 TS in the figure), thus reducing the background.

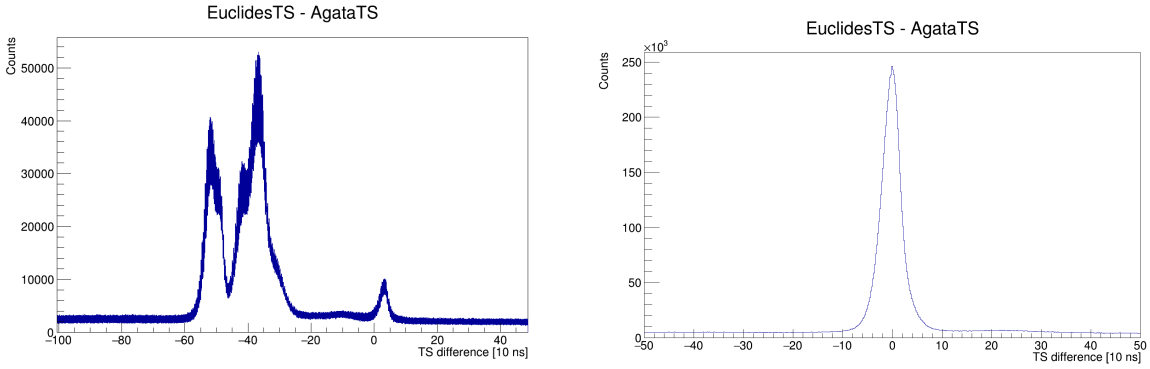

Figure 8.2. Timestamp difference before (left) and after (right) the alignment of the coincidences peaks.

8.1 Doppler Correction

Since the ER are moving at relativistic velocity ($\beta \approx 0.04$) the emitted γ-rays undergo a Doppler shift that modifies the energy of the γ according to the formula:

$$E = E_0 \frac{\sqrt{1-\beta^2}}{1-\beta\cos\theta} \tag{8.1}$$

where E_0 is the characteristic energy of the γ-ray emitted and θ is the angle between the velocity of the ER $\vec{\beta}$ and the γ-ray emitted. To correct this Doppler shift, the direction of the emitted γ deduced from its first interaction point in AGATA has been used. For the ER an average value of $\vec{\beta}$ can be used since the ER are produced at a very small angle around the beam direction. Fig. 8.3 reports the gamma singles spectra at 47 MeV with (red) and without (blue) the average Doppler correction. As can be seen, after the Doppler correction the two transitions at 770 keV and

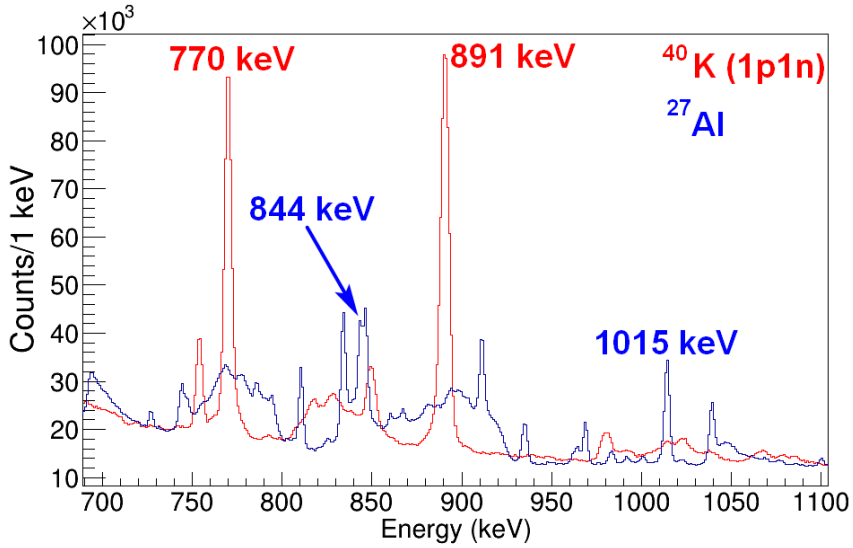

Figure 8.3. The AGATA spectrum at 47 MeV with (red) and without (blue) average Doppler correction.

891 keV from ^{41}K can be identified, while the two γ-peaks at 844 keV and 1015 keV produced by the excitation of the ^{27}Al of the target holder disappear. For the events in coincidence, is possible to obtain a better Doppler correction by reconstructing the ER kinematics using the information on the energy and the direction of the evaporated particles provided by the EUCLIDES detectors. In this way, it is possible to obtain a more precise event-by-event Doppler correction. This method is much more precise but can be used only for events in coincidence since the information from EUCLIDES is needed. Fig. 8.4 shows the difference between the two approaches for the spectrum

in coincidences with 1 α. One can notice that the peak corresponding to the $2^+ \rightarrow 0^+$ transition of the ^{38}Ar is much better defined with the event-by-event correction (red line) compared with the average correction (blue line).

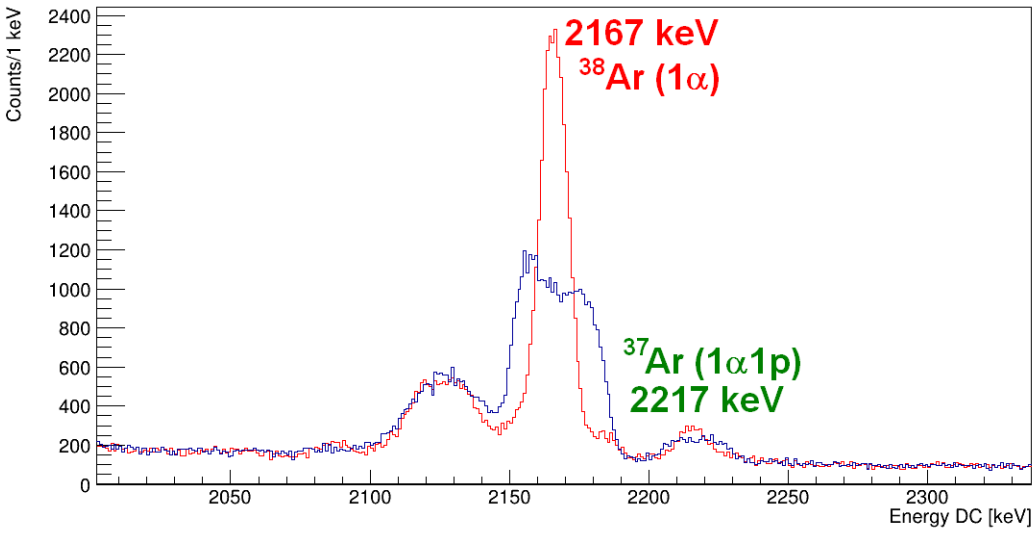

Figure 8.4. The AGATA spectrum at 47 MeV in coincidence with 1 α with an average Doppler correction (blue) and with an event-by-event Doppler correction (red).

8.2 EUCLIDES-EUCLIDES coincidences

Since the compound nucleus produced after the fusion process can evaporate more than one particle, a time coincidence between the different detectors of EUCLIDES is needed to identify these events correctly. The idea is to determine the shortest timestamp in the ΔE layer for the events inside a large time gate and then evaluate the difference between the shortest timestamp (TS_{min}) and the timestamp (TS) of every event in coincidence. The result is that the timestamp differences for the events actually in coincidence produce a coincidence peak around a value close to zero, because for the events with the shortest timestamp TS=TS_{min}. Instead, if there are other events in coincidence the time difference TS-TS_{min} will be of few tenths of nanoseconds producing a tail on the right of the peak. The events far from the peak are considered random coincidences and can be ignored to reduce the background. Through the analysis program (the selector [46]), a smaller time gate around the coincidence peak can be set. For this experiment, the width of the time gate has been set to 130 ns (from -5 to +8 TS). Fig. 8.5 shows the coincidence peaks for the detector H59 with the ΔE (left) and the E (right) layers of every other detector.

The coincidences between different EUCLIDES detectors are useful to reduce the

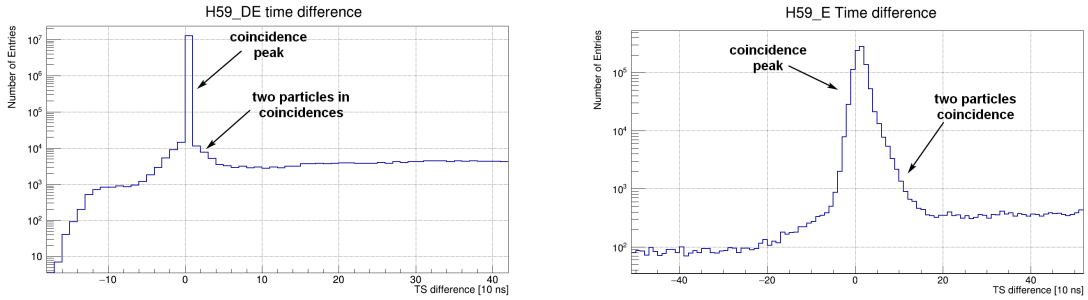

Figure 8.5. Time difference between the shortest timestamp for the ΔE layer (left) and E layer (right) of detector H59 with every other detector of EUCLIDES.

background of the spectra, and this is particularly important at energies far below the Coulomb barrier where the fusion events are infrequent.

8.3 Coincidence spectra

Once the time gate on EUCLIDES and on AGATA have been set the coincidence spectra between AGATA and EUCLIDES can be produced. For each detector of EUCLIDES protons, deuterons and alphas have been selected with a graphical cut on the E-ΔE spectra. In this way, through the analysis program Selector [46], it is possible to fill the spectra of AGATA only with the γ-events in coincidence with the selected events of EUCLIDES. It is also possible to require the coincidence with more than one EUCLIDES event to obtain the coincidence spectra for the evaporation channels 2 protons, 2 α and 1 proton + 1 α. For this reaction, ^{30}Si + ^{12}C, the compound nucleus is ^{42}Ca and the observed evaporation channels at the energy of 47 MeV are shown in Table 8.1. The coincidence with EUCLIDES allows to separate in different spectra the γ-transitions from the different evaporation channels and to strongly reduce the background produced by other reactions channels. Fig. 8.6 shows the difference between the γ-singles spectra and the spectra in coincidence with one α particle, showing how the transition at the energy of 2167.2 keV from ^{38}Ar cannot be easily identified without the coincidence with the charged particles detected by EUCLIDES. This is because of the background and the presence of γ-rays from other reaction channels. The spectra in coincidence with 1 proton and in coincidence with 1 α are shown respectively in Fig. 8.7 and 8.8, which refer to a run of about four hours of beam time performed with a mean current of 4.2 pnA at the energy of 47 MeV.

In these two spectra, one can recognize the main transitions for the different evaporation channels. The transitions highlighted are only the most intense, but there are several other peaks that have been identified during the data analysis.

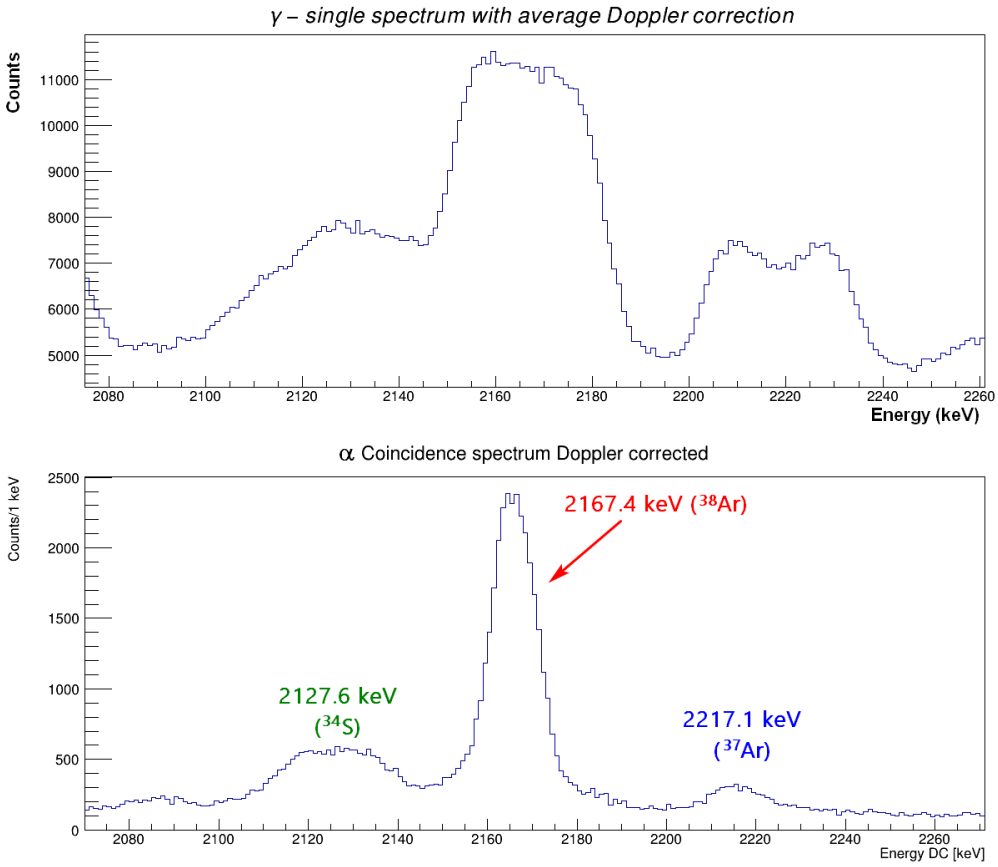

Figure 8.6. Comparison between the γ-singles energy spectrum (above) and the spectrum in coincidence with 1 α (below) for a run at 47 MeV. The peaks at 2167.4 keV, 2127.6 keV and 2217.1 keV cannot be identified without the coincidence with EUCLIDES.

Table 8.1. Evaporation channels and corresponding evaporation residues observed for the reaction ^{30}Si+^{12}C at 47 MeV.

evaporation channel	Evaporation Residue
1 proton	^{41}K
1 proton + 1 neutron	^{40}K
2 protons	^{40}Ar
1 proton + 1 alpha	^{37}Cl
1 neutron	^{41}Ca
2 neutrons	^{40}Ca
1 neutron + 1 alpha	^{37}Ar
1 alpha	^{38}Ar
2 alphas	^{34}S

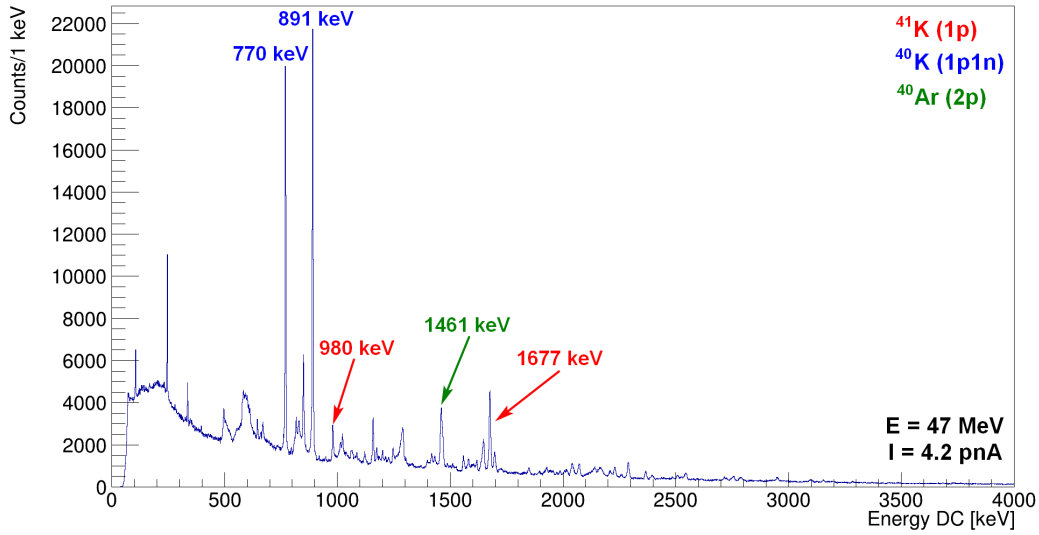

Figure 8.7. Spectrum of AGATA in coincidence with 1 proton where the main transitions for the 1 proton (red), 1 proton and 1 neutron (blue) and 2 protons (green) evaporation channels are highlighted.

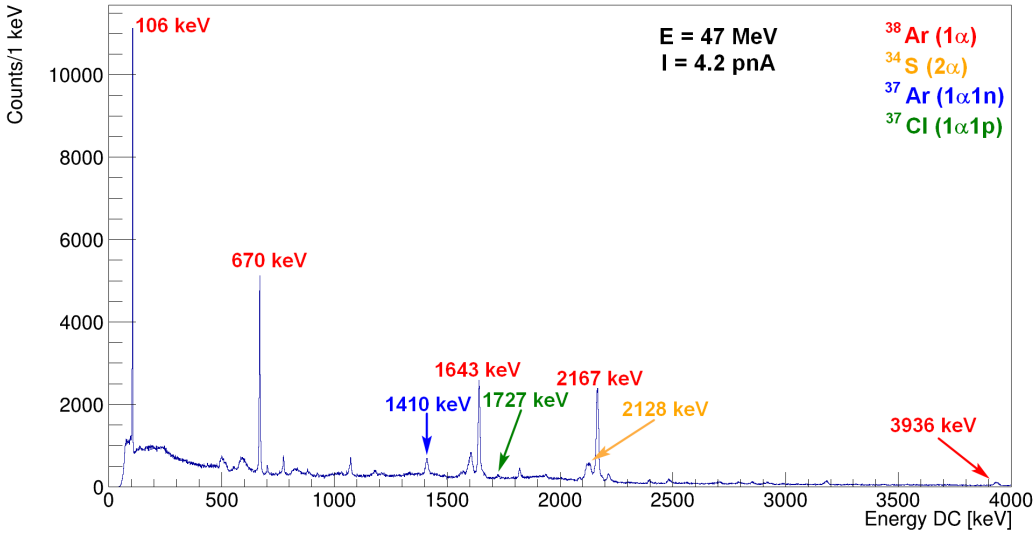

Figure 8.8. Spectrum of AGATA in coincidence with 1 α where the main transitions for the 1 α (red), 1 α and 1 neutron (blue), 1 α and 1 proton (green) and 2 α (orange) evaporation channels are highlighted.

Also, coincidences with more than one particle can be imposed, obtaining, in this way, the γ spectra of two protons, two α-particles and one proton + one α, shown in Fig. 8.9. In these spectra the most intense transitions from the corresponding evaporation channels, not simply recognizable from the spectra in coincidence with only one particle, can be observed; for example, the transition at 1460 keV from ^{37}Ar can be clearly identified in the 2 protons coincidence spectrum, the transition at 2128 keV from ^{34}S can be identified in the spectrum in coincidence with two α-particles and the transition at the energy of 1726 keV from ^{37}Cl can be observed in the spectrum in coincidence with one proton and one α. One can also notice that in the 1p1α coincidence spectrum, the most intense peak corresponds to the transition at 2128 keV from ^{34}S. The reason is that at very low energies both protons and α-particles stop in the ΔE layer of the EUCLIDES telescopes and as a consequence, it is not possible to distinguish α-particles from the protons. Since the low energy α-particles are emitted mainly from the 2α evaporation channel, the result is that the very low energy α are wrongly identified as protons and as a consequence, the 1p1α coincidence spectrum shows also a part of the γ-rays in coincidence with 2α. This is the reason for the presence of so many events corresponding to the transition from ^{34}S in the 1p1α coincidence spectrum.
In order to obtain the fusion cross section the number of fusion events is needed, which can be obtained from the number of γ-rays corresponding to transitions that

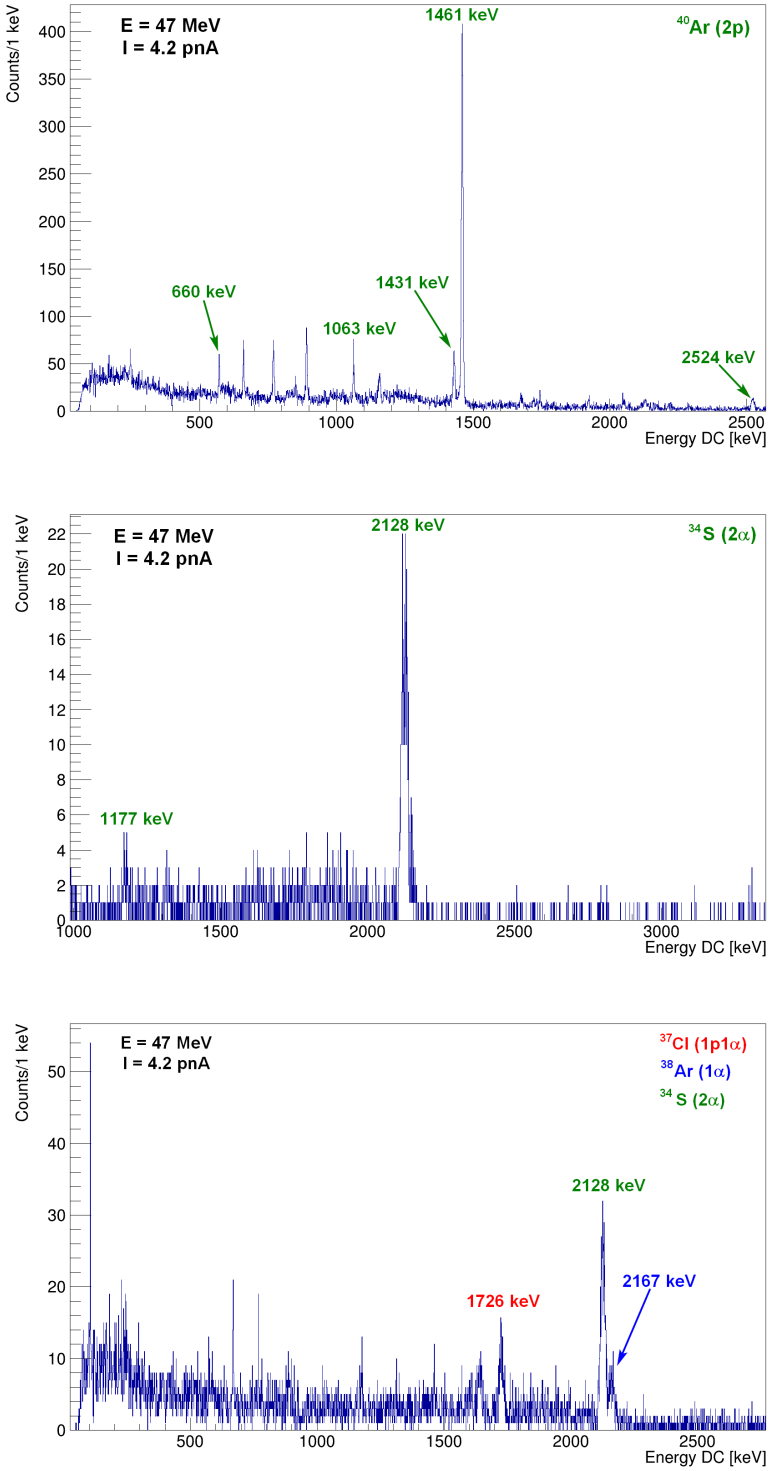

Figure 8.9. AGATA spectra in coincidences with 2 protons (top panel), 2 α-particles (centre panel) and 1 proton plus 1 α (bottom panel).

go directly to the ground state. For this reason, such transitions that have been identified in the coincidence spectra and the corresponding photo-peaks have been fitted with a gaussian plus a linear background and then integrated to obtain the number of γ-rays detected by AGATA for that particular transition. The full list of the transitions that go directly to the ground state identified in the spectra can be found in Table 11.3 in Sect. 11. At this point, the number of γ-rays obtained from this list of transitions has to be corrected for the efficiency of the set-up.

8.4 Efficiency of AGATA

The efficiency of AGATA has been measured in a previous experiment [47] utilizing three γ-sources of ^{152}Eu, ^{60}Co and ^{133}Ba placed at the centre of the reaction chamber. The absolute photo-peak efficiency for a given energy is defined as follows [48].

$$\epsilon_{photo} = \frac{number\ of\ counts\ in\ the\ photo-peak}{number\ of\ \gamma-rays\ emitted\ by\ the\ source} \tag{8.2}$$

One can use the formula:

$$\epsilon_{photo} = \frac{N_\gamma(E)}{A\Delta t I_R(E)(1-Dt)} \tag{8.3}$$

where $N_\gamma(E)$ is the number of counts in the photo-peak, extracted from the energy spectrum as the total area under the peak after background subtraction, A is the activity of the source, Δt is the duration of the measurement, $I_R(E)$ is the relative intensity of the transition with energy E and Dt is the dead time of the acquisition system. Using this method is possible to extract the efficiency from the γ single spectrum, however, it is also possible to estimate the efficiency using γ-γ coincidences. It consists of setting a gate on the upper γ of the cascade (E_1) and counting the number of events in the photo-peak of the lower γ of the cascade (E_2) in time coincidence with the γ-rays in the gate. The efficiency of the energy E_2 can be estimated from the following formula:

$$\epsilon_{photo}(E_2) = \frac{N_{\gamma,coinc}(E_2)}{N_{\gamma,single}(E_1)W(\theta)1/(1+\alpha_T(E_2))} \tag{8.4}$$

where $N_{\gamma,coinc}(E_2)$ is the number of counts in the $\gamma-\gamma$ coincidence spectrum for the E_2 transition, $N_{\gamma,single}(E_1)$ is the number of events in the γ-single spectrum, $W(\theta)$ is the angular correlation function of two consecutive γ-rays and α_T (E_2) is the internal conversion coefficient from the state at energy E_2. This technique allows us to get rid of dependencies on the dead time and the source activity but can be applied only to successive γ-rays. These two methods are schematically represented in Fig. 8.10. Using these two methods the absolute photo-peak efficiency has been measured for

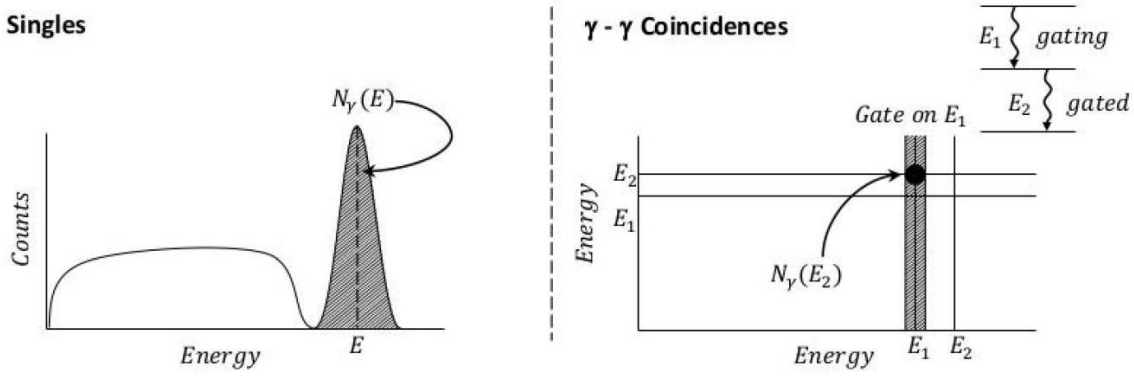

Figure 8.10. Scheme of the methods used to calculate the photo-peak efficiency of AGATA, in single (left) and in coincidence (right) (figure from [48]).

the different peaks of the γ-sources and then the values have been fitted with the RadWare function [49]:

$$\epsilon_{photo}(E_\gamma) = exp\left[\left[\left(A + Bx + Cx^2\right)^{-G} + \left(D + Ey + Fy^2\right)^{-G}\right]^{-1/G}\right] \tag{8.5}$$

$$with \quad x = ln\left(\frac{E_\gamma}{100}\right) \quad y = ln\left(\frac{E_\gamma}{1000}\right) \tag{8.6}$$

The value of C has been fixed to 0 while the value of G to 15 since similar values are usually set [50], the other parameters obtained from the fit are shown in table 8.2 The

Table 8.2. Parameters of the fitted efficiency curve [47].

A	B	D	E	F
5(4)	0.1(10)	1.268(9)	-0.42(2)	-0.063(10)

values of A and B have a very large error, anyway, these two parameters determine the behaviour of the efficiency curve at low energies far from the energies of interest for this experiment. This efficiency measurement was performed with AGATA placed at the nominal position (23.5 cm from the centre of the reaction chamber) while during the present experiment, AGATA was placed at the close-up position (18 cm from the centre of the reaction chamber), so the efficiency curve has been rescaled of a factor 1.28 obtained from the simulated efficiency curves for the two positions. The efficiency curve has been also estimated using only 23 crystals of AGATA so the curve has also been rescaled to the 32 crystals used in this experiment. The resulting curve is shown in Fig. 8.11 and the efficiency of AGATA estimated at the energy of 1.3 MeV for ^{60}Co is $\epsilon_{photo}(1.3\text{ MeV}) \sim 5.64\% \pm 0.16\%$

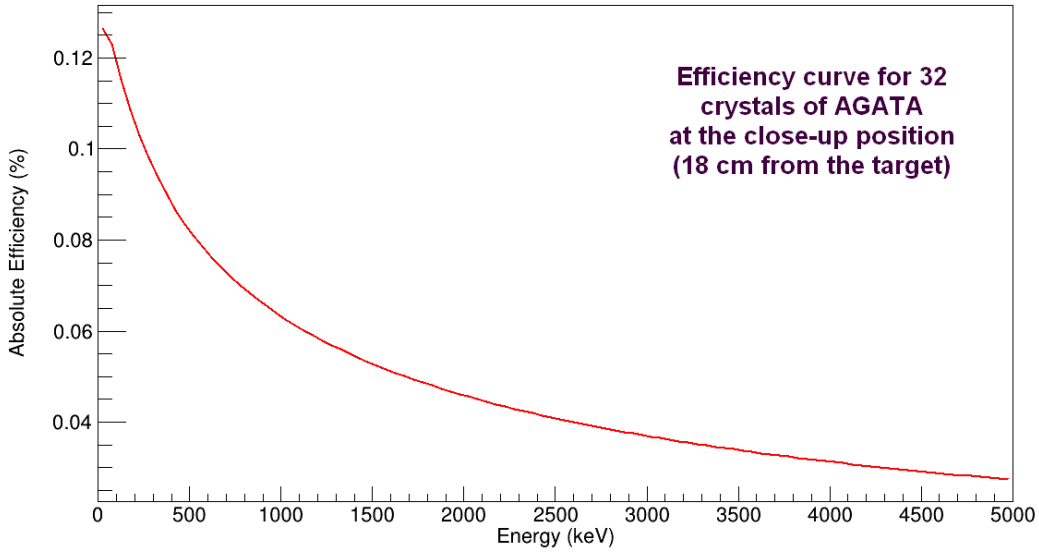

Figure 8.11. Efficiency curve of AGATA at the close-up position for 32 crystals.

8.5 Efficiency of EUCLIDES

The efficiency of EUCLIDES has been estimated by the ratio between the number of γ-rays emitted in coincidences ($N_{\gamma,coinc}$) with EUCLIDES and the number of γ-rays emitted in single ($N_{\gamma,single}$) for a given transition. Since the number of events in coincidence depends on both the efficiency of AGATA (ϵ_{agata}) and EUCLIDES ($\epsilon_{euclides}$) while the number of events in single depends only on the efficiency of AGATA, the ratio between these two quantities, gives us an estimate of the efficiency of EUCLIDES as shown in Eq. 8.7.

$$\frac{N_{\gamma,coinc}}{N_{\gamma,single}} = \frac{N_{\gamma}\epsilon_{agata}\epsilon_{euclides}}{N_{\gamma}\epsilon_{agata}} = \epsilon_{euclides} \tag{8.7}$$

The associated uncertainty can be calculated using the propagation of error formula:

$$\Delta\epsilon_{euclides} = \sqrt{\left(\frac{\Delta N_{\gamma,coinc}}{N_{\gamma,single}}\right)^2 + \left(\frac{\Delta N_{\gamma,single} \cdot N_{\gamma,coinc}}{N^2_{\gamma,single}}\right)^2} \tag{8.8}$$

The efficiency estimated using this method takes into consideration also the presence of the cylindrical aluminium absorber placed inside EUCLIDES and the Upilex-75S foil put in front of each detector of the array. The efficiency of EUCLIDES has been estimated for the different evaporation channels at different energies and the results are reported in Table 8.3 Only the most intense transitions can be identified in the

Table 8.3. Efficiency of EUCLIDES estimated for each evaporation channel. For the channels pp, $\alpha\alpha$ and pα the efficiency to detect only one of the two particles is reported.

ER	evap. channel	γ-ray energy (keV)	$\epsilon_{euclides}$ (47 MeV)	$\epsilon_{euclides}$ (40 MeV)
^{40}K	np	770	21.9% ± 0.4%	17.1% ± 0.5%
^{41}K	p	1677	25.3% ± 0.5%	20.3% ± 0.5%
^{40}Ar	pp	1460	37.8% ± 0.7%	32.4% ± 0.7%
^{38}Ar	α	2167	11.3% ± 0.5%	8.2% ± 0.5%
^{37}Ar	αn	1410	11.3% ± 0.5%	8.2% ± 0.5%
^{37}Cl	αp	1727	30.88% ± 0.5%	0%
^{34}S	$\alpha\alpha$	2157	20.4% ± 0.7%	0%

γ-singles spectra, so for the $\alpha\alpha$ or pp evaporation channel, the efficiency has been estimated from the value obtained for the channels p and α in two ways. The first one can be applied if the analysis of these channels is performed on the spectrum in coincidence with only one proton (or α), in this case, the efficiency is given by the following formula for the pp channel (and similarly for the $\alpha\alpha$ channel)

$$\epsilon_{pp} = 1 - (1 - \epsilon_p)^2 - \epsilon_p^2 \tag{8.9}$$

where ϵ_p is the efficiency of the channel p and ϵ_{pp} is the efficiency of detecting one of the two protons evaporated. In this way, the number of γ-rays from ^{40}Ar that are included in the spectrum in coincidence with only one proton have been corrected for the value ϵ_{pp}. The second method can be applied if the analysis is performed on the spectrum in coincidence with two protons (or two α particles). These spectra are cleaner compared with the spectra in coincidence with only one particle, but, the efficiency of EUCLIDES is smaller since the detection of two particles is required. The efficiency can be simply obtained from the following formula for the pp channel (and similarly for the $\alpha\alpha$ channel)

$$\epsilon_{pp} = \epsilon_p^2 \tag{8.10}$$

Similarly, the transitions of the evaporation channel αp can be studied in three different spectra (in coincidence with only one α, with only one proton or with one proton and one α) and, also in this case, the efficiency would be different depending on the particle we require to be in coincidence with the γ-rays from the ^{37}Cl. Since at energies below the Coulomb barrier, the probability of evaporating two particles decreases rapidly with the energy, already at the energy of 40 MeV the second method cannot be applied for the $\alpha\alpha$ evaporation channel since the peak of ^{34}S cannot be distinguished from the background (because of the low efficiency of detecting both evaporated α particles). For this reason, the efficiency has been estimated utilizing

the first method, analyzing the spectra in coincidence with only one particle for both the energies measured.

8.6 Geant4 simulation

To better prepare the experiment, have an estimation of the number of fusion events expected and predict the response of the set-up AGATA + EUCLIDES a simulation has been also used. The simulation is based on the Geant 4 toolkit [51] and can reproduce the behaviour of the AGATA spectrometer combined with the different ancillary detectors available at the LNL, including EUCLIDES, for various reactions. For the present case, the simulation has been set to reproduce a fusion evaporation reaction for the system ^{30}Si + ^{12}C with the set-up AGATA + EUCLIDES in the configuration used during the test including the cylindrical aluminum absorber placed inside EUCLIDES (as described in Sect. 4.1). The simulated set-up is shown in Fig. 8.12. The software has been used to simulate a large number of fusion evaporation events

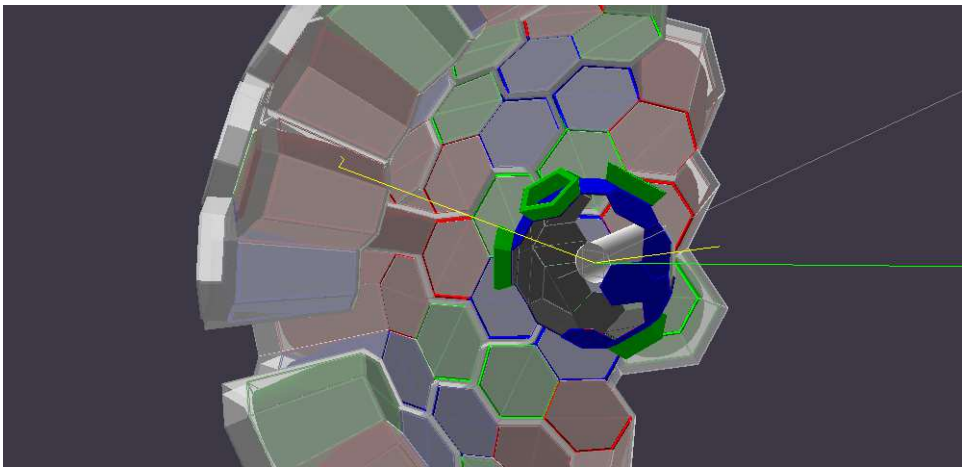

Figure 8.12. Picture of the simulated AGATA + EUCLIDES set-up with the simulation of one fusion event with the evaporation of one proton (green line) and the emission of two γ-ray (yellow lines).

for the different evaporation channels observed during the test to verify the response of the EUCLIDES + AGATA set-up at the two energies measured. In this way, it is possible to obtain an estimation of the efficiency of EUCLIDES. In Fig. 8.13 the E-ΔE spectra obtained from the simulation for all the detectors of EUCLIDES and the beam energy of 47 MeV can be observed for the evaporation of one proton or one α-particle. The simulation provides also the interacting position of the charged particles inside EUCLIDES that can be used to reconstruct the position of the detectors of EUCLIDES. In Fig. 8.14 is possible to notice that, as expected, the number of events

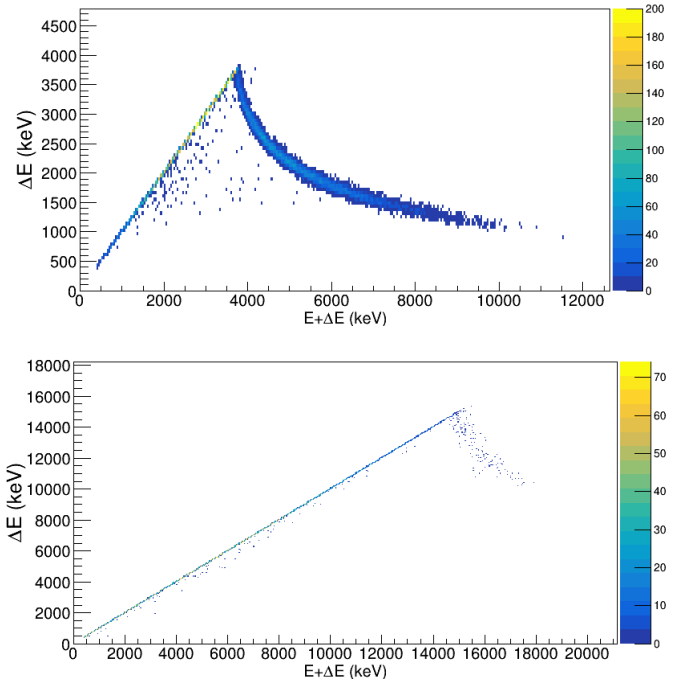

Figure 8.13. Simulated E-ΔE spectra for protons (left) and α-particles (right).

detected by the forward detectors is higher compared to the detectors at backward angles. It's also possible to estimate the efficiency of EUCLIDES as the ratio of the number of events detected by EUCLIDES and the total number of simulated events and confront the result with the efficiency obtained experimentally. The efficiency obtained in this way results to be ∼45% for proton and about ∼30% for alpha. The efficiency estimated using the simulation, results in being higher compared with what has been obtained in the previous section. To better understand the reason for this difference, the efficiency for only one EUCLIDES detector at the different θ angle has been simulated and the ratio between the events in a γ-peak in coincidences and in the same γ-peak without coincidences for the best performing detectors. The results are reported in Tab. 8.4. One can notice that the efficiency in the simulation is higher even for the best performing detectors used during the experiment. The simulation considers the EUCLIDES detectors perfectly working while in the experiment some of the detectors present lower performances, also the simulation does not take into account the threshold and the dead time of the acquisition. It's also possible to simulate the γ-events in AGATA obtaining a γ-spectrum similar to what has been obtained during the experiment. In Fig. 8.15 one can observe an energy spectrum obtained with AGATA where three different transitions (850 keV, 980 keV and 1677 keV) of ^{41}K (evaporation channel 1p) have been simulated and are visible in the spectrum.

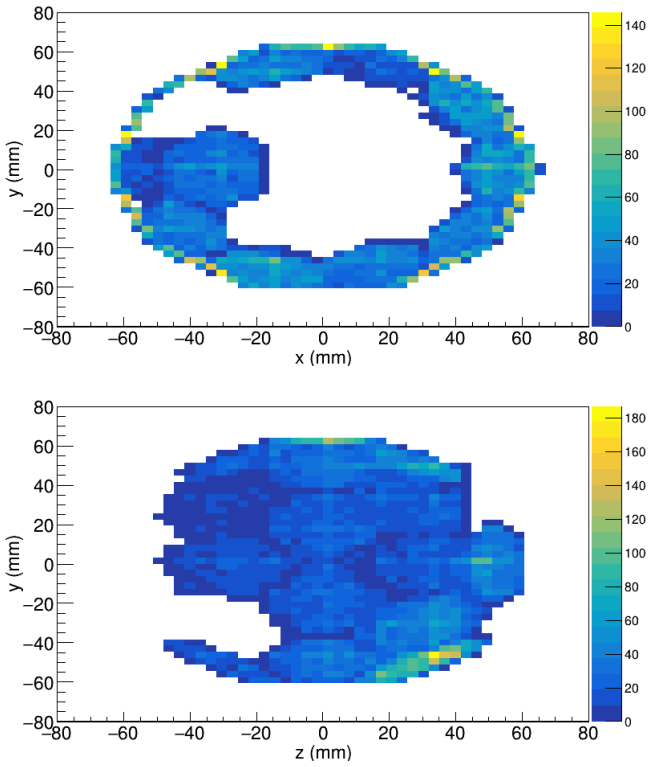

Figure 8.14. Front (top panel) and side (bottom panel) view of EUCLIDES in the configuration adopted for the experiment obtained from the interaction points provided by the simulation.

Table 8.4. Experimental and simulated efficiency of the single EUCLIDES detectors estimated for the different θ for the one proton evaporation channel.

θ angle	detector	$\epsilon_{euclides}$ simulation	$\epsilon_{euclides}$ experimental
30°	M0	3.75% ± 0.05%	3.08% ± 0.1%
60°	P200	2.82% ± 0.05%	2.39% ± 0.08%
90°	H39	1.79% ± 0.05%	1.38% ± 0.06%
120°	P500	1.23% ± 0.05%	1.18% ± 0.06%

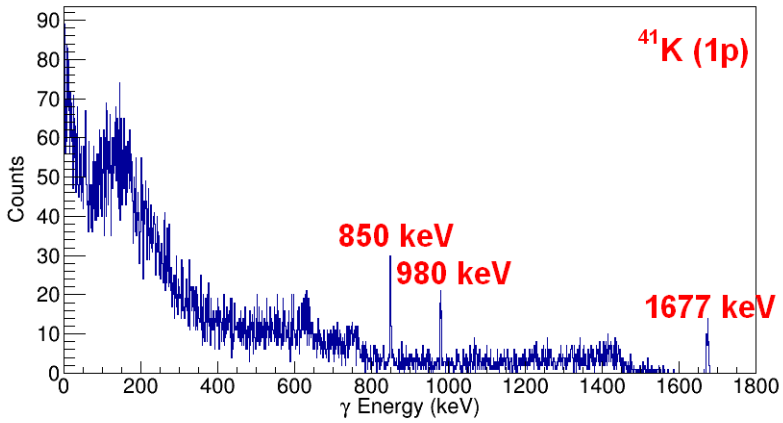

Figure 8.15. Simulated AGATA spectrum where the three transitions at 1677 keV, 980 keV and 850 keV of ^{41}K can be observed.

8.7 Cross section calculation

The fusion cross section can be determined from the coincidences between the light charged particles evaporated after the fusion process and the γ-rays emitted right after. In order to calculate the total fusion cross section the number of fusion events has been estimated from the number of γ-rays for transitions that go directly to the ground state properly corrected for the efficiency of AGATA and EUCLIDES; such various γ-peaks have been fitted with a Gaussian plus a linear background. This has been performed for the spectra in coincidence for the evaporation channels with at least one charged particle, while for the one neutron and two neutrons evaporation channels, where the corresponding γ-rays cannot be observed in the coincidence spectra, the number of events has been estimated directly from the γ-single spectra. An example is shown in Fig. 8.16 where the two peaks have been fitted together with two Gaussians plus a linear background. The total fusion cross section in mb can then be obtained from the fusion yields, calculated from the γ-rays in coincidence, knowing the thickness of the target and the intensity of the beam current using the following formula.

$$\sigma_f = \frac{A_t}{d_t I \Delta t \cdot 3.76 \cdot 10^3} \sum_{E_\gamma} \left(\frac{N_\gamma(E_\gamma)}{\epsilon_{AG}(E_\gamma)\epsilon_{EU}} \right) \tag{8.11}$$

Where $N_\gamma(E_\gamma)$ is the number of γ counts in the photo-peak at the energy of E_γ, $\epsilon_{AG}(E_\gamma)$ is the efficiency of AGATA at the energy E_γ, ϵ_{EU} the efficiency of EUCLIDES for the corresponding evaporation channel, A_t is the mass number of the target ($A_t = 12$), d_t is the target thickness in mg/cm^2 ($d_t = 0.1$ mg/cm^2), I is the intensity of the beam in pnA and Δt is the time duration of the run. The sum is extended over all γ-rays contributing to the fusion yield. The beam current has been

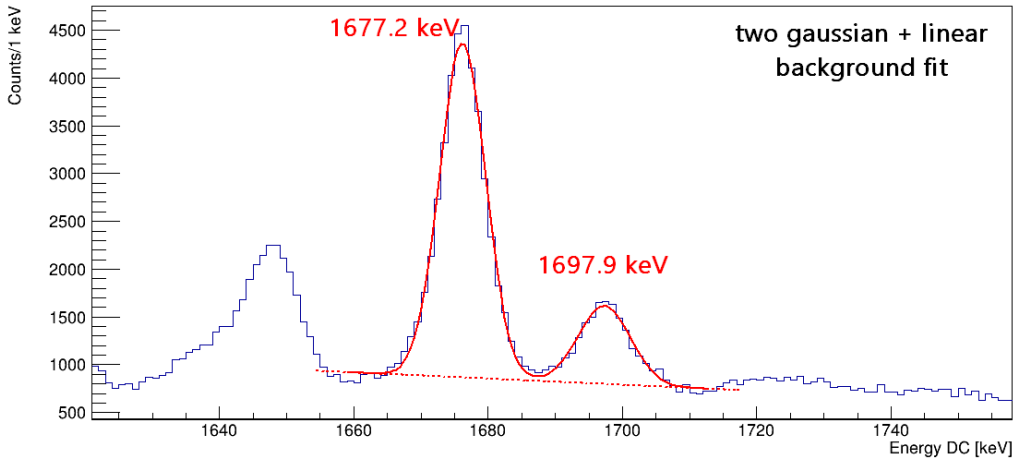

Figure 8.16. Fit of the peaks at 1677.2 keV and 1697.9 keV of ^{41}K at the energy of 47 MeV. The two peaks have been fitted with two Gaussian plus a linear background.

taken as the value measured at the beginning of each run and then the mean value of the current has been obtained based on the counting rate of AGATA during the run. Since the number of events in each γ-peak has been obtained as $N_\gamma = N_{tot} - B$, where N_{tot} is the total integral of the peak and B is the number of events in the linear background the statistical uncertainty on N_γ can be obtained as:

$$\Delta N_\gamma = \sqrt{\Delta {N_{tot}}^2 + \Delta B^2} \tag{8.12}$$

In addition to the statistical uncertainty on the cross section obtained with the Eq. 8.11 there is also a systematic error due to the uncertainty on the beam current of about 14%, estimated from the oscillations in the counting rate of AGATA, on the target thickness of 10% and the error on the AGATA and EUCLIDES efficiency of ∼5%. Anyway, since the beam current and the target thickness are only an estimate of the actual values, the result obtained with the formula 8.11 for the beam energy of 47 MeV has been renormalized to the cross section measured with PISOLO in a previous experiment [43]. The resulting normalization factor has been utilized to extract the fusion cross section at 40 MeV, the results are reported in Table 8.5, where one can notice that the cross section at 40 MeV is in good agreement with the one measured with PISOLO. For a future experiment of this kind, a more reliable estimate of the beam current can be obtained by using a Faraday cup to stop the beam.
Alternatively, one can normalise the fusion yield to the Rutherford cross section, measured by one or two monitor detectors placed at a forward angle with respect to the

beam direction. The integral of the peak relative to the elastic scattering of the beam on the target in the monitor spectrum can be used to normalize the fusion yield as it was done for the measurement with PISOLO described in Sect. 5.2. The total fusion cross section can be obtained from the following formula:

$$\sigma_f = \sum_{E_\gamma} \left(\frac{N_\gamma(E_\gamma)}{\epsilon_{AG}(E_\gamma)\epsilon_{EU}} \right) \frac{\Delta\Omega_{mon}}{N_{mon}} \frac{d\sigma_{Ruth}}{d\Omega}(E, \theta_{mon}) \tag{8.13}$$

where $N_\gamma(E_\gamma)$ is the number of counts in the photo-peak at the energy of E_γ, $\epsilon_{AG}(E_\gamma)$ is the efficiency of AGATA at the energy E_γ, ϵ_{EU} the efficiency of EUCLIDES for the corresponding evaporation channel, $\Delta\Omega_{mon}$ is the solid angle covered by the monitor, N_{mon} is the number of elastic scattering events measured with the monitor and $d\sigma_{Ruth}/d\Omega(E, \theta_{mon})$ is the Rutherford cross section at the angle where the monitor is placed at the energy of the beam. In this way, there is no need to know the current intensity and the target thickness precisely and one obtains a more accurate estimate of the fusion cross section. The results obtained with the Eq. 8.11 are also shown in Fig. 8.17 (blue triangles), where they are also compared with the cross sections obtained with only PISOLO in 2016 (red dots) and in the PISOLO plus silicon detector test (magenta squares). In the table, only the statistical errors are reported. The

Table 8.5. Cross section measured with the AGATA+EUCLIDES set-up confronted with the cross section measured with PISOLO [43], only the statistical errors are reported in the table.

Energy CM	σ_f AGATA+EUCLIDES	σ_f PISOLO
13.18 MeV	49.6 mb ± 0.2 mb	50 mb ± 5 mb
11.17 MeV	0.90 mb ± 0.02 mb	0.84 mb ± 0.10 mb

γ-charged particles coincidence method also allows us to estimate the fusion cross section for each evaporation channel and calculate the weight of every channel on the total fusion cross section. Table 8.6 reports the contributions of the different evaporation channels to the total fusion cross section. As can be seen, the channels ppp, αp and $\alpha\alpha$ completely disappear at energies below the Coulomb barrier and, in general, almost all the channels where more than one particle is evaporated are strongly suppressed at the lower energy.

These results can be compared with the cross sections obtained with PISOLO during the test with the two silicon detectors (Chapter 7) where the same system has been measured. In that case, one can distinguish between the various ER on the basis of the atomic number, therefore also for the AGATA-EUCLIDES test the number of events from the various channels with the same Z has been summed together. In Table 8.7 one sees the contribution of the evaporation channels with different atomic

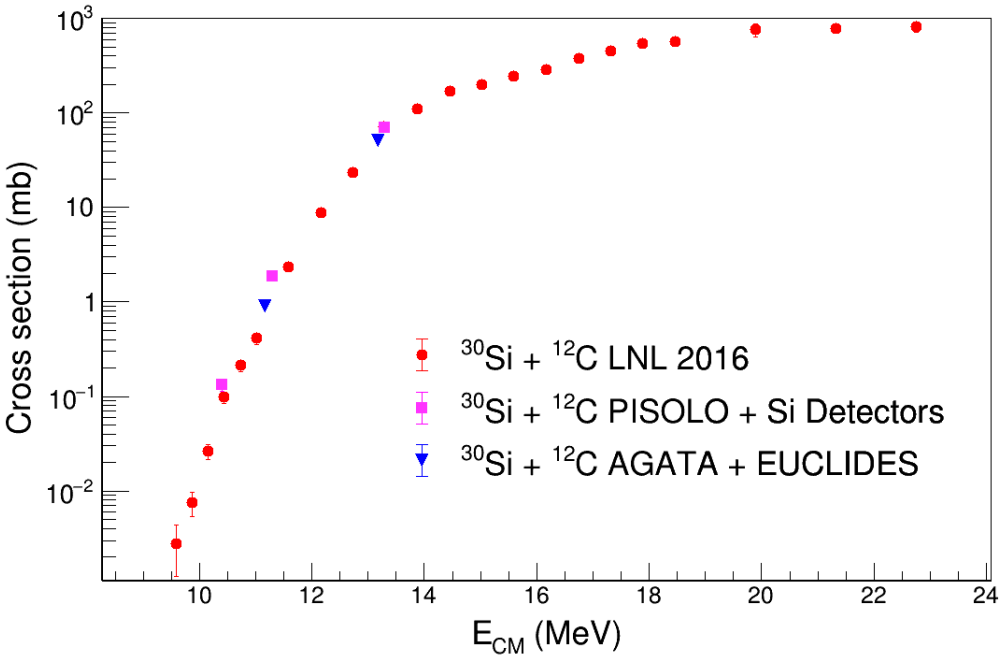

Figure 8.17. Cross section obtained with the AGATA+EUCLIDES set-up (blue triangles) compared with the results obtained with PISOLO in 2016 (red dots) and with PISOLO+Silicon detectors (magenta squares).

Table 8.6. Contribution to the total cross section of the different evaporation channels at the two measured energies.

nucleus	channel	contribution to σ_f at 47 MeV	contribution to σ_f at 40 MeV
^{40}K	np	41.71% ± 0.25%	14.90% ± 0.01%
^{41}K	p	12.9% ± 0.19%	30.71% ± 0.01%
^{41}Ca	n	7.89% ± 0.11%	12.74% ± 0.03%
^{40}Ca	nn	11.88% ± 0.06%	6.42% ± 0.01%
^{40}Ar	pp	1.82% ± 0.02%	3.386% ± 0.002%
^{38}Ar	α	14.23% ± 0.12%	30.44% ± 0.01%
^{37}Ar	αn	7.29% ± 0.06%	1.407% ± 0.001%
^{37}Cl	αp	0.103% ± 0.004%	0%
^{34}S	$\alpha\alpha$	2.09% ± 0.02%	0%
^{39}Cl	ppp	0.094% ± 0.003%	0%

Table 8.7. The contribution to the total cross section of the evaporation channels with different Z at the energy of 47 MeV measured with the AGATA+EUCLIDES set-up and with PISOLO.

Z	channels	contribution to σ_f AGATA	contribution to σ_f PISOLO
20	n, nn	19.77% ± 0.13%	25.77% ± 0.17%
19	p, pn	54.60% ± 0.33%	67.45% ± 0.27%
18	α, pp, αn	23.34% ± 0.14%	4.40% ± 0.07%
17	αp, ppp	0.103% ± 0.004%	1.25% ± 0.04%
16	$\alpha\alpha$	2.10% ± 0.02%	1.14% ± 0.04%

numbers obtained in the two experiments at 47 MeV. The difference in the results can be attributed to the fact that PISOLO detects the ER only at a specific angle (3° in the test). Since the fraction of events detected by PISOLO depends on the angular distribution of the ER that depends on the mass of the particle evaporated, the fraction of ^{38}Ar from the α evaporation channel detected by PISOLO is lower than the result obtained with the AGATA-EUCLIDES set-up.

8.8 Background subtraction

Analyzing the coincidence spectra measured at the beam energy of 40 MeV one can notice that there is a quite intense peak at the energy of 136.3 keV that cannot be assigned to any ER (Fig. 8.18). Indeed, this peak belongs to ^{181}Ta, whose presence is due to the tantalum shield of EUCLIDES used to prevent the beam from hitting directly the detectors. Probably, during the experiment, a halo or part of the beam hit that shield producing the intense background that was observed in the spectra, due to the problematic beam focalization for this experiment.

In fact, since it is not possible to focus the beam on quartz while EUCLIDES is inside the reaction chamber, focusing was performed before EUCLIDES was installed at the beginning of the experiment, and during the energy change. For this reason, it is possible that the focalization of the beam worsened during the measurement resulting in a halo of the beam hitting the tantalum shield.

Correctly analysing these spectra is very important to reduce the background produced by the ^{181}Ta. This can be obtained by estimating the background of the coincidence spectra using a time gate on the timestamp difference between AGATA and EUCLIDES away from the coincidence peak. In this way, one can obtain the spectra of AGATA filled with events in random coincidence with EUCLIDES and use it as an estimate of the background to be subtracted from the coincidence spectra. For the analysis, two time-gates have been chosen, one from -750 ns to -150 ns and the other from 150 ns to 750 ns (the gate around the coincidence peak has been

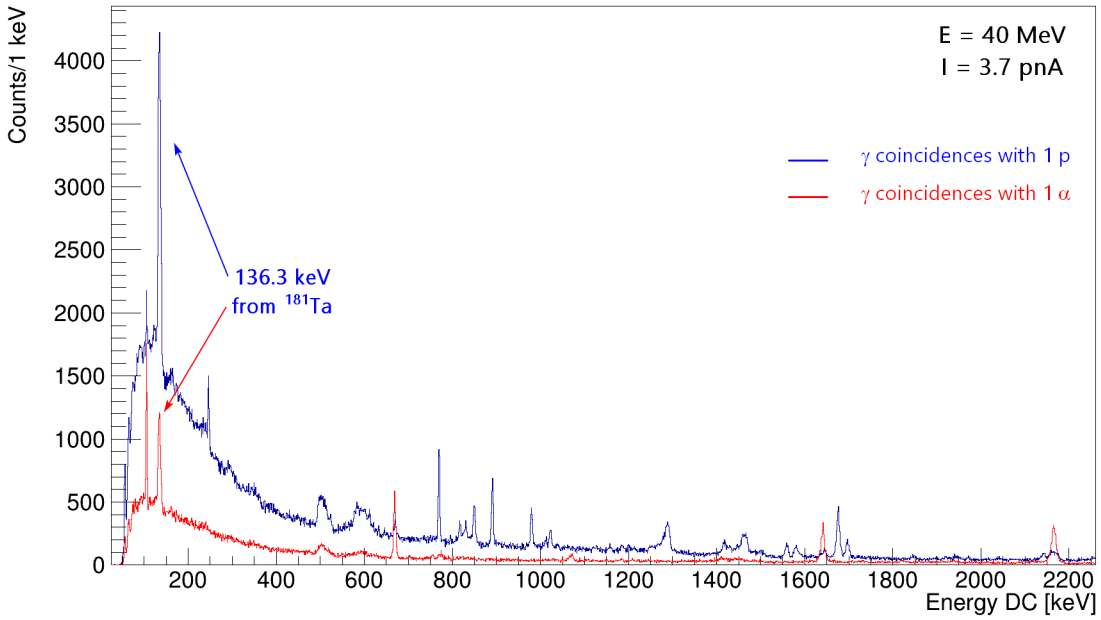

Figure 8.18. Example of a Doppler corrected energy spectrum measured at 40 MeV in coincidence with 1 proton (blue line) and 1 α (red line) where the peak at 136.3 keV from ^{181}Ta is clearly present.

taken from -100 ns to 100 ns) as shown in Fig. 8.19. Since the number of random coincidences is much smaller than the event in the coincidence peak, the time gate for the background has been taken six times larger, so that, the counts in the resulting spectra have been renormalized by a factor six. The results are shown in Fig. 8.20 where the coincidence spectra for a run at 40 MeV can be seen with and without the background subtraction. It can be noticed that the peak at 136.3 keV from ^{181}Ta disappears after this background subtraction.

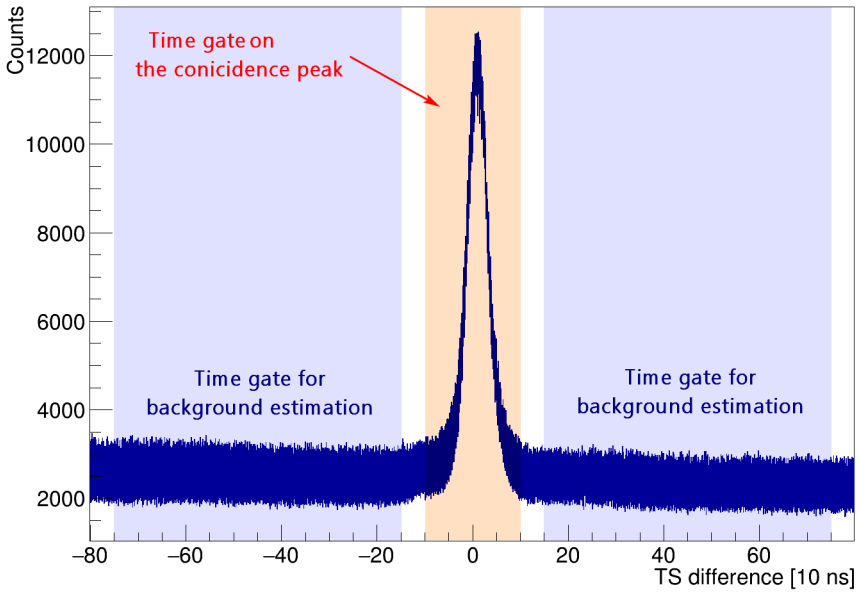

Figure 8.19. Coincidence peak for a run at 40 MeV showing the time gate on the coincidence peak and the time gates away from the peak used to estimate the background.

8.9 Excitation energy

The information from the evaporated particles detected by EUCLIDES also allows us to reconstruct the excitation energy of the evaporation residues for all events in coincidence. In the fusion process, the compound nucleus is produced at an excitation energy of $E_x = Q_{fus} + E_{cm}$ where Q_{fus} is the Q-value of the reaction (for ^{30}Si + ^{12}C, Q_{fus} = 14.1 MeV) and E_{cm} is the centre of mass beam energy (E_{cm} = 13.4 MeV and 11.4 MeV at the two measured energies). The excitation energy is partially removed by the evaporated particles and then by the γ-rays. It is possible to calculate the energy removed from the compound nucleus by the evaporated particles knowing their

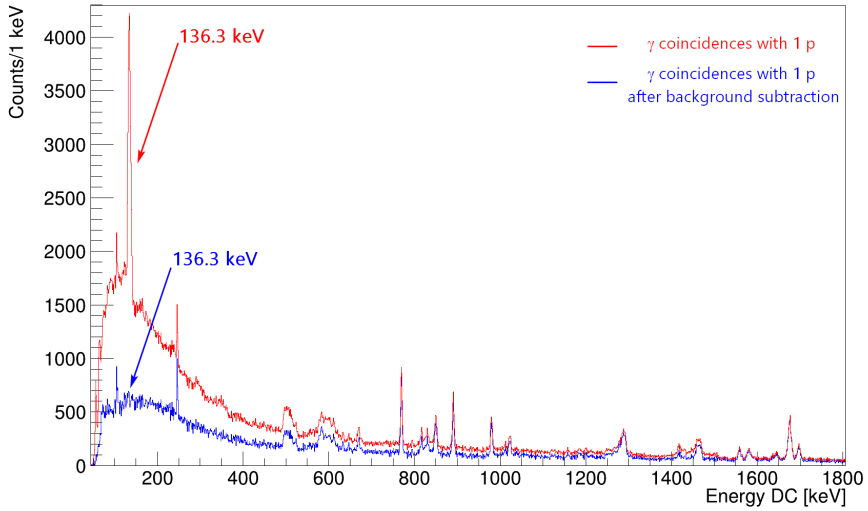

Figure 8.20. Example of a Doppler corrected energy spectrum measured at 40 MeV in coincidence with 1 proton with (blue line) and without (red line) the background subtraction, the peak at 136.3 keV from ^{181}Ta completely disappears after the background subtraction.

energy and direction provided by EUCLIDES and correcting it for the energy loss in the aluminum cylinder and the Upilex-75S foil in front of each detector of EUCLIDES, obtaining in this way the excitation energy of the ER. The matrices that combine the excitation energy extracted for every event with the γ-rays in coincidence with one proton and with one α are shown respectively in Fig. 8.21 and Fig. 8.22. It is also to be noticed that these two spectra are in coincidence with only one proton and with only one α respectively, so that, one of the particles evaporated in the channels np, αp, $\alpha\alpha$ and αn has not been detected by EUCLIDES. As a consequence, part of the information is missing, resulting in a value of the reconstructed excitation energy higher than the actual value for these channels.
The matrix in coincidence with one proton shows that there are two regions, lower and higher excitation energy; in the high energy region, most of the events are related to the 2 protons and 1 neutron + 1 proton evaporation channels, while in the low energy region, most of the γ-rays come from the evaporation channel of 1 proton. In fact, the most intense transitions from ^{40}K (np evaporation channel) like the one at 770 keV and the one at 891 keV disappear for excitation energies lower than about 11 MeV. On the other hand, the most intense transitions from ^{41}K (p evaporation channel) like 1677 keV and 980 keV appear clearly only when the excitation energy goes below about 13 MeV.
In the spectrum in coincidence with one α-particle the separation is not so evident but

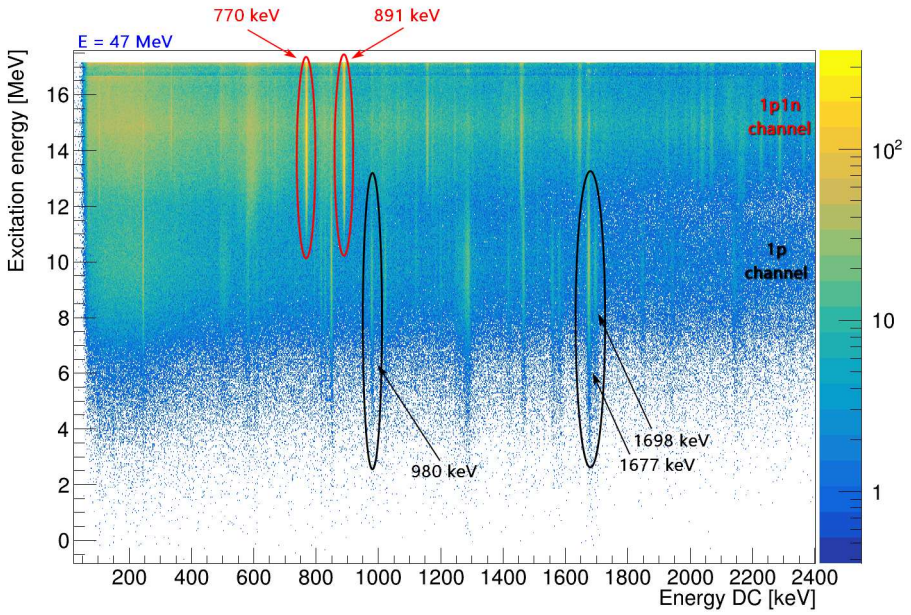

Figure 8.21. Matrix excitation energy - γ energy at 47 MeV in coincidence with 1 proton. The transitions at 770 keV and 891 keV from ^{40}K (np) are visible only at high excitation energy while the transitions at 1677 keV and 1698 keV from ^{41}K (p) show up only at low excitation energy.

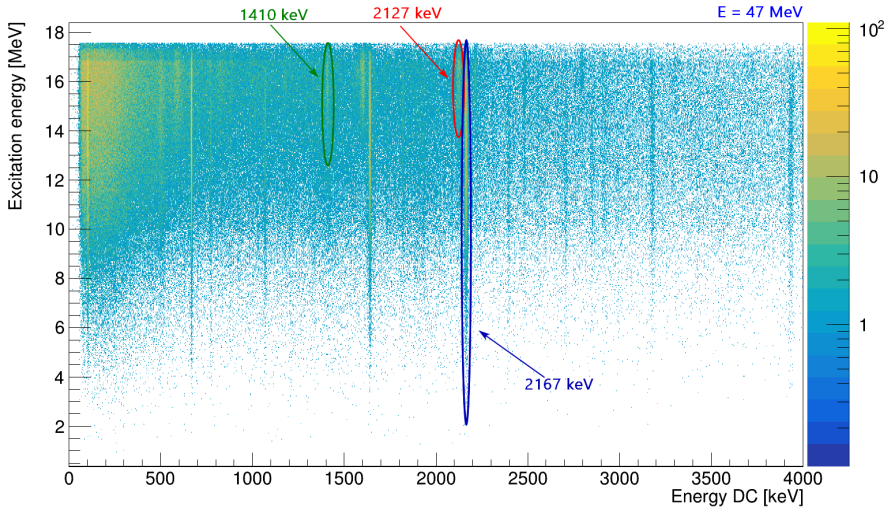

Figure 8.22. Matrix excitation energy - γ energy at 47 MeV in coincidence with 1 α. The transition at 2167 keV from ^{38}Ar (α) is visible for almost every excitation energy while the transitions at 2127 keV and 1410 keV from ^{34}S and ^{37}Ar respectively are visible only at high excitation energy.

the γ-rays belonging to the 2 α and 1 neutron + 1 α evaporation channels are visible only in the high excitation energy region of the spectrum. Indeed, the transition at 2167 keV of ^{38}Ar can be observed for almost any value of the excitation energy but the transitions at 2127 keV of ^{34}S (2α evaporation channel) and at 1410 keV of ^{37}Ar (αn evaporation channel) are not observed for excitation energies lower than about 13 MeV.
The reason may be the different energy of the particles emitted from different evaporation channels, in fact, the energy released by the particles in the detectors of EUCLIDES is larger for the protons evaporated in channel p compared with the protons in channel np. Similarly, the α-particles emitted in the 1 α evaporation channel result to be more energetic compared with the particles emitted in the $\alpha\alpha$ or αn evaporation channel. This difference in the energy of the particles evaporated in different channels can be observed in the coincidence spectra of AGATA with a gate on the energy left in the EUCLIDES detectors by the charged particles. As shown in Fig 8.23 the most energetic particles (12 MeV $< E <$ 17 MeV) are in coincidence with almost only transitions of ^{38}Ar (Fig. 8.23 top panel). At lower energies (5 MeV $< E <$ 10 MeV) most of the transitions come from ^{38}Ar and ^{41}K. Also the transitions at 2127 keV from ^{34}S and at 770 keV and 891 keV from ^{40}K now can be observed, even if the corresponding photo peaks are a small fraction of the total number obtained without conditions on the energy of the charged particle (Fig. 8.23 central panel). For the least energetic particles (0 MeV $< E <$ 5 MeV) the ^{40}K transitions become dominant while the peaks of ^{38}Ar and ^{34}S become much smaller, also the transition at 1460 keV of ^{40}Ar becomes visible, while ^{41}K is still present but is no longer the most intense transition (Fig. 8.23 bottom panel). Since most of the γ-rays of ^{40}K appear only when the gate is placed at low energies while most of the γ-rays of ^{41}K show up at higher energies, on average, the energy of protons of the 1p evaporation channel is higher than the energy of the protons of the pn or pp evaporation channel. Similarly, also the α emitted in the α evaporation channel are, on average, more energetic with respect to the particles emitted in the 2α or αn evaporation channels. As a consequence, the energy of the particles from 1p and 1α channels results to be larger with respect to that of the other evaporation channels. The separation of the different evaporation channels by the excitation energy of the ER is useful to distinguish between two γ-peaks very close in energy. An example is shown in Fig. 8.24 where the peak at 1460 keV of ^{40}Ar (pp) and the peak at 1468 keV of ^{41}K (p) are too close in energy to be correctly identified in the coincidence γ spectrum alone, but thanks to the separation in the excitation energy the two peaks can be identified and correctly integrated to calculate the fusion cross section.

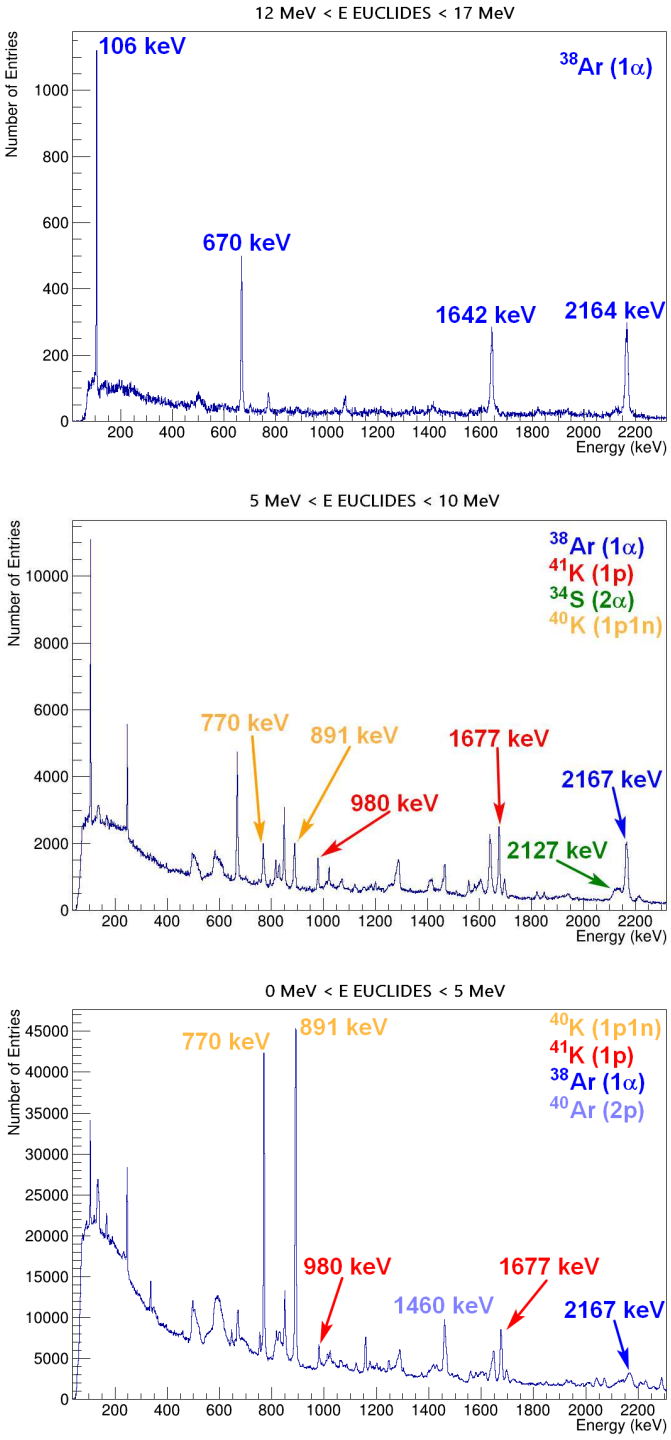

Figure 8.23. Doppler corrected γ-ray energy spectra from AGATA with a condition on three different intervals of the charged particle energy. The γ-rays from the np evaporation channel become dominant only in coincidence with low energy particles, while for more energetic particles the γ-rays from p and α evaporation channels are dominant.

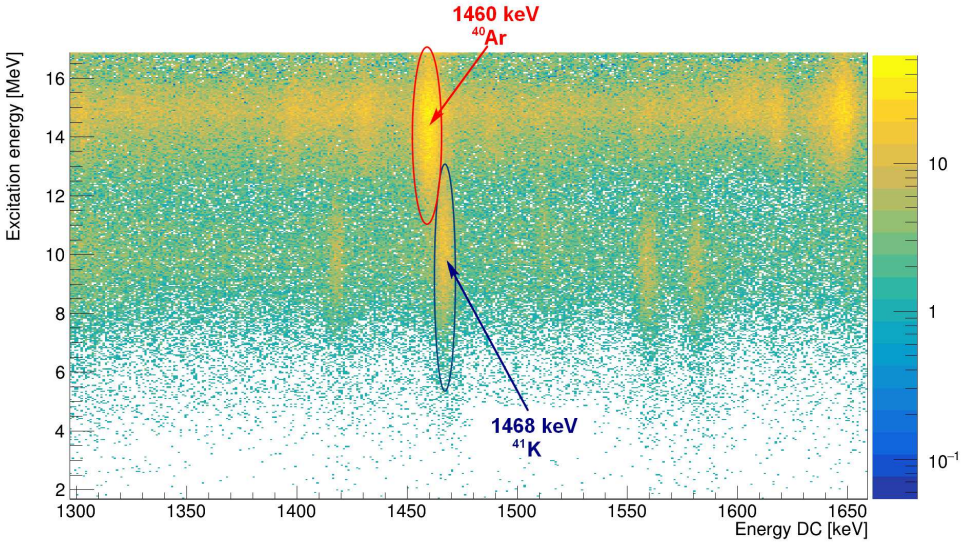

Figure 8.24. The peak at 1460 keV of ^{40}Ar (pp) that can be separated from the one at 1468 keV of ^{41}K (p) by means of the different excitation energy of the two ER.

8.10 Angular distribution of evaporated particles

The angle at which each charged particle is emitted with respect to the beam direction can be deduced from the position of the EUCLIDES detector that sees the particle. Even if the angular resolution is quite low (each detector of EUCLIDES covers an angle of about $\sim$30° in the θ coordinate) it is still possible to reconstruct the angular distribution. One can analyse the spectra of AGATA in coincidence with single detectors of EUCLIDES fitting and integrating the photo-peaks corresponding to the transitions that go directly to the ground state. In this way, it is possible to obtain the number of fusion events corresponding to a specific angle for each detector, and then sum the contribution of the detectors at the same θ angle with respect to the beam direction to obtain the angular distribution. The differential fusion cross section in mb/sr for the angle θ covered by EUCLIDES has been calculated using the following formula:

$$\frac{d\sigma_f}{d\Omega}(\theta) = \sum_{E_\gamma} \left(\frac{N_\gamma(E_\gamma)}{\epsilon_{AG}(E_\gamma)\epsilon_{i,EU}} \right) \frac{A_t}{d_t I \Delta t \Delta\Omega_{EU} \cdot 3.76 \cdot 10^3} \tag{8.14}$$

where $N_\gamma(E_\gamma)$ is the number of events in the photo peak of energy E_γ, ϵ_{AG} is the efficiency of AGATA for γ-rays of energy E_γ, $\epsilon_{i,EU}$ is the efficiency of the single detector of EUCLIDES for the proper evaporation channel, A_t is the mass number of the target ($A_t = 12$), d_t is the thickness of the target in mg/cm^2 ($d_t = 0.1$ mg/cm^2), I is the average beam current in pnA, Δt is the time length of the run analyzed in seconds

and $\Delta\Omega_{EU}$ is the solid angle covered by the EUCLIDES detectors placed at the angle θ. As already mentioned (Sect. 8.5) the absolute efficiency for the evaporation channel of one of the detectors of EUCLIDES can be estimated by the ratio between the number of events in a photo peak in coincidence with EUCLIDES and the number of events in the same photo peak for the γ-singles spectra. The intrinsic efficiency can be estimated by the ratio between the absolute efficiency with the percentage of particles that are emitted toward each detector of EUCLIDES. The percentage of particles evaporated toward each detector was determined using the code PACE4 to estimate the angular distribution of the charged particles for the system ^{30}Si + ^{12}C at the two measured energies. The angular distributions then were fitted with a Gaussian and the resulting curve was integrated on the solid angle covered by each EUCLIDES detector. The resulting values have been then divided by the integral of the angular distribution on the whole solid angle obtaining in this way the percentage of events evaporated toward each EUCLIDES detector used to obtain the intrinsic efficiency. At this point, it is possible to calculate the differential fusion cross section for each detector of EUCLIDES through the Eq. 8.14 by integrating the photo peaks that go directly to the ground state from the spectra of AGATA in coincidence with the singles detectors of EUCLIDES. The results obtained for detectors placed at the same θ angle with respect to the beam direction have been summed together. The results are reported in Table 8.8 and are shown in Fig. 8.25.

The angular distributions have been obtained for the three main evaporation channels: one proton, one proton plus one neutron and one α, the other evaporation channels do not have enough events in coincidence with the detectors placed at backward angles to extract the differential cross section at 90° and 120°. The angular distribution of each channel has been then fitted with a Gaussian curve and integrated on the whole solid angle to obtain the contribution of that evaporation channel to the total cross section. The results are shown in Table 8.9 together with the corresponding values calculated from the γ-spectra in coincidence with the whole EUCLIDES array (as described in 8.7). The comparison of the two methods shows that they produce very similar results. It is also possible to extract the differential cross section in the centre of mass.

As already discussed in Sect. 8.9 it is possible to calculate the excitation energy of the ER from the energy of the detected particle, but it should be noted that due to the large angle covered by the detectors of EUCLIDES, the extracted value of the excitation energy covers a large distribution so a mean value for the excitation energy has been used to obtain the angular distribution in the centre of mass.

In a future experiment, the use of detectors with a better angular resolution will be very useful. This will allow us to determine the energy of the evaporated particles and the excitation energy with better precision. The calculation of the angular distribution in the centre of mass system has been performed utilizing mean values for E_x and θ_{lab} and the results are shown in Fig. 8.26. In the centre of mass, the angular

Table 8.8. Value of the differential cross section measured with the statistical errors for the two measured energies for the 1p and 1α evaporation channels.

Energy	evaporation channel	angle	$d\sigma_f/d\Omega$
47 MeV	1p	30°	0.36 mb/sr ± 0.03 mb/sr
47 MeV	1p	60°	0.30 mb/sr ± 0.02 mb/sr
47 MeV	1p	90°	0.24 mb/sr ± 0.01 mb/sr
47 MeV	1p	120°	0.143 mb/sr ± 0.003 mb/sr
47 MeV	1α	30°	0.491 mb/sr ± 0.008 mb/sr
47 MeV	1α	60°	0.337 mb/sr ± 0.006 mb/sr
47 MeV	1α	90°	0.220 mb/sr ± 0.008 mb/sr
47 MeV	1α	120°	0.10 mb/sr ± 0.02 mb/sr
40 MeV	1p	30°	0.016 mb/sr ± 0.002 mb/sr
40 MeV	1p	60°	0.012 mb/sr ± 0.001 mb/sr
40 MeV	1p	90°	0.0088 mb/sr ± 0.0008 mb/sr
40 MeV	1p	120°	0.0045 mb/sr ± 0.0003 mb/sr
40 MeV	1α	30°	0.026 mb/sr ± 0.003 mb/sr
40 MeV	1α	60°	0.0143 mb/sr ± 0.0004 mb/sr
40 MeV	1α	90°	0.010 mb/sr ± 0.001 mb/sr

Table 8.9. Cross sections measured with AGATA+EUCLIDES obtained by integrating the angular distribution of the evaporated particles compared with the value obtained from the integration of the γ-peaks from the spectra in coincidence with the whole EUCLIDES. Only the statistical errors are reported.

Energy	ER	σ_f angular distrib.	σ_f coincidence spectra
47 MeV	^{40}K	7.40 mb ± 0.05 mb	7.52 mb ± 0.04 mb
47 MeV	^{41}K	2.86 mb ± 0.08 mb	2.59 mb ± 0.04 mb
47 MeV	^{38}Ar	2.77 mb ± 0.03 mb	2.86 mb ± 0.02 mb
40 MeV	^{40}K	0.063 mb ± 0.003 mb	0.054 mb ± 0.002 mb
40 MeV	^{41}K	0.105 mb ± 0.003 mb	0.112 mb ± 0.004 mb
40 MeV	^{38}Ar	0.126 mb ± 0.004 mb	0.111 mb ± 0.005 mb

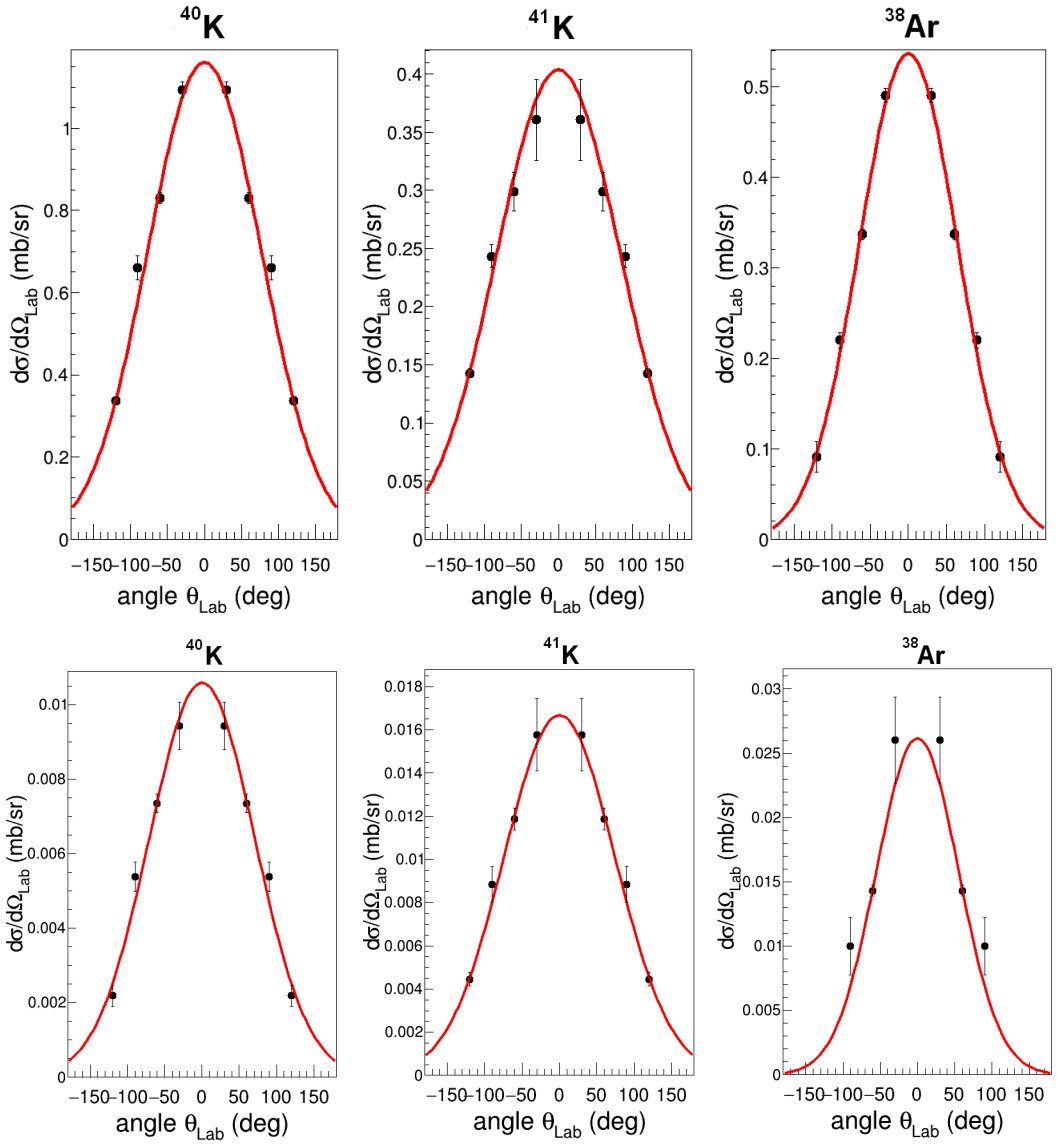

Figure 8.25. Angular distribution of the evaporated particles for the three most intense evaporation channels (1p1n, 1p and 1α) for the energy of 47 MeV (top panels) and 40 MeV (bottom panels) fitted with a Gaussian curve.

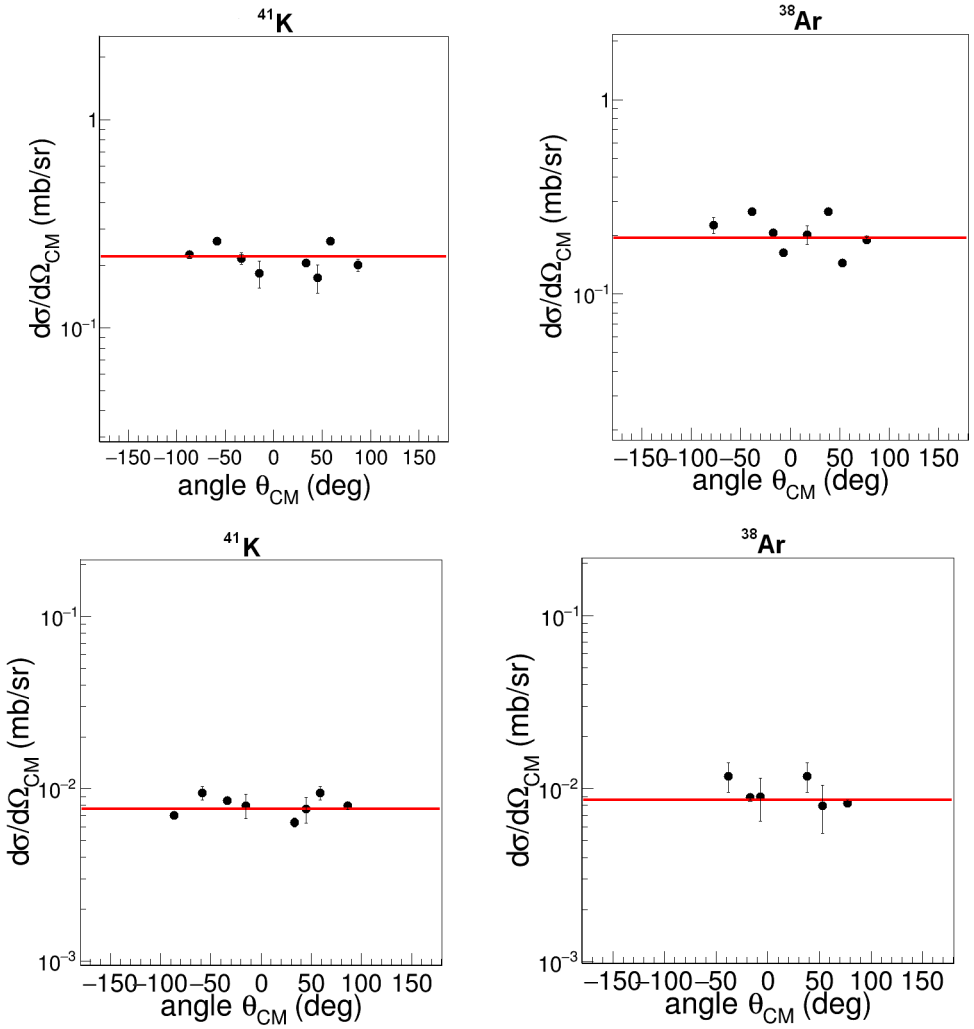

Figure 8.26. Angular distribution in the centre of mass of the evaporated particles for the 1p and 1α evaporation channels for the energy of 47 MeV (top panels) and 40 MeV (bottom panels) fitted with a constant value.

distribution of the evaporated particles was aspected to be isotropic, and as a consequence, a rough estimate of the fusion cross section can be obtained by multiplying the mean value of the differential cross section by 4π. The values of the cross section obtained with the angular distribution method and normalized to the cross section measured with PISOLO are compatible with the values obtained with the integration of the photopeaks in the coincidence γ-spectra with the whole EUCLIDES set-up (Sect. 8.7). Integrating the angular distribution of light particles can be very useful at energies far below the barrier where the main contribution to the fusion cross section (for light system) comes from the p and α evaporation channels, especially if combined with a detector with a good angular resolution.

8.11 Final Consideration

The results of the performed test are positive, and it has been possible to observe the γ-rays emitted from the ER detected by AGATA, in coincidence with the charged particles evaporated from the compound nucleus detected by EUCLIDES. The number of events corresponding to the transitions that populate the ground state has been used to estimate the fusion yield and extract the total fusion cross section. As an alternative method, the cross section has been obtained by integrating the angular distribution of the evaporated particles. In this way, three runs at 47 MeV and two at 40 MeV have been analyzed.

Chapter 9

Improvements of the γ-particle coincidence technique

The results from the AGATA and EUCLIDES test show that the γ-particle coincidence is a powerful method to measure the fusion cross section at low energies, and at this point, the next step is to perform a real measurement based on this technique. An experiment to measure the fusion cross section of the system ^{28}Si + ^{12}C in inverse kinematics using the γ-particles coincidences has been approved by the LNL PAC and performed very recently. The purpose was to better understand the behaviour of this system at very low energies and measure the cross section below the limit of the PISOLO set-up. In the experiment, we have employed two DSSD annular silicon detectors [52] (Fig. 9.1) of 5 inches in diameter called SAURON instead of EUCLIDES, placed 5 cm from the target one upstream and one downstream. The thickness of the two detectors is 1500 μm for the one at forward angles and 500 μm for the one at backward angles. With this kind of detector it is not possible to distinguish between protons and α-particle with the E-ΔE method, but, thanks to the high angular resolution the separation can be performed kinematically or through a pulse shape analysis. Indeed these detectors have 16 rings on the front side (giving the θ angle), and 16 sectors on the rear Ohmic side (giving the φ information) granting a very good angular resolution allowing a precise reconstruction of the kinematic. Similar DSSD detectors have already been used in sub-barrier fusion measurements, at Argonne National Laboratory [4] [53] in combination with the Gammasphere array and in the set-up STELLA [54] together with the UK FATIMA $LaBr_3$(Ce) array [55] to investigate the system ^{12}C + ^{12}C with success. In the expansion of the AGATA reaction chamber, two monitor detectors have been also installed at an angle of 12° with respect to the beam direction, in order to detect the elastic scattering of the beam and use it to normalize the fusion yield to the Rutherford cross section.
The experiment has consisted in measuring the cross section of the ^{28}Si + ^{12}C system starting from E_{CM} = 15 MeV to properly set up the coincidences between AGATA

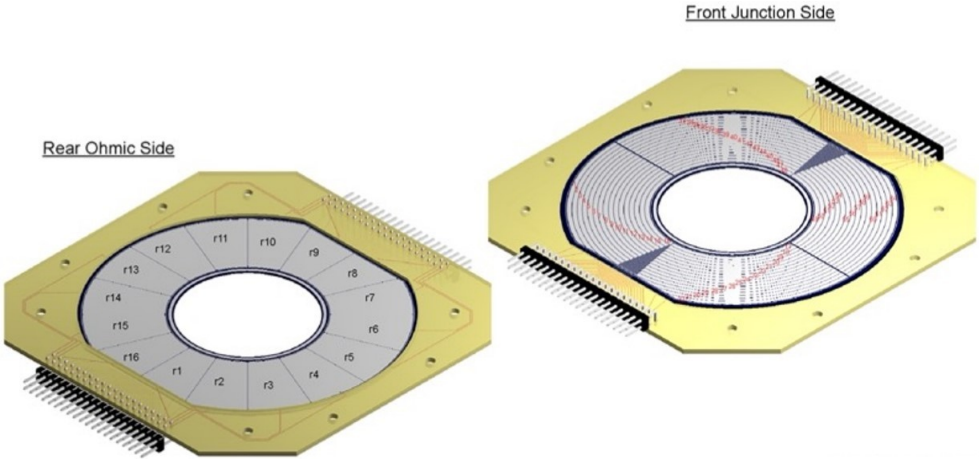

Figure 9.1. Picture of the front side and back side of the DSSD detector for the proposed experiment.

and SAURON. Then measuring at two energies that were also measured with PISOLO (12.3 MeV and 10.2 MeV) to have an overlap between the two approaches and finally measure at two new energies, 9.15 MeV and 8.85 MeV that should correspond to cross sections of about ~ 0.75 μb and $\sim$200 nb, respectively. Fig. 9.2 is a picture of the two DSSD detectors mounted on the support used in the experiment (top panel) and installed inside the reaction chamber (bottom panel), where one also sees the tantalum shield used to protect the detector from the beam and a 15 μm thick nickel foil to stop the elastic scattering of the beam on the target. The, very preliminary, online results obtained during the experiment show that it is possible to identify the γ-transitions in coincidence with the evaporated charged particles. The γ-spectrum in coincidence with the forward detector of SAURON for the energy of 50 MeV is shown in Fig. 9.3 where the transitions from the 2p, 1p1n, 1p, 1α and 1α1p evaporation channels have been recognized. It has also been possible to combine the energy of the particles detected by only one ring of SAURON and the energy of the γ-rays. Thanks to the very good angular resolution of the DSSD it is possible to recognize the different evaporation channels, as shown in Fig. 9.4 for the ring at 24.6° of the forward DSSD. The online analysis of the spectra obtained during the experiment gives promising results for the extraction of the total fusion cross section of the system ^{28}Si + ^{12}C and for employing this technique to measure fusion cross sections at very low energies also for other systems of interest like ^{24}Mg + ^{12}C to better understand the behaviour of its excitation function in the range of hundreds of nanobarns (as described in Sect. 6.2) or also for lighter systems of interest for astrophysics like ^{16}O + ^{12}C.

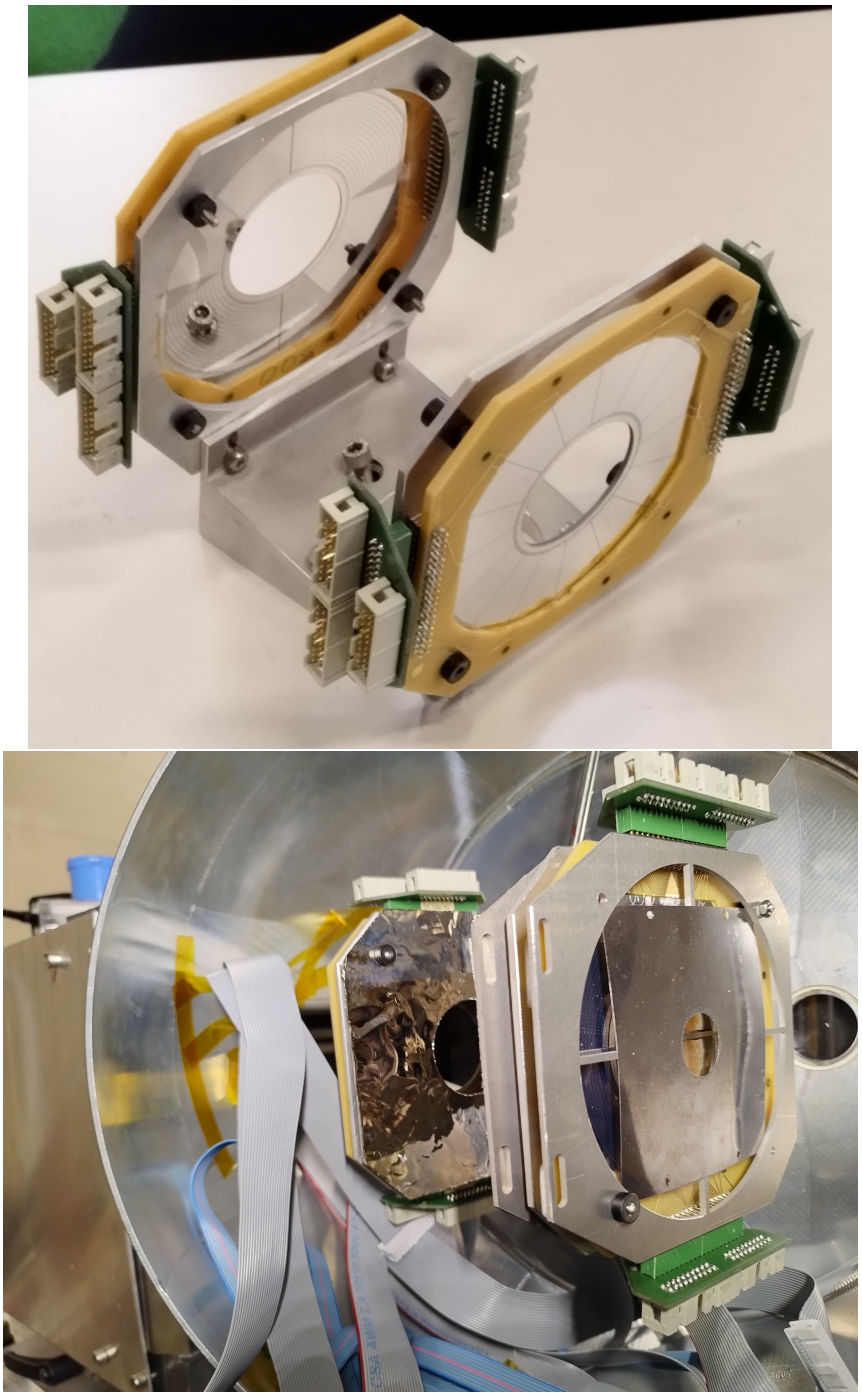

Figure 9.2. Picture of the two DSSD detectors placed on the supports in the configuration used for the experiment (top panel) and the set-up installed in the AGATA reaction chamber (bottom panel).

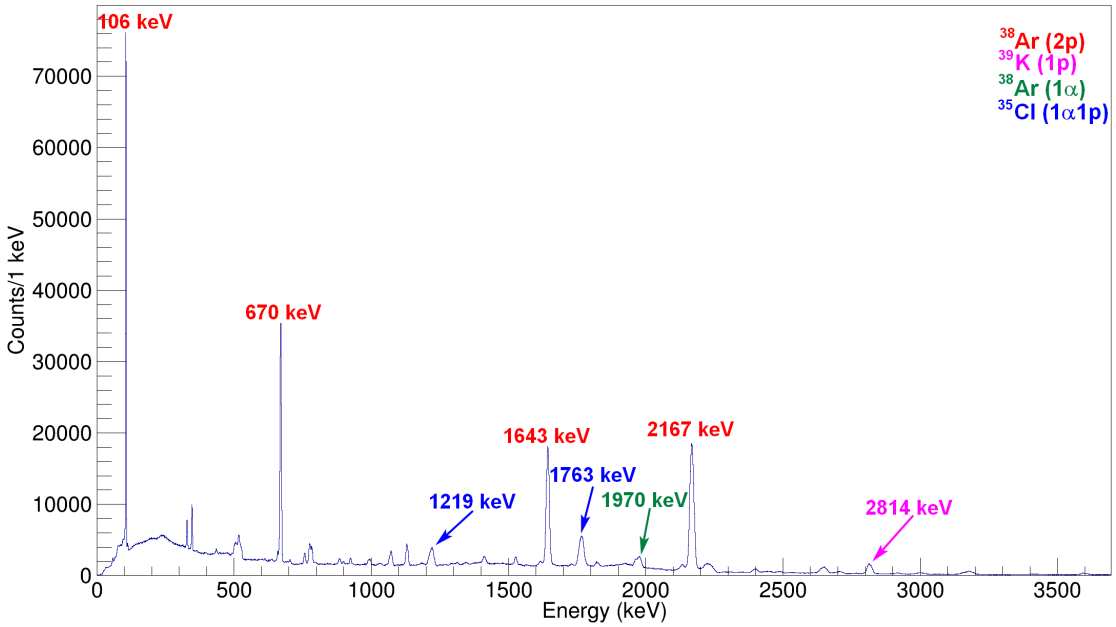

Figure 9.3. γ-ray energy spectrum of AGATA obtained imposing the coincidences with the forward detector of SAURON.

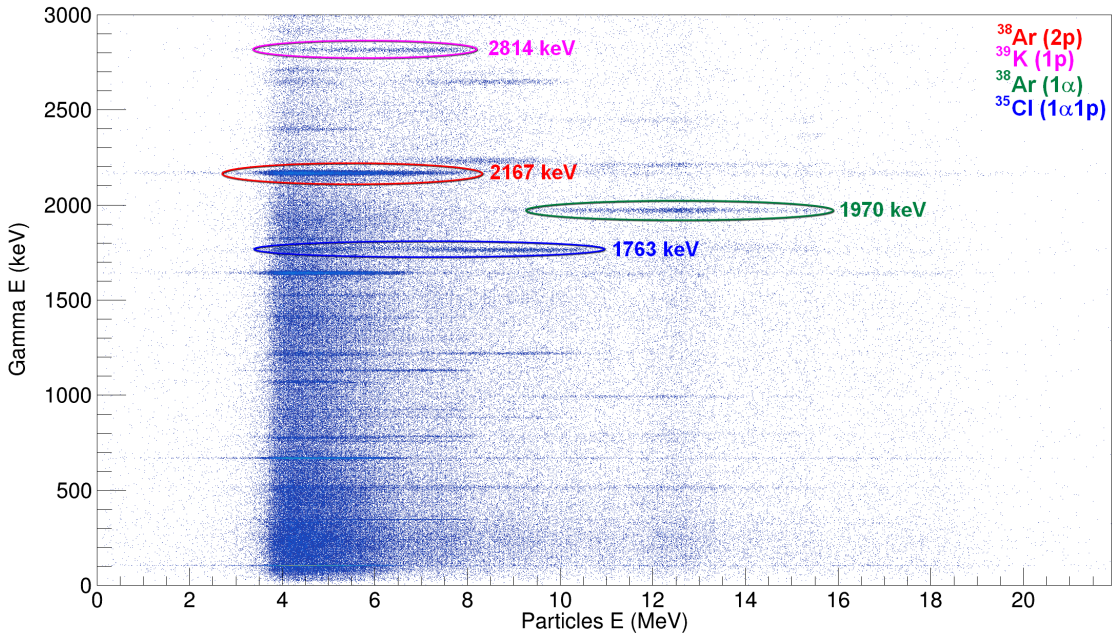

Figure 9.4. Spectrum of particles energy vs γ energy at 50 MeV for the ring at 24.6° of the forward SAURON.

Chapter 10

Conclusion and perspective

The purpose of this thesis work was to better understand the unusual behaviour of the excitation function of the system ^{24}Mg + ^{12}C at energies far below the Coulomb barrier compared with other similar systems. For this reason the fusion cross section of the case ^{26}Mg + ^{12}C has been measured down to a few μb with the set-up PISOLO. The results show that the behaviour of these two similar systems appears to be very different, indeed at sub-barrier energies the hindrance shows up at lower energies for ^{26}Mg + ^{12}C with a narrower maximum for the astrophysical S factor. The reason could be the α-like structure of the ^{24}Mg. Since it is not possible to measure fusion cross section below a few μb with PISOLO, two different techniques have been tested in this work. The first one is an upgrade of PISOLO and consists of the installation of two silicon detectors in the reaction chamber to detect the charged particles evaporated after the fusion process putting them in coincidence with the ER detected by PISOLO. The second technique is based on the coincidences between the charged particles evaporated by the compound nucleus and the γ-rays emitted by the ER using the silicon array EUCLIDES and the γ spectrometer AGATA. The results for the two tests are positive confirming the possibility of measuring fusion cross sections using these two techniques in the range of hundreds of nanobarns. In the future, these two methods will be employed for fusion cross section measurement. An experiment based on the γ-charged particles coincidence has already been performed, using the SAURON + AGATA set-up. The system ^{28}Si + ^{12}C has been measured, providing promising results during the online analysis. Other experiments are going to be proposed, like the cited ^{24}Mg + ^{13}C and the system ^{16}O + ^{12}C which is important for astrophysics.

Chapter 11

Appendix: Tables of experimental data

Table 11.3. List of the γ-transitions that go directly to the ground state and the measured counts of the corresponding photo-peak, for each observed evaporation residue at the two measured energies during the AGATA+EUCLIDES test (Sect. 8.3).

nucleus	γ Energy (keV)	counts (47 MeV)	counts (40 MeV)
^{40}K	770.3	84055 ± 590	3171 ± 165
	891.4	109999 ± 592	2362 ± 151
	1929.3	2360 ± 49	0
	2017.5	1071 ± 33	0
	2039.9	6752 ± 293	0
	2070.1	5611 ± 281	0
	2230.5	3480 ± 271	0
	2260.1	1063 ± 32	0
	2289.2	7175 ± 254	0
	2367.2	3587 ± 233	0
	2397.1	2539 ± 228	0
	2545.9	3070 ± 242	0
	2716.9	2254 ± 187	0
	2756.8	2785 ± 202	0
	2787.1	2411 ± 199	0
	2950.8	1694 ± 141	0
	3100	1354 ± 36	0
	3128.1	235 ± 15	0
	3153.5	955 ± 30	0
	3229.4	20 ± 4	0

	3338.2	30 ± 5	0
^{41}K	980.5	8460 ± 419	1584 ± 144
	1293.6	11682 ± 417	500 ± 130
	1559.9	4554 ± 320	814 ± 95
	1582.0	2234 ± 346	1001 ± 98
	1677.2	28940 ± 383	3161 ± 113
	1697.9	7041 ± 344	963 ± 101
	2143.7	2463 ± 312	522 ± 88
	2166.7	6466 ± 250	1230 ± 44
	2507.9	1291 ± 233	200 ± 63
	2447.8	674 ± 50	0
	3179.7	20 ± 9	0
^{38}Ar	2167.4	28856 ± 224	3085 ± 192
	3936.1	1474 ± 88	302 ± 52
^{40}Ar	1460.8	23056 ± 151	1848 ± 143
^{37}Ar	1409.8	4607 ± 168	200 ± 114
	1611.2	7684 ± 188	0
	2217.1	2310 ± 148	0
	2215.2	1306 ± 136	0
	2490.2	1679 ± 141	0
^{37}Cl	1726.4	688 ± 226	0
^{41}Ca	1942.7	33162 ± 899	7041 ± 472
	2009.8	31380 ± 817	3360 ± 468
	2576.3	5662 ± 713	0
	2605.7	13433 ± 623	0
	2883.8	6728 ± 605	1088 ± 233
	2959.2	17251 ± 616	1388 ± 230
	3201.1	23679 ± 602	3534 ± 225
	3676.8	8702 ± 546	538 ± 199
^{40}Ca	3736.5	105930 ± 545	4166 ± 189
	3903.9	56514 ± 456	2448 ± 186
	5248.9	2593 ± 286	0
	5628.5	1491 ± 225	0
^{34}S	2127.5	8125 ± 190	0
^{39}Cl	396.4	944 ± 130	0

Table 11.1. Logarithmic derivative obtained in the ^{26}Mg + ^{12}C experiment (Sect. 5.3).

E_{CM} (Mev)	L(E) (MeV^{-1})
15.13	0.38 ± 0.09
14.42	0.56 ± 0.04
14.10	0.54 ± 0.06
13.80	0.62 ± 0.07
13.15	0.63 ± 0.09
12.84	0.52 ± 0.08
12.52	0.60 ± 0.09
12.20	0.81 ± 0.10
11.88	1.20 ± 0.09
11.57	1.25 ± 0.10
11.25	1.5 ± 0.1
10.93	1.6 ± 0.1
10.70	2.1 ± 0.1
10.46	2.3 ± 0.2
10.22	2.9 ± 0.2
10.06	2.6 ± 0.3
9.91	2.7 ± 0.3
9.75	2.3 ± 0.3
9.59	2.8 ± 0.3
9.43	3.0 ± 0.4
9.27	4.2 ± 0.4
9.11	4.0 ± 0.5
8.96	3.6 ± 0.6
8.80	2.8 ± 0.8
8.64	3.8 ± 2.2
8.48	3.3 ± 1.0
8.32	4.2 ± 1.5

Table 11.2. Astrophysical S-factor obtained in the ^{26}Mg+^{12}C experiment (Sect. 5.3)

E_{CM}	S(E) (MeV·mb)
15.69	1.498 ± 0.066
15.21	3.06 ± 0.14
14.89	4.12 ± 0.27
14.58	6.68 ± 0.59
13.63	24.2 ± 1.2
13.31	36.8 ± 2.3
12.99	58.5 ± 3.7
12.68	100.9 ± 6.5
12.36	184.1 ± 9.1
12.04	295 ± 19
11.73	451 ± 28
11.41	625 ± 46
11.09	1055 ± 74
10.78	1367 ± 106
10.46	2063 ± 153
10.30	2057 ± 174
10.14	2100 ± 163
9.99	2294 ± 154
9.83	2739 ± 290
9.67	2788 ± 349
9.51	3691 ± 431
9.35	3718 ± 462
9.19	3560 ± 440
9.03	2771 ± 448
8.88	3297 ± 671
8.72	3865 ± 1061
8.56	4586 ± 1569
8.25	5646 ± 2128
8.09	4702 ± 2941

Bibliography

[1] N. Rowley, G.R. Satchler, and P.H. Stelson. In: *Phys. Lett. B* 254 (1991).

[2] C.L. Jiang et al. In: *Phys. Rev. Lett.* 89 (2002).

[3] W.P. Tan et al. In: *Phys. Rev. Lett.* 124 (2020), p. 192702.

[4] C.L. Jiang et al. In: *Phys. Rev. C* 97 (2018), 012801(R).

[5] G. Fruet et al. In: *Phys. Rev. Lett.* 124 (2020), p. 192701.

[6] C.L. Jiang et al. In: *Eur. Phys. J. A* 57 (2021), p. 235.

[7] C.L. Jiang et al. In: *Phys. Rev. C* 75 (2007), p. 015803.

[8] A.M. Stefanini et al. In: *Phys. Rev. C* 82 (2010), p. 014614.

[9] G. Montagnoli et al. In: *J. Phys. G* 49 (2022), p. 095101.

[10] T. Ichikawa, K. Hagino, and A. Iwamoto. In: *Physical Review C* 92 (2015), p. 6.

[11] S. Akkoyun et al. In: *Nucl. Instrum. Methods Phys. Res. A* 668 (2012), p. 26.

[12] D. Testov et al. In: *Eur. Phys. J. A* 55 (2019), p. 47.

[13] Ö. Akyüz and A. Winther. In: *Proc. Int. School of Physics "Enrico Fermi" Course LXXVII, Varenna* (1979).

[14] S. Misicu and H. Esbensen. In: *Physical Review C* 75 (2007), pp. 1–14.

[15] G. Bertsch et al. In: *Nuclear Physics A* 284 (1977), pp. 399–419.

[16] E. Uegaki and Y. Abe. In: *Progress of Theoretical Physics* 90.3 (1993), p. 615.

[17] D. L. Hill and J. A. Wheeler. In: *Physical Review* 89 (1995), pp. 1102–1145.

[18] C. Y. Wong. In: *Physical Review Letters* 31.12 (1973), pp. 766–769.

[19] C.L.Jiang et al. In: *Phys. Rev. Lett.* 93 (2004), p. 012701.

[20] C. H. Dasso, S. Landowne, and A. Winther. In: *Nuclear Physics A* 405 (1983), pp. 381–396.

[21] C. H. Dasso, S. Landowne, and A. Winther. In: *Nuclear Physics A* 432 (1985), pp. 495–513.

[22] K. Hagino and N. Takigawa. In: *128.6* (2012).

[23] M. A. Nagarajan, A. B. Balantekin, and N. Takigawa. In: *Physical Review C* 38 (1986), pp. 894–898.

[24] K. Hagino, N. Rowley, and A. T. Kruppa. In: *Computer Physics Communications* 123 (1999).

[25] T. Ichikawa, K. Hagino, and A. Iwamoto. In: *Physical Review Letters* 103 (2009), pp. 1–4.

[26] S.Misicu and H. Esbensen. In: *Phys. Rev. Lett.* 96,112701 (2006).

[27] A.M. Stefanini, G. Montagnoli, and M. Del Fabbro et al. In: *Physical Review C* 100 (2019), p. 044619.

[28] A.M. Stefanini and G. Montagnoli et al. In: *Physics Letters B* 728 (2014), pp. 639–644.

[29] G. Montagnoli et al. In: *Nuclear Instruments and Methods in Physics Research* 547.2-3 (2005), pp. 455–463.

[30] H. W. Fulbright. In: *Nuclear Instruments and Methods* 162 (1979), pp. 21–28.

[31] O.B.Tarasov and D.Bazin. URL: `http://lise.nscl.msu.edu`.

[32] P.-A. Söderström et al. In: *Nuclear Instruments and Methods in Physics Research Section A* 638 (2011), p. 1.

[33] B. Bruyneel, B. Birkenbach, and P. Reiter. In: *The European Physical Journal A* 52 (2012), p. 3.

[34] K. Daneshvar et al. In: *Phys. Rev. C* 25 (1982), p. 1342.

[35] S. Raman. In: *Atomic Data and Nuclear Data Tables* 78 (2001), pp. 1–128.

[36] T. Kibédi and R. H. Spear. In: *Atomic Data and Nuclear Data Tables* 80 (2002), pp. 35–82.

[37] W. P. Tan et al. In: *Phys. Rev. C* 96 (2017), p. 045804.

[38] K. A. Erb et al. In: *Phys. Rev. C* 22 (1980), p. 507.

[39] D. A. Bromley, J. A. Kühner, and E. Almqvist. In: *Phys. Rev. C* 4 (1960), p. 365.

[40] C. L. Jiang et al. In: *Phys. Rev. Lett.* 110 (2013), p. 072701.

[41] N.T. Zhang et al. In: *Phys. Lett. B* 801 (2019), p. 135170.

[42] A. Gavron. In: *Phys. Rev. C* 21 (1980), p. 230.

[43] G. Montagnoli et al. In: *Phys. Rev. C* 97 (2018), p. 024610.

[44] M. Beckerman et al. In: *Nucl. Phys. A* 278 (1977), p. 333.

[45] A.S. Iljinov et al. In: *Nucl. Phys. A* 543 (1992), p. 517.

[46] URL: `https://baltig.infn.it/gamma/agataselector`.

[47] F. Angelini. MA thesis. Università di Padova, 2022.

[48] R. M. Pérez Vidal. PhD thesis. Universidad de Valencia, 2019.

[49] D. C. Radford. In: *Nucl. Instr. Meth. A* 361 (1995), pp. 297–305.

[50] URL: `https://radware.phy.ornl.gov/gf3/gf3.html`.

[51] *AGATA Geant4 simulation code*. URL: `http://npg.dl.ac.uk/svn/agata`.

[52] URL: `http://www.micronsemiconductor.co.uk`.

[53] C.L. Jiang et al. In: *Nucl. Instr. Meth. Phys. Res. A* 682 (2012), p. 12.

[54] M. Heine et al. In: *Nucl. Instr. Meth. Phys. Res. A* 903 (2018), p. 1.

[55] R. Shearman et al. In: *Rad. Phys. Chem.* 140 (2017), p. 475.

Ringraziamenti

A conclusione di questo elaborato desidero ringraziare tutte le persone che mi hanno aiutato a completare questo lavoro. In particular modo ringrazio Giovanna Montagnoli e Alberto Stefanini, per avermi introdotto in questo ambiente di ricerca, per la disponibilità che hanno sempre mostrato e per gli insegnamenti e il sostegno che mi hanno fornito. Un ringraziamento anche a Daniele Brugnara per il suo aiuto con l'analisi dati e per la disponibilità a rispondere a tutte le mie domande. Desidero ringraziare anche Alain Goasduff sempre pronto a risolvere qualunque problems durante gli esperimenti. Infine vorrei ringraziare tutti i colleghi dei Laboratori Nazionali di Legnaro, che mi hanno accompagnato durante il periodo di dottorato.